

National and Kapodistrian University of Athens
Department of Physics
Section of Nuclear and Particle Physics



Master's Thesis
Comparison of the decays $B \rightarrow J/\psi K$, $J/\psi \rightarrow \mu\mu$ and
 $B \rightarrow \mu\mu K$ with the CMS experiment at CERN LHC

Melachroinos Georgios
R.N. 2019201

Supervisor: Prof. Sphicas Paraskevas
Assistant Supervisor: Prof. Tetradis Nikolaos
Assistant Supervisor: Ass. Prof. Vellidis Konstantinos

March 2021

Abstract

We present a measurement of the ratio of branching fractions of charged B mesons to $B^\pm \rightarrow \mu^+\mu^-K^\pm$ and $B^\pm \rightarrow J/\psi K^\pm$, with the latter decay followed by $J/\psi \rightarrow \mu^+\mu^-$. The direct decay $B^\pm \rightarrow \mu^+\mu^-K^\pm$ involves a Flavor-Changing Neutral Current (FCNC), and thus, is forbidden at tree level in the Standard Model. Instead, the decay proceeds via higher-order processes, and is therefore rare, with a branching fraction of $\sim 10^{-7}$, which is four orders of magnitude smaller than the $B \rightarrow J/\psi K$ decay. FCNC rare decays of B mesons are particularly interesting, since they probe Lepton Flavor Universality in the Weak Interactions. In this Master's thesis, we reconstruct both decay modes, using proton-proton collisions recorded by the CMS experiment at the Large Hadron Collider in 2018. We then measure the fraction $R_K(\mu) = Br(B^\pm \rightarrow \mu^+\mu^-K^\pm)/Br(B^\pm \rightarrow J/\psi(\mu^+\mu^-)K^\pm)$, which is used in a full CMS analysis of a comparison of $R_K(\mu)$ with $R_K(e)$, with $R_K(e)$ being the same ratio for decays with electrons in the final state.

Περίληψη

Παρουσιάζουμε μια μέτρηση του λόγου των πιθανοτήτων των διασπάσεων των φορτισμένων μεσονίων B σε $B^\pm \rightarrow \mu^+\mu^-K^\pm$ και $B^\pm \rightarrow J/\psi K^\pm$, με τη δεύτερη διάσπαση να ακολουθείται από $J/\psi \rightarrow \mu^+\mu^-$. Η πρώτη διάσπαση απαγορεύεται στην κατώτερη τάξη από το Καθιερωμένο Πρότυπο καθώς αντιστοιχεί σε Ουδέτερο Ρεύμα Αλλαγής Γεύσης (Flavor-Changing Neutral Current (FCNC)). Αντ' αυτού, η διάσπαση λαμβάνει χώρα μέσα από διαδικασίες ανώτερης τάξης, και ως εκ τούτου είναι σπάνια, με πιθανότητα της τάξης του $\sim 10^{-7}$, σχεδόν τέσσερις τάξεις μεγέθους μικρότερη από την διάσπαση $B \rightarrow J/\psi K$. Τα σπάνια Ουδέτερα Ρεύματα Αλλαγής Γεύσης των B μεσονίων έχουν ιδιαίτερο ενδιαφέρον, καθώς ελέγχουν την Παγκοσμιότητα της Γεύσης των Λεπτονίων των Ασθενών Αλληλεπιδράσεων (Lepton Flavor Universality of the Weak Interactions). Στην παρούσα διπλωματική εργασία ανακατασκευάζονται οι δύο διασπάσεις χρησιμοποιώντας δεδομένα που καταγράφηκαν το 2018 από το πείραμα CMS στον Μεγάλο Επιταχυντή Αδρονίων (LHC). Ακολούθως, υπολογίζεται ο λόγος $R_K(\mu) = Br(B^\pm \rightarrow \mu^+\mu^-K^\pm)/Br(B^\pm \rightarrow J/\psi(\mu^+\mu^-)K^\pm)$, που χρησιμοποιείται σε ανάλυση του CMS για σύγκριση με τον λόγο $R_K(e)$, που είναι η αντίστοιχη ποσότητα σε διασπάσεις με ηλεκτρόνια στην τελική κατάσταση.

Contents

1	The CMS detector	6
1.1	The Large Hadron Collider	6
1.2	The Compact Muon Solenoid - CMS	8
1.2.1	Tracking System	9
1.2.2	The Electromagnetic Calorimeters	12
1.2.3	The Hadronic Calorimeters	15
1.2.4	The Superconducting Solenoid	17
1.2.5	The Muon Chambers	19
1.2.6	The Forward Detectors	24
1.2.7	Trigger and DAQ systems	25
2	The Particle Flow and Event Reconstruction	28
2.1	Tracks, Primary vertices and Beamspots	29
2.1.1	Track Reconstruction	29
2.1.2	Primary Vertices and Beamspot	32
2.2	Muons	34
2.2.1	Muon Tracks Reconstruction	34
2.2.2	Muon Identification	35
2.2.3	High Level Triggering Muons	37
2.3	Calorimeter Clustering, Electrons and Photons	39
3	Electroweak theory and Flavour Changing Neutral Currents	42
3.1	Electrodynamics as a Gauge Theory	42
3.2	Weak Interactions as Gauge Theory	44
3.2.1	Weak Isospin Doublets and Singlets	44
3.2.2	Weak Interactions as Yang-Mills Theory	45
3.2.3	The Cabibbo-Kobayashi-Maskawa Matrix, the W propagator and the Flavour Changing Neutral Currents	48
3.2.4	The Z propagator and weak Neutral Currents	51
3.3	Electroweak Unification	52
3.3.1	The Higgs Mechanism and the Spontaneous Symmetry Breaking	54
3.4	Lepton Flavour Universality	57
3.5	$R_K(\mu)$	58
3.6	$B^\pm \rightarrow K^\pm \ell^- \ell^+$	59
3.7	$B \rightarrow J/\psi K, J/\psi \rightarrow \mu^+ \mu^-$	62
3.7.1	$B \rightarrow J/\psi K$	62
3.7.2	$J/\psi \rightarrow \mu^+ \mu^-$	64

4	Analysis	65
4.1	Trigger Strategy	65
4.2	HLT-Reco Muon Matching	66
4.3	Dimuon Mass Region	70
4.4	B meson reconstruction and preselection cuts	71
4.5	acceptance \times efficiency for Tag Side	73
4.6	BDT training and cut	81
4.7	Fitting Processes	85
4.8	Scale Factor	89
4.9	$R_K(\mu)$ measurement	90
4.10	$R_{\psi(2S)}(\mu)$ measurement	91
5	Summary and Outlook	97

1 The CMS detector

1.1 The Large Hadron Collider

The Large Hadron Collider (LHC), located at the Swiss-French borders, is the biggest and strongest particle accelerator. LHC boosts charged particles, such as protons, at high speeds, close to the speed of light to collide them either against each other or to fixed target. LHC is composed of superconducting magnets that boost the energy of the particles along the way of a 27 Km long ring. Collisions take place in four points where the four big experiments are located.

Inside the collider, two beams of particles are moving in opposite directions in separate beam pipes, with velocity almost equal to that of light. The beams are kept in track inside the beam pipe using magnetic fields along the accelerator. To ensure the highest efficiency with the less energy loss, the magnets that form the collider need to be superconducting. The whole system of magnets in order to operate effectively is chilled to $-271.3\text{ }^{\circ}\text{C}$ by using liquid helium. The beam pipes are also kept in ultra high vacuum. 1232 dipole magnets of 15 m length and 392 quadrupole magnets of 5-7 m length that bend and focus the beams respectively, form the LHC.

Each beam is not a constant flux of particles, but is separated in bunches of particles. Apart from protons (p), ions of Lead (Pb) are also injected in the LHC so as apart from p-p collisions, p-Pb and Pb-Pb collisions can take place. For the rest of this thesis, we will talk only about p-p collisions. Each proton beam includes 2808 bunches, each bunch contains at start 1.2×10^{11} protons and completes 11245 turns per second. Each bunch is 25 ns away from the previous one and passes completely a vertical slice of the ring in 1.25 ns.

However, protons are not injected in the LHC with their maximum energy, but are accelerated in levels passing through the CERN accelerator complex [7]. First of all, hydrogen atoms are ionized using an electric field and so protons are separated by their electrons. All the protons are then gathered and pass through a linear accelerator (LINAC). The LINAC [9] is formed by radiofrequency cavities, where electric fields along them switches from positive to negative at a given frequency forcing the protons to be pulled forwards and pushed from behind. The frequency of the change is such to ensure the particles accelerate not in a continuous stream, but in closely spaced bunches.

Protons are then injected to the four superimposed synchrotron rings that form the Proton Synchrotron Booster (PSB) [14], where they are accelerated from 50 MeV up to 1.4 GeV. Subsequently, protons are accelerated up to 25 GeV passing through the magnets of the Proton Synchrotron (PS) [13], up to 450 GeV passing through the Super Proton Synchrotron (SPS) [14] and finally up to 6.5 TeV by injecting in the LHC.

SPS apart from separating the protons and creating the two beams, provides beams for the COMPASS experiment and the NA61/SHINE and NA62 experiments. Back in 1973, SPS by running as a proton-antiproton collider, was providing beams for the Gargamelle experiment leading to the discovery of W and Z particles and to the award of Nobel Prize in 1979 to Glashow, Salam and Weinberg for their contributions to the theory of the unified

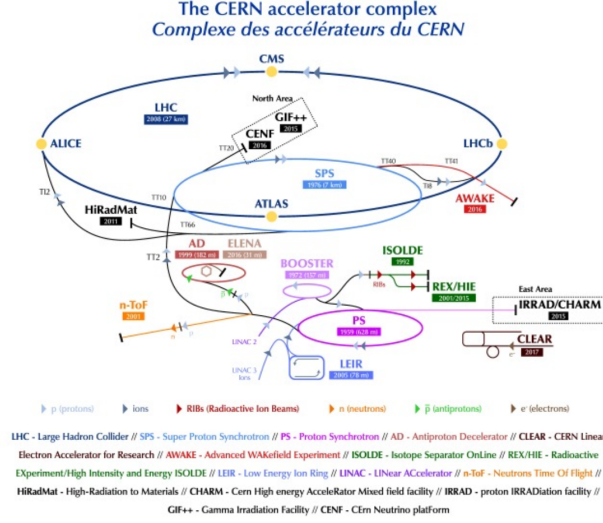


Figure 1: The CERN accelerator complex [30].

weak and electromagnetic interaction between elementary particles, including, inter alia, the prediction of the weak neutral current.

However, the energy boosting can not be continued for as long as we wish since more powerful magnetic fields would be required to keep particles in orbit. Due to the head-on collisions between the protons the total energy per collision is 13 TeV in the lab frame. However, the partons (gluons and quarks) that form the protons and are the particles that truly interact, carry only a part of the protons' momentum. They are moving along the beam axis (which we call the z-axis) and in the lab frame, same with the center of mass frame for the bunches, their system is randomly Lorentz boosted since each parton has a part of the available momentum.

So, unfortunately, the total available energy in the partons' center of mass frame is always lower than 13 TeV. The available energy in the partons' center of mass frame determines the possible produced particles, since particles with more mass than the available energy is strictly forbidden to be produced. Therefore, we can now understand why we need billions of protons in each bunch. Each process has a specific probability σ to happen, so if we have more protons we will finally collect more events for the process we are looking for. This is expressed using the following formula:

$$\frac{dN}{dt} = \mathcal{L}\sigma,$$

where $\frac{dN}{dt}$ is the number of collisions, which are called events, and \mathcal{L} is the the number of potential collisions per surface unit over a given period of time, also known as instant luminosity. \mathcal{L} is calculated from:

$$\mathcal{L} = f \frac{n_1 n_2}{4\pi\sigma_x \sigma_y},$$

where f is the collision frequency, n_1 and n_2 are the number of protons per bunch and $\sigma_x \sigma_y$

is the surface of the bunches in the transverse plane. We can see now that the more squeezed the beams are the higher the luminosity is and the more events will be detected. Instant luminosity is measured in $\text{fb}^{-1}\cdot\text{s}^{-1} = 10^{-24}\text{cm}^2\cdot\text{s}^{-1}$. Instead of using instant luminosity \mathcal{L} , it is a common aspect to use the integrated luminosity L , that is given by intergrating the instant luminosity over a period of time $L = \int_{t_1}^{t_2} \mathcal{L}dt$. During Run3 luminosity will be double with respect to the 2018 luminosity and during High-Luminosity LHC (HL-LHC) luminosity will be 5 times bigger than the one in Run3 and 10 times bigger than the original pre-designed luminosity [8]. Along the LHC, there are four collision points where the four big experiments, ATLAS, CMS, ALICE and LHCb are built.

1.2 The Compact Muon Solenoid - CMS

The Compact Muon Solenoid (CMS) Detector (2) is a multilayered cylindrical detector located at one of the collision points, the point 5 of the Large Hadron Collider (LHC). A penetrating particle coming from the interaction point of the two proton bunches passes through the following layers: a silicon-based particle tracker, a scintillating crystal electromagnetic calorimeter, a sampling hadronic calorimeter, a central superconducting solenoid magnet ($\approx 4\text{ T}$) and 4 alternating layers of muon detectors and return yokes of the magnet. The detector consists of a barrel part (made up from 5 wheels) that is sealed with two end-caps.

The CMS Experiment is designed as a general-purpose detector, capable of studying many aspects of proton collisions at 0.9-14 TeV, the center-of-mass energy of the LHC.

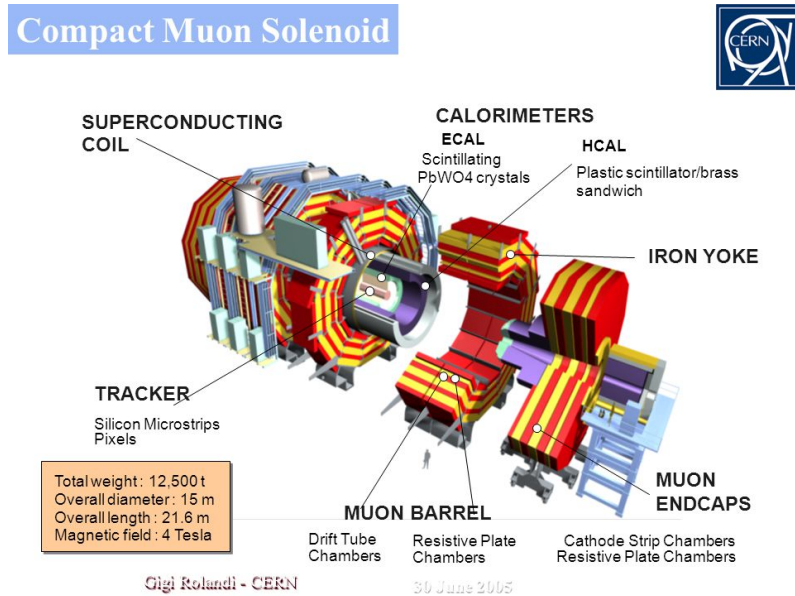


Figure 2: The Compact Muon Solenoid.

A very usefull quantity for relativistic particles is the pseudorapidity, measured as $\eta = -\ln(\tan(\theta/2))$, where θ is the polar angle from the z axis.

1.2.1 Tracking System

Momentum, one of the most crucial parameter, is calculated by tracking the particles' path through a 4T magnetic field (the more curved the path the less momentum the particle has). The tracker needs to record particle paths accurately. As less material as possible should be used so as to disturb the particle as less as possible. This is done by taking position measurements so accurate that tracks can be reliably reconstructed using just a few measurement points. Each measurement is accurate to $10\ \mu\text{m}$. The tracking system is also the inner most layer of the detector, and hence, receives the highest volume of particles: the construction materials were therefore carefully chosen to resist radiation.

The CMS Tracker consists entirely of silicon. Electron-hole pairs in doped semiconductor wafer (usually silicon or germanium) created by the ionisation process, are drifting along the direction of the external electric field where they are collected by p-n junctions, shaped into strips or pixels. With appropriate amplification the induced charges are transferred into readout signals. Silicon tracking detectors typically consist of several cylindrical surfaces of silicon wafers. A charged particle will leave a "hit" in a silicon sensor in each cylindrical layer from which the trajectory of the charged particle track can be reconstructed.

The pixel tracker is at the very core of the detector and deals with the highest intensity of particles. It is surrounded by the silicon microstrip detectors. As particles travel through the tracker the pixels and microstrips produce electric signals that are amplified and detected.

Tracker's main purpose is to record the path of charged particles and after that to measure momentum by measuring the radius from the bended trajectories due to the magnetic field. Finally, when the tracks are reconstructed, the tracking system reconstructs the primary and the secondary vertices. Primary vertices are the points where protons interact, and therefore are the points where plenty of tracks are coming from. Secondary vertices are points away from the beam axis where other particles decayed and so only a few tracks are forming them.

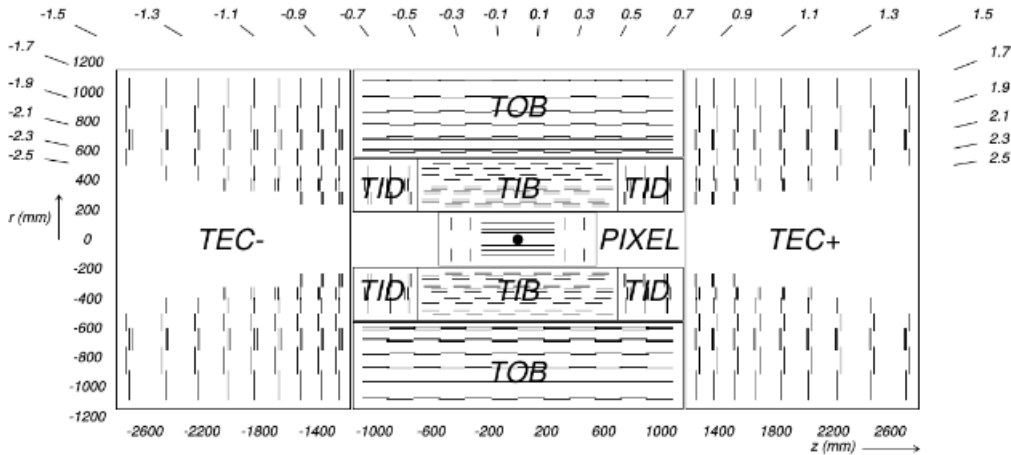


Figure 3: The CMS tracking system.

The tracker detector can reconstruct a track within $|\eta| < 2.4$ range that corresponds to an

angle of almost 80° from the xy -plane. The Tracker consists of five parts: A) Pixel Detector B) Tracker Inner Barrel (TIB 4 layers), C) Tracker Inner Disks (TID 3 disks), D) Tracker Outer Barrel (TOB 6 layers) and E) Tracker End Caps (TEC 9 disks). All parts apart from the Pixel Detector are made of silicon microstrips.

1.2.1.1 Pixel Detector

The Pixel Detector [11] contains 124 million pixels and allows the tracks reconstruction with extreme accuracy. It is the closest detector to the beam pipe and for this reason it has been replaced and upgraded twice since the first Runs back in 2010. During 2018 and after the Extended Year-End Technical Stop it was composed by four cylindrical layers placed at 3, 6.8, 10.9 and 16 cm and six endcap disks organized into three disks with two layers each, at z distances of 29.1, 39.6 and 51.6 cm. The forward acceptance of this tracker is given by $|\eta| < 2.5$

The pixel detector is able to disentangle and reconstruct all the tracks of 10 million particles per square centimetre per second. Each layer is split into two segments, a silicon sensor, $100 \times 150 \mu\text{m}^2$, and an electronic microchip.

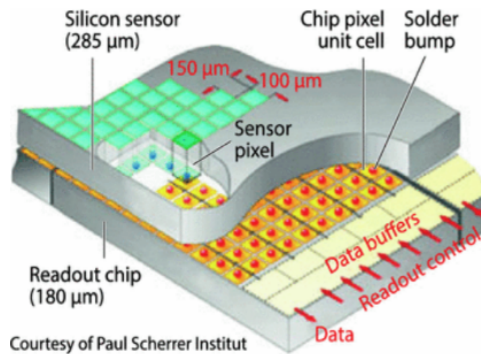


Figure 4: Sketch of a typical CMS pixel sensor

Charged particles passing through pixels create electron-hole pairs. Each pixel uses electric currents to collect these charges on the surface as a small electric signal. An electronic silicon chip, attached to each sensor surface, uses an almost microscopic spot of solder utilizing the so-called bump bonding technique, which amplifies the signal. Knowing which 2D pixels and in which layer has been touched allows us to deduce the 3D particle's trajectory.

As not to overheat the detector, the pixels are mounted on cooling tubes. The barrel is divided into ladders (along the r - ϕ plane) and rings (along the z axis). The intersection is called a module and is made up of 8 or 16 Readout Chips (ROC), each with 52×80 pixels of size $100 \times 150 \mu\text{m}^2$. The ROC reads out the pixel data in double columns, with each double column having its own data and time-stamp buffer. The performance is measured in terms of hit efficiency, which is the probability to find a pixel cluster in any given sensor within a $500 \mu\text{m}$ radius of a well reconstructed charged particle trajectory (isolation, originate from the PV, pass through the active regions of the sensors).

Estimation of the systematic uncertainty for the measurement is made by comparing it to measurements with "ideal tracks" (high transverse momentum, zero IP etc). This way, the systematic uncertainty is approximated to be 0.3%. For a 100 GeV muon, the pixel detector is designed to achieve a 1-2% transverse momentum resolution up to $|\eta|= 1.6$ and around 10 μm transverse impact parameter resolution within $|\eta| < 2.5$.

1.2.1.2 Strip Silicon Detector

A total area of 223 m^2 with axial range of 20-120 cm is covered by 10 millions Strip Silicon Detectors [12]. This part of the tracker contains 15200 highly sensitive modules read by 80.000 microelectronic chips. Each module consists of three elements: a set of sensors, its mechanical support structure and readout electronics. The tracker and its electronics are pummeled by radiation but they are designed to withstand it by operating at -20°C .

While the pixel's goal is to record a limited but accurate subset of three-dimensional information about a particle's trajectory near the interaction point, the strip tracker has the role of recording more rough two-dimensional information about the trajectory across a larger number of measurement surfaces. This allows the strip tracker to obtain a more robust lever arm and hence better measurement of the particle's momentum. The pixel's specialty, in contrast, is the determination of a particle's longitudinal and transverse impact parameter.

As mentioned above, the strip tracker is formed by 4 sub-modules that create a ten layered silicon strip detector, reaching out to a radius of 130 centimetres.

Silicon sensors are highly suited to receive many particles in a small space due to their fast response and good spatial resolution. The silicon detectors work in much the same way as the pixels: as a charged particle crosses the material it knocks electron from atoms and within the applied electric field these move giving a very small pulse of current lasting a few nanoseconds. This small amount of charge is then amplified by APV25 chips, giving us "hits" when a particle passes, allowing us to reconstruct its path.

The charge on each microstrip is read out and amplified by an Analogue Pipeline Voltage (APV25) chip. Four or six such chips are housed within a "hybrid", which also contains electronics to monitor key sensor information, such as temperature, and provide timing information in order to match "hits" with collisions. The APV25 stores the signals in a memory for several microseconds and then processes them before sending to a laser to be converted into infrared pulses. These are then transmitted over a 100m fibre optic cable for analysis in a radiation-free environment. The tracker uses 40,000 such fibre optic links providing a low power, lightweight way of transporting the signal. Much of the technology behind the tracker electronics came from innovation in collaboration with industry. As all CMS silicon sensors, strip detectors are built of n-type silicon. Heavily doped p+ implants are processed in strips into the surface of one sensor side, the so called junction side. Thus, they provide one dimensional information about traversing particles.

The mean energy loss of heavy charged particles is described by the Bethe-Bloch formula. Particles with energy losses near the minimum point of this formula are called minimum ionizing particles (MIPs). All these particles excite electrons from material atoms creating

ionizations.

The distance between two neighbouring strips is called strip pitch P while their width is referred to as implant width W . In the rectangular sensors for TOB and TIB the strip pitch is kept constant whereas in wedge-shaped sensors the strip distance changes from one end of the sensor to the opposite end. This is also true for the implant widths. The opposite wafer side, the ohmic side or backplane, is coated with an unstructured n^+ implant. Moreover, the n^+ implant is required over the entire cutting area of the junction side to avoid edge effects.

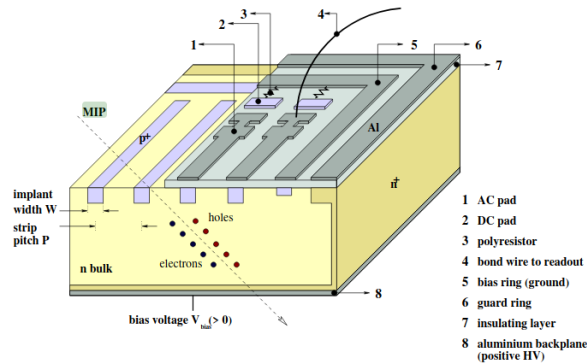


Figure 5: A CMS silicon microstrip sensor.

In the CMS layout, polyresistors connect each strip via a metallized probe pad, called DC pad, to the grounded bias ring which borders the complete sensor by providing all strips with the same potential. A floating guard ring surrounds the strips and the bias ring to gradually degrade the electric field within the sensitive area, and to minimize edge effects. This improves the breakdown performance of the sensors. The p^+ implants are covered with multiple thin insulating layers of SiO_2 and Si_3N_4 on which aluminium strips are deposited parallel to the implants.

The CMS sensor design provides so-called AC coupling as the DC leakage current is bypassed over the polyresistors while the AC part can be picked up over the capacitor built by the metal-oxide-semiconductor interface. Each strip has to be connected to its own readout channel and amplifier. This connection is made with a $25 \mu\text{m}$ thin wire welded onto the corresponding AC pad using an ultrasonic bonding wedge. Two rows of AC pads are used at the ends of the strips on each side of the detector thus allowing for bonding and for testing.

1.2.2 The Electromagnetic Calorimeters

The electromagnetic calorimeter (ECAL) of CMS is a homogeneous and hermetic calorimeter [16]. It is composed of 75848 lead tungstate (PbWO_4) crystals designed to measure the energy of electrons and photons. The whole electromagnetic calorimeter is 7.9 m long and 3.6 m in diameter surrounding the whole tracker detector. Due to the crystal mass it weighs ~ 90 t.

Electromagnetic calorimeters actually measure the energy of particles that interact primarily via the electromagnetic interaction. Electrons and photons are mainly the two types of particles that interact with this interaction, since the first one interacts electromagnetically by emitting a plethora of Bremsstrahlung photons and the latter one interacts with matter via photoelectric effect, Compton scattering and pair production. An electromagnetic calorimeter consists of an active material, where all these processes take place and an absorber where the emitted energy from these processes is detected.

The incoming particle interacts, producing multiple new particles with less energy each time and then each of these particles then interacts in the same way. This process continues until many new low-energy particles are produced. All these new particles are creating a cascade-shower and this process is stopped when the produced particles are not sufficiently energetic and are absorbed by the material. The Molière radius is a characteristic constant of a material giving the scale of the transverse dimension of the fully contained electromagnetic showers initiated by an incident high energy electron or photon. Apart from the Molière radius, materials have another characteristic constant, the radiation length. The radiation length, X_0 , is the amount of matter that an incoming electron needs to traverse in order to emit Bremsstrahlung radiation, or a photon to produce a e^+e^- pair and it is usually measured in $\text{g}\cdot\text{cm}^{-2}$. These characteristic constants need to be low enough to avoid very long and wide calorimeters.

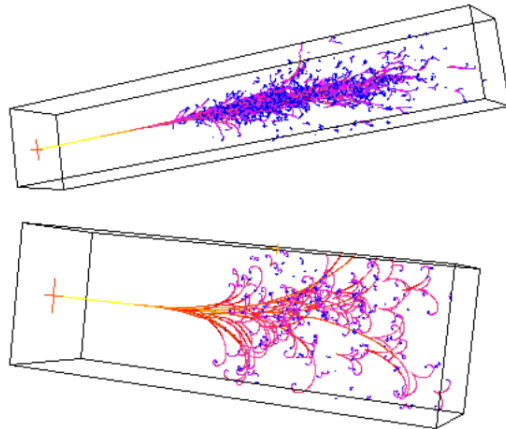


Figure 6: Simulated cascades inside electromagnetic crystals.

Lead tungstate crystal is chosen to be the active material since it satisfies all these prerequisites, it is highly dense (8.28 g/cm^3), it has a short radiation length (0.89 cm) and a small Molière radius (2.2 cm). It is also very fast responding, about 80% of the scintillation light in the crystals is emitted within 25 ns, the LHC bunch crossing time. The crystals are also radiation-hard, with the ability to maintain a good ECAL performance throughout LHC operations. It also peaks in the blue (425 nm) allowing efficient photo detection from photodetectors.

In the barrel region the PbWO_4 crystals are approximately $2.2 \times 2.2 \times 23 \text{ cm}^3$ in size. Crys-

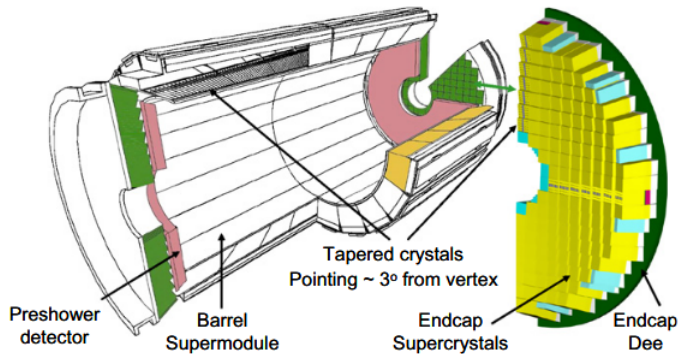


Figure 7: A schematic view of the CMS Electromagnetic calorimeters.

tals are grouped into 36 supermodules, each spanning 20 degree in ϕ . The crystal length corresponds to ~ 26 radiation length X_0 . The endcap electromagnetic (EE) calorimeter crystals are approximately $2.2 \times 2.2 \times 22 \text{cm}^3$ in size, corresponding to $\sim 25X_0$ grouped in a 5×5 unit called supercrystals, which are arranged in the regular x-y grid. All crystals are pointing towards the beamspot. The whole calorimeter was designed to be located in 4T magnetic field. The barrel electromagnetic (BE) calorimeter crystals cover a pseudorapidity range of $|\eta| < 1.479$ whereas the EE covers $1.479 < |\eta| < 3.0$.

The preshower detector is made of layers of lead and silicon strip sensors, is located in front of the endcap electromagnetic calorimeters and is used to identify neutral pions and improves identification of electrons against minimum ionizing particles.

A typical energy resolution [24] measured in EB is found to be

$$\left(\frac{\sigma}{E}\right)^2 = \left(\frac{2.8\%}{\sqrt{E}}\right)^2 + \left(\frac{0.12}{E}\right)^2 + (0.3\%)^2,$$

with E measured in GeV. The first term corresponds to the stochastic term while the second one to the noise and the last one to the constant term. The homogeneous nature of the ECAL crystals reduces the stochastic term by minimizing the lost of scintillation photons in the absorber.

However, the light yield emitted in the active material is rather low (~ 50 photons/MeV), and varies with temperature ($-2\%/C^\circ$ at 18°C). The problem of overheating is solved by using a water cooling system. To avoid any further problems, e.g. with low crystal transparency and/or self-anneal under irradiation at room temperatures, a very precise system for monitoring crystals is used.

The crystals are read out by two different types of photodetectors: silicon based avalanche photodiodes (APD) in the barrel and vacuum phototriodes in the end-caps. Both are running at a high voltage of several hundred Volts. The collected data are transferred to the off-detector electronics for further treatment. The light loss of the crystals occurring during the CMS operation through irradiation and its subsequent recovery is determined by a laser light-injection system.

The APDs in the barrel region are with 75% quantum efficiency and an excess noise factor of 2.1 at the operating gain of 50. They are insensitive to shower leakage particles traversing them. In the Endcaps, where radiation levels are higher and the magnetic field direction is within 25° of the crystal axes, Vacuum Photo-Triodes (VPTs) are deployed. VPTs are photo-multipliers with a single gain stage and were specially developed for CMS. They are with 20% quantum efficiency and a radiation hard UV glass window. They have a typical gain of 10 at 4 T.

The data of 5×5 crystals and their corresponding photodetectors are processed via multiple amplifiers, shaped and digitized to the so-called trigger tower electronics at a rate of 40MHz and after that the information is sent to the level 1 trigger and triggered data are sent to the off-detector electronics. The noise per channel, measured on completed supermodules, is 40 MeV, with an rms spread of 3 MeV.

The ECAL off-detector electronics serves both the DAQ and the Trigger paths. Readout and data reduction is carried out in the DAQ path. In the Trigger path, the Trigger primitives received from the on-detector electronics are synchronised by the Trigger Concentrator Cards and transmitted to the Regional Calorimeter Trigger.

A blue (440 nm) and an infrared (796 nm) wavelength are used to detect any changes in crystal light yield under irradiation like changes in the amount of scintillation light reaching the photodetectors. The light pulses are distributed to the crystals through a system of optical fibres. Temperature, humidity, water cooling system, water flow, voltage supplies etc are also monitored from the ECAL detector control system.

1.2.3 The Hadronic Calorimeters

The CMS hadron calorimeter (HCAL) [15] in cooperation with the ECAL consist a complete calorimetry system for the measurements of jets and missing transverse energy (MET). The measurement of jets and MET is a crucial parameter for identifying many Standard Model processes like QCD multi-jets, top, W +jets, and Z +jets as well as new physics signatures.

In contrast with the electromagnetic cascades the physical processes that cause the creation of a hadron shower are different. Hadron production, nuclear deexcitation and meson decays are the dominant processes for these showers. It is estimated that 1/3 of the produced pions are neutral pions whose energy is dissipated in the form of electromagnetic showers. It is very often that a hadronic shower has also an electromagnetic component which sometimes can be a bit displaced from the hadronic one.

Another important characteristic of the hadronic shower is that it takes longer to develop than the electromagnetic one. This can be seen by comparing the number of particles present versus depth for pion and electron initiated showers. The longitudinal development of hadronic showers scales with the interaction length. For this reason hadronic calorimeters are longer and bigger than the electromagnetic calorimeters, in order to include the whole cascade and avoid as much as possible energy and particles losses from the back parts of the alternating layers of active material and absorber plates. Therefore, their bigger size is responsible to our inability to produce homogenous hadronic calorimeters.

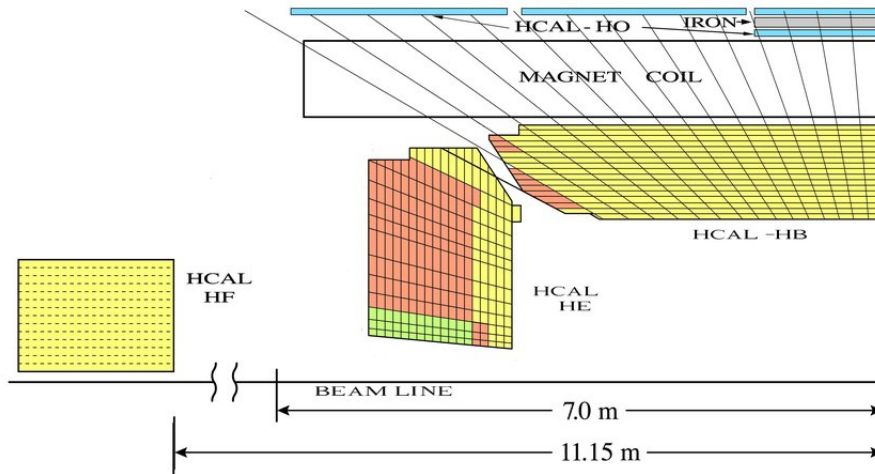


Figure 8: A quadrant of the CMS hadronic calorimeter.

The CMS HCAL is comprised of a set of brass/steel sampling hadron calorimeter. Sampling calorimeters are those,¹ that the material producing the particle shower is distinct from the material that measures the deposited energy. It is designed to measure the energy of charged and neutral hadrons and is located outside of ECAL. The CMS HCAL consists of 4 sub-detectors to cover a wide pseudorapidity range up to $|\eta|=5.2$, known as the barrel and the end-cap (HB, HE) covering $|\eta| < 1.3$ and $1.3 < |\eta| < 3$ range, the forward calorimeter (HF) (see here) and the outer calorimeter (HO). The HCAL barrel (HB) and endcap (HE) detectors surround the electromagnetic calorimeter, and are contained completely within the high magnetic field region of the solenoid.

The HB consists of brass absorbers and plastic scintillators as active materials. The effective HCAL thickness in the region $|\eta| < 1.3$ is extended by the addition of the outerbarrel (HO) scintillators outside the magnet cryostat. Each subdetector spans the full range of the azimuthal angle ϕ . The HB and HE subdetectors consist of layers of plastic scintillator within a brass/stainless steel absorber. These subdetectors are segmented into readout channels. In the regions where $|\eta|$ is greater than 1.74, the ϕ segmentation is more coarsely granulated. Scintillation light, produced in the plastic scintillators is detected by hybrid photodiodes (HPDs).

The interaction length λ , the mean distance travelled by a hadronic particle before undergoing an inelastic nuclear interaction, at $\eta=0$ is equal to 5.82 while it increases up to 10.6 λ at $|\eta| = 1.3$. The ECAL in front of HB adds about 1.1 λ . The scintillators are arranged in trays of tiles called megatiles. The granularity of each tile is $\Delta\eta \times \Delta\phi = 0.087 \times 0.087$ for $|\eta| < 1.6$ and $\Delta\eta \Delta\phi = 0.17 \times 0.17$ for higher $|\eta| \geq 1.6$.

The HO utilizes the solenoid coil as an additional absorber to serve as a tail catcher for late showers to compensate the smaller radiation lengths at low η .

Both HB and HE use hybrid photo-diodes(HPD), HF uses the more radiation resistant

¹In contrast, in the homogenous calorimeters the whole crystal is sensitive and contributes a signal

photomultiplier tube (PMT) and HO uses silicon photomultiplier (SiPM). Since hadronic showers start the development within the ECAL, the hadronic energy resolution depends on both ECAL and HCAL. Due to the sampling nature of HCAL, the energy resolution is generally worse than ECAL. The typical resolution measured to be

$$\left(\frac{\sigma}{E}\right)^2 = \left(\frac{84.7\%}{\sqrt{E}}\right)^2 + (7.4\%)^2$$

If anyone compares the stochastic term of the hadronic calorimetric resolution and the corresponding one from the electromagnetic calorimeter we will notice that in the case of the HCAL, the stochastic term is bigger, since the calorimeter is sampling and not homogenous. The endcap region has similar resolution to the barrel.

1.2.4 The Superconducting Solenoid

S in the CMS abbreviation stands for the Solenoid, the device around which the whole experiment is built, while M stands for the Muons and C for the compact, since a vertical slices of the detector can reveal that there is almost no empty space between the sub-detectors apart from a very thin layer between the solenoid [27] and the muon chambers.

It is located right after the hadronic calorimeter. Its coils are made of superconducting niobium-titanium. Through its coils a 13000 A electric current passing through them creates a powerful 3.8 T magnetic field almost 100,000 times stronger than the Earth’s magnetic field. The solenoid is 13 m long and 6 m in diameter. It was initially designed to produce a 4T magnetic field but the operating amplitude was lowered to 3.8 T in order to prevent it from damage and make it live longer. The inductance of the magnet is 14 H and the nominal current for 4 T is 19,500 A, giving a total stored energy of 2.66 GJ, equivalent to about half-a-tonne of TNT. There are dump circuits to safely dissipate this energy should the magnet quench.

The job of the big magnet is to bend the paths of all charged particles coming from high-energy collisions in the LHC. Tracing a particle’s path leads to measurement of its momentum, since the more momentum a particle has the less its path is curved by the magnetic field. The combination of the magnetic field with the high-precision position measurements from the tracking system and the muon chambers contributes to the accurate measurement of the momentum of even high-energy particles.

The muon detectors are interleaved with a 12-sided iron structure that apart from surrounding the magnet coils it also contains and guides the field. Made up of three layers this “return yoke” reaches out 14 metres in diameter and also acts as a filter, allowing through only muons and weakly interacting particles such as neutrinos. The enormous magnet also provides most of the experiment’s structural support, and must be very strong itself to withstand the forces of its own magnetic field. These iron-made structural support and the return yokes are mainly responsible for the total 12500 tonnes weights of the CMS detector. The return yokes help maintaining a nearly homoge-neous magnetic field throughout the detector volume outside of the Solenoid.

The yoke is composed of common steel and forms five three-layered dodecagonal barrel wheels and three endcap disks at each end. In the barrel region the innermost yoke layer is 295 mm thick and each of the two outermost ones is 630 mm thick. The yoke contributes to only 8% of the central magnetic flux density. Its main role is to increase the field homogeneity in the tracker volume and to reduce the stray field by returning the magnetic flux of the solenoid. In addition, the steel plates play the role of absorber for the four interleaved layers (“stations”) of muon chambers, which provide for a measurement of the muon momentum independent of the inner tracking system.

The magnetic field was well mapped [10] inside the solenoid but not sufficiently measured for the endcaps and the return yokes. During 2008, more than 270 muons from cosmic rays were reconstructed in order to measure the magnetic field efficiently in the barrel return yoke area. However there were not enough muons that penetrated the endcap muon stations and the inner tracker so the accurate mapping of the magnetic field in the endcaps return yokes was very challenging and impossible.

The mapped magnetic flux density on a longitudinal section of the CMS detector is shown in Figure (9). Approximately two thirds of the magnetic flux return through the barrel yoke, half of which enters directly into the barrel without passing through the endcap disks. One third of the total flux escapes radially, returning outside the steel yoke.

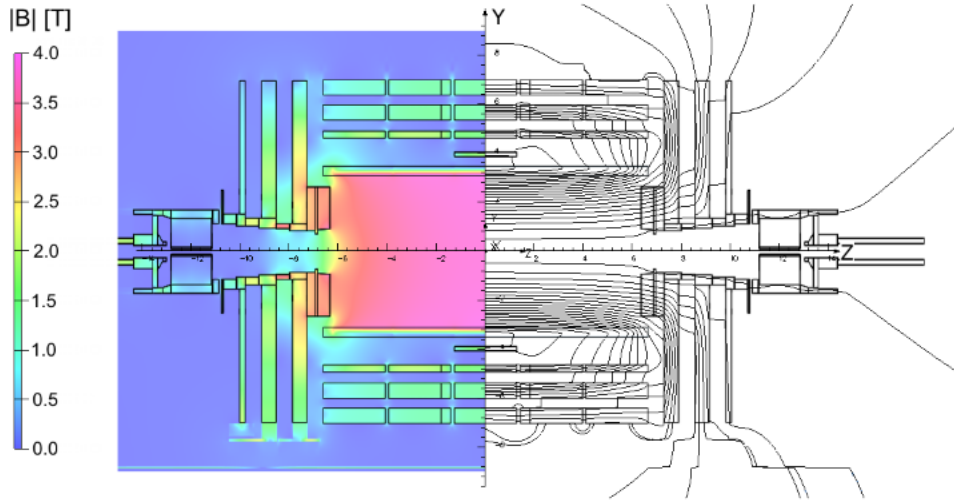


Figure 9: Value of magnetic field (left) and field lines (right) predicted on a longitudinal section of the CMS detector.

The Magnetic Field along the beam axis is parametrized as:

$$B_z(0, z) = \frac{1}{2} B_0 \sqrt{1 + \bar{a}} [f(u) + f(v)]$$

where

$$u = (1 - \bar{z})/\bar{a}$$

$$\begin{aligned}
v &= (1 + \bar{z})/\bar{a} \\
f(x) &= x/\sqrt{1+x^2} \\
\bar{z} &= 2z/L \\
\bar{a} &= 2a/L
\end{aligned}$$

and a = solenoid radius and L its length.

and inside the solenoid region (orange-pink region) the two components of the magnetic field (along the z axis and the polar one respectively) are parametrized as:

$$\begin{aligned}
B_z(r, z) &= \sum_{\nu=0}^{\infty} \frac{(-1)^\nu}{(\nu!)^2} \frac{\partial^{2\nu}}{\partial z^{2\nu}} B_z(0, z) \left(\frac{r}{2}\right)^{2\nu} \\
B_r(r, z) &= \sum_{\nu=0}^{\infty} \frac{(-1)^\nu}{\nu!(\nu-1)!} \frac{\partial^{2\nu-1}}{\partial z^{2\nu-1}} B_z(0, z) \left(\frac{r}{2}\right)^{2\nu-1}
\end{aligned}$$

1.2.5 The Muon Chambers

In the CMS collaboration precise reconstruction and identification of high energy muons is one of the central design concepts. The central purpose was to achieve $\sim 1\%$ dimuon mass resolution for 100 GeV muons and to be able to determine the charge of muons up to 1 TeV. Muons are very important for all analysis since their existence, their detection and their identification can lead to many interesting processes, like $H \rightarrow 4\mu$, $H \rightarrow 2\mu$, or could even lead to many supersymmetric processes since muons are predicted to be the last products of many supersymmetric decay channels. Muons are also reconstructed very easily by creating clear tracks and are widely used as triggering objects in many experiments.

Due to their mass (almost 207 times heavier than electrons), muons emit negligible radiation as Bremsstrahlung radiation, since the emitted power for Bremsstrahlung radiation is $\sim 1/m^2$ where m is the decelerating particle. Muons deposit minimal parts of their energy in all the previous detector layers. A muon creates hits in four stations in the muon chambers. Subsequently hits are combined to create high purity muon tracks. In contrast, electrons and all rest particles are stopped in the electromagnetic and hadronic calorimeters.

Muon detectors [20] are placed outside the solenoid and its magnetic field and more than 3 m away from the collision points, covering the whole body of the detector up to $|\eta| < 2.4$. Owing to muons' importance, three different kind of muons chambers are used for their efficiently reconstruction, identification, and their momentum measurement. All these three sub-detectors are embedded in the flux-return yoke of the magnetic field. An important fact is that all the muon subdetectors use a different technique to reconstruct the muons' trajectories, but all based on gas ionisation chambers. They are known as the Drift Tubes (DTs), the Cathode Strip Chambers (CSCs) and the Resistive Plate Chambers (RPCs). The DTs are covering the barrel region and the CSCs the endcaps region. Both are providing high position resolution with the wire chambers in the r - ϕ plane. RPC are mainly covering the overlapping area of the barrel and the endcap providing additional coverage with fast,

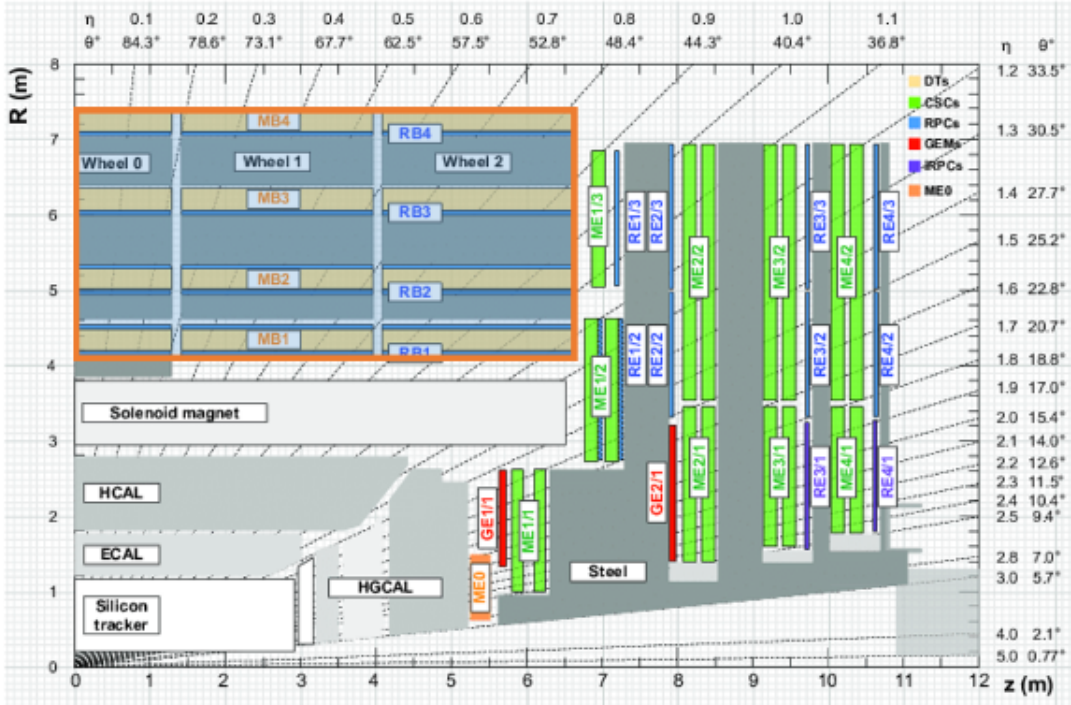


Figure 10: A schematic longitudinal view of one quarter of the CMS detector.

independent and highly segmented detectors for triggering. The muon system can achieve a spatial resolution of about $100 \mu\text{m}$ and a momentum resolution better than 2% for muons with p_T up to about 100 GeV.

1.2.5.1 The Drift Tubes

The DT system [18], [20], cover the $|\eta|$ region up to 1.2, and consists of 4 stations. The basic element of the chambers is a drift tube cell, which is an aluminium cathode cell with a $50\text{-}\mu\text{m}$ -diameter gold-plated anode wire at the center, filled with a gas mixture of Ar (85%) and CO₂(15%). Aluminum strip electrodes shape the electric field to achieve constant drift velocity along the cell as shown in Figure (11). The central wire in the DTs is at a high voltage (3600 V) while the two cathodes on the sides are at -1800 V and the two electrodes above and below the wires are at +1800 V. Free electrons created by the ionizing radiation drift with velocity $\sim 55 \mu\text{m}/\text{ns}$ with a maximum drift time equal to 400 ns in the electric field towards the anode wire where they trigger a signal. The resulting electric pulses are then amplified, digitized with a time-to-digital converter (TDC) and read out. The r - ϕ position resolution in the DTs is around $100 \mu\text{m}$ at each station while the timing resolution in each superlayer is a few nanoseconds.

Twelve layers of parallel drift cells (50 to 100), grouped as shown in the left-side of 1.2.12, consist a DT chamber. Those twelve layers are divided into three superlayers with respect to gas circulation, High Voltage (HV) distribution and Front-End amplifiers (FEB). The first

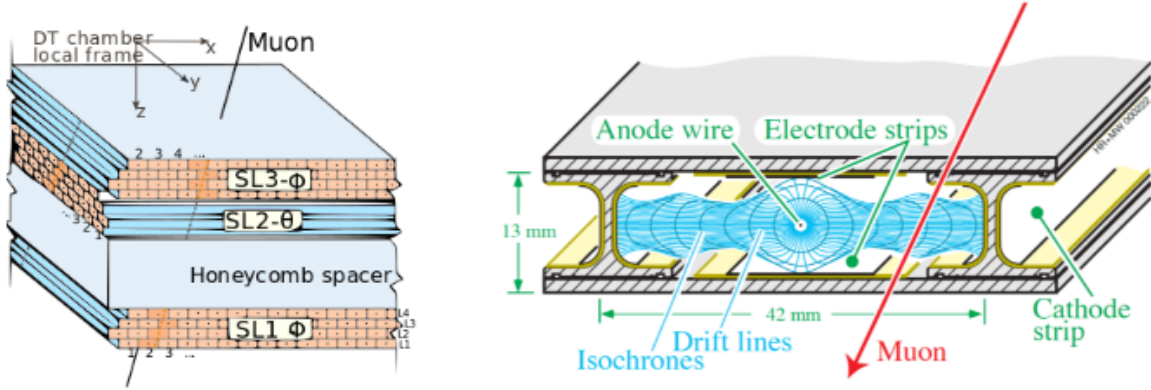


Figure 11: Left: A DT Chamber with three superlayers. Right: A drift cell showing the electric field lines in the gas volume.

and the third group (total 8 layers of tubes) are oriented in the ϕ direction and the second is orthogonal to them (in the Z-longitudinal direction). The honey comb spacer between the second and the third superlayer is a structural element. The DTs create a twelve-sector ring in the longitudinal direction. In each of those sectors there are four concentric chambers or stations labelled from inside out as MB1, MB2, MB3 and MB4 (Muon Barrel). There are two additional chambers in the top and bottom of CMS labelled as sectors 13 and 14. In the outer MB4 stations there is no Z superlayer in the chambers.

1.2.5.2 The Resistive Plate Chambers

The Resistive Plate Chambers (RPCs) [20] are used in both the barrel and the endcap regions providing a faster timing signal and have a different sensitivity to background. They were primarily designed to provide timing information for the muon trigger with a lower p_T threshold over a large portion of the pseudorapidity range ($|\eta| < 1.9$). A RPC consists of two parallel plates (a positively-charged anode and a negatively-charged cathode) of high-resistivity plastic material creating a 2mm thin gap filled with a gas mixture of 96.2% $C_2H_2F_4$, 3.5% C_4H_{10} and 0.3% of SF_6 . As in the DTs, a passing particle creates ionizations by releasing electrons, which are accelerated creating avalanches towards the positively charged side of the chamber. The plastic is transparent to these electrical signals, which are then picked up by external metallic strips.

Resistive Plate Chambers CMS includes a subdetector system with excellent time resolution dedicated to reinforce the measurement of the correct beam crossing time at the highest LHC luminosities. The resistive plate chambers (RPCs) are mounted in both the barrel and end cap regions.

A charged particle passing through the RPC produces an avalanche of electrons in the gap between the two plates. This charge induces a signal on an external strip readout plane to identify muons from collision events with a precision of a few ns. Since a muon passing through the RPC induces a signal on more than one strip, the center of the cluster determines

the position of the RPC hit. They are organised in stations attached to the DT and the CSC. As shown in Figure (10), there are four stations in the barrel (RB1-RB4), and three stations in the endcaps (RE1-RE3), with the inner most barrel stations containing two layers of RPC at both sides of the DT chambers. The rest of the chambers are single-layer only. The RPC strips are used to measure the coordinate in the bending plane. This means that the strips are oriented parallel to the wires of the DT chambers in the barrel, and they are oriented parallel to the CSC strips in the endcaps. The RPC are grouped in wheels/sectors or in rings just as the corresponding DT and CSC chambers.

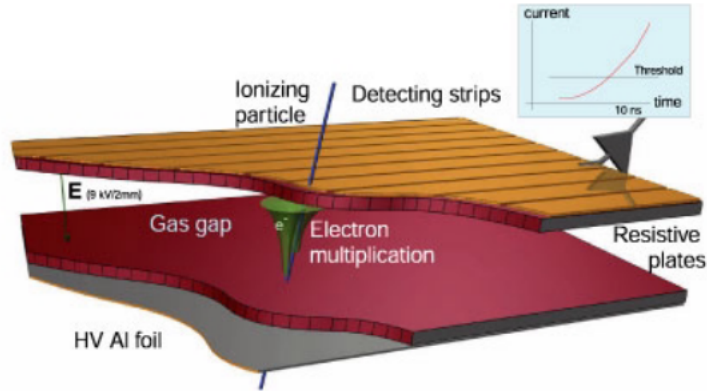


Figure 12: A Muon resistive plate chamber.

While the DTs and CSCs provide fast readout and are able to trigger on the p_T of muons with good efficiency and high background rejection, due to the uncertainty in the eventual background rates at full luminosity, a complimentary detector system was needed. Thus, resistive plate chambers (RPCs) cover both the barrel and endcap regions up to $|\eta| < 1.6$ and provide a relatively lower position resolution but excellent time resolution of ~ 1 ns within the 25 ns bunch separation. There are six layers of RPCs embedded alongside the DTs in the barrel and three layers in the endcaps alongside the CSCs. Overall, RPCs provide a fast response at high rates, with great time resolution and they also help to resolve ambiguities in attempting to make tracks from multiple hits in a chamber.

1.2.5.3 The Cathode Strip Chambers

The Cathode Strip Chambers (CSCs) ([17], [20]) are located only in the end caps region covering the eta region from 0.9 up to 2.4. CSCs have been chosen for this region since the muon rates and background levels are higher and the magnetic field is strong and non uniform and these chambers can provide fast response time and can operate properly in the non-uniform magnetic field. The position resolution of a CSC chamber is around $100 \mu\text{m}$, and the timing resolution is 7 ns. These properties are coming from their short drift path. The fast response time is useful for triggering in the eta region. The basic unit of CSC are multiwire proportional chambers, with an array of anode wires arranged at an angle to the

cathode strips. The CSC chambers are filled with a gas mixture of 50% CO_2 , 40% Ar and 10% CF_4 .

As shown in (13), the shape of a CSC is trapezoidal and they are arranged in such a way that concentric rings centered on the beam line are formed. Each CSC is composed of six staggered layers between two aluminum cathode planes. Each layer measure the muon position in 2 coordinates, the R and ϕ . Their operating principle is similar to that of the Drift Chambers but the main difference is that the applied electric field is stronger. However, in contrast with the DTs, the CSCs are more radiation resistant. The cathode planes are segmented into strips and the strips are interleaved perpendicular with wires.

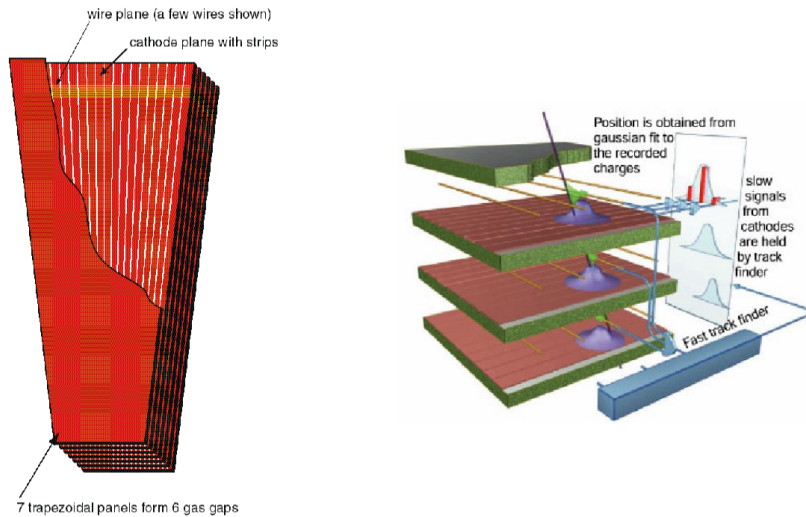


Figure 13: Right: A Cathode Strip Chamber. Left: The creating electric pulses inside a Cathode Strip Chamber from an incoming particle.

The freed electrons, caused by ionization from incoming particles, are collected by the wires, while the positive ions drift to the strips. The intersection point of the cathode strips signal and the anode wires signal determines the hit positions. The wires are measuring the radial coordinate and the strips are measuring the ϕ coordination. An incoming muon, can create ions that will be collected from more than one strip. For this reason the gathered pulses are fitted using gaussian, to estimate the center of the gaussian that corresponds to the hit of the muon's track.

Similar to the barrel region and as shown in Figure (10), the CSCs are grouped in four stations separated by the return iron yokes located perpendicular to the beam axis. They are labelled as ME1/1 up to M4/2. The ME1/1 chambers are operated at an anode voltage of 2900 V since they are closer to collision points and the magnetic field is stronger, and all others at 3600 V. Hence the ME1/1 chambers determine the resolution and the whole alignment since they are vital for the measurement of the distance from center of the bending arc to the center of its base, also known as the sagita. For this reason, the strips that are used for the chambers in this station are narrower.

1.2.5.4 Muon Chambers alignment

With the exception of the central wheel, which is fixed, the other wheels and disks are movable along the beam direction to allow opening the yoke for the installation and maintenance of the detectors. Gravitational distortions lead to static deformations of the yoke elements that generate displacements of the muon chambers with respect to their design position of up to several millimeters. However, the repositioning of the large elements of the yoke after opening and closing of the CMS detector, though rather precise, cannot be better than a few millimeters given their size and weight. In addition, the magnetic flux induces huge forces that cause deformations and movements that may be as large as several millimeters, and these must be carefully tracked by the alignment system. The eleven yoke elements are compressed and slightly tilted. The endcap disks are bent and the central part of the disks is deflected inward by roughly 15 mm. Thermal equilibrium of the yoke is reached after several months of operation, with thermal effects expected in the sub-millimeter range. All these displacements and deformations are either partially or totally non-reproducible, and their typical size is an order of magnitude larger than the desired chamber position accuracy. The CMS alignment system consists of four independent parts: the internal alignment of the tracker, DT, CSC systems, and the Link system.

The muon alignment system [19] is designed to provide continuous monitoring of the muon chamber positions in the entire magnetic field range between 0 T and 4 T, and to meet the challenging constraints of large radiation and magnetic field tolerance, wide dynamic range, high precision, and tight spatial confinement. The whole alignment system is based on a number of precise rigid structures independently supported by the tracker and by each yoke element. These structures contain optical sensors that look at the relative positions of chambers within the same yoke element. The connection among the structures located on the various yoke elements is possible only when CMS is closed, and is obtained through a network of laserbeams, local distance sensors, and digital cameras. The knowledge of detector conditions, such as the magnetic field, is of particular importance for the alignment system. The muon barrel alignment system measures the positions of the DT chambers with respect to each other and to the entire muon barrel.

1.2.6 The Forward Detectors

1.2.6.1 The CASTOR calorimeter

The very forward CASTOR Calorimeter [22] [32], standing for "Centauro And Strange Object Research" at the CMS experiment is a sampling electromagnetic and hadronic calorimeter, located outside from the magnetic field at $z = 14.4$ cm from the interaction point and the main body of the CMS detector covering the pseudorapidity region $5.2 < |\eta| < 6.6$. Castor calorimeters are basically Cherenkov sampling calorimeters. Its effective fibers are made of quartz while its absorbing plates are made of tungsten. Its length is equal to ten interaction lengths and it is segmented in 16 transversal and 14 longitudinal sections. There are two types of fibers within this forward detector: "long" fibers that span the length of the subdetector, and "short" fibers that begin 22 cm into the detector. Differences between

signals read out from the long and short fibers are used to distinguish between electromagnetic and hadronic showers. Photomultiplier tubes (PMTs) connected to the fibers via light guides convert detected light to electrical signals. Since it is very close to the beam pipe it was designed to withstand high ambient radiation and strong magnetic fields.

1.2.6.2 The ZDC Detectors

The Zero Degree Calorimeter (ZDC) [32] detects neutral particles in $|\eta| > 8.5$ region. These detectors are located at $z = \pm 140$ m from the interaction point. In 2016, the ZDC is cross-calibrated to 2010 dataset. The CMS ZDC is able to measure the spectator neutron multiplicity distribution. Its fibres are made up quartz and its effective material is tungsten and its technology is similar with that of the CASTOR calorimeter.

1.2.7 Trigger and DAQ systems

In just one second during the LHC operation, 40 millions p-p collisions take place and fire the subdetectors. Apart from the fact that there is not a possible way to record and store all these petabytes of data, only few of them are coming from deep inelastic scattering that leads to production of new massive particles, like bottom or top quarks, W^\pm/Z mesons or Higgs bosons. Most of the collisions are low-energy not interesting phenomena.

As mentioned above, bunches of protons collide every 25 ns leading to hundreds of new particles. The collision rate is so high that new waves of particles are being generated before those from the last event have even left the detector. The solution to the high recording rate is to store the data in pipelines that can retain and process information from many interactions at the same time. In order not to confuse particles from two different events, the detectors must have a very good time resolution and quick time response, smaller to the time that is required for the next collision. All the electronic channels must be synchronised so as to signals from the same crossing are identified as being from the same event.

The time required to record a complete set of data for each subsystem is ~ 18 minutes for the endcap, ~ 27 minutes for the barrel-endcap overlap, and ~ 2 hours for the barrel. Hence, a “trigger” that can select the interesting events and reduce the rate to just a few hundred events per second, which can be read out and stored on computer disk for subsequent analysis is required. This process, the “garbage cleaning process”, is called “Triggering” and is carried out in two levels, the Level 1 triggering (L1 triggering) and the High Level Triggering (HLT), both aiming to reduce by a factor of 10^6 the rate of data recording.

The CMS trigger decides in real-time which subset of data is to be read out by the detector and archived for offline analysis. The data acquisition (DAQ) system collects the data from the different parts of the detector, converts them into a suitable format and saves it to permanent storage.

The L1 trigger [25] uses the calorimeter, muon system, and global triggers, that combine the data from calorimeters and the muon system. The L1 trigger decides in $3.2 \mu\text{s}$ if the event is to be stored or not by searching for jets, muons, electrons and photons above P_T or η thresholds. According to the L1 triggering process, the event rate from 40 MHz is

The CMS Level-1 trigger design

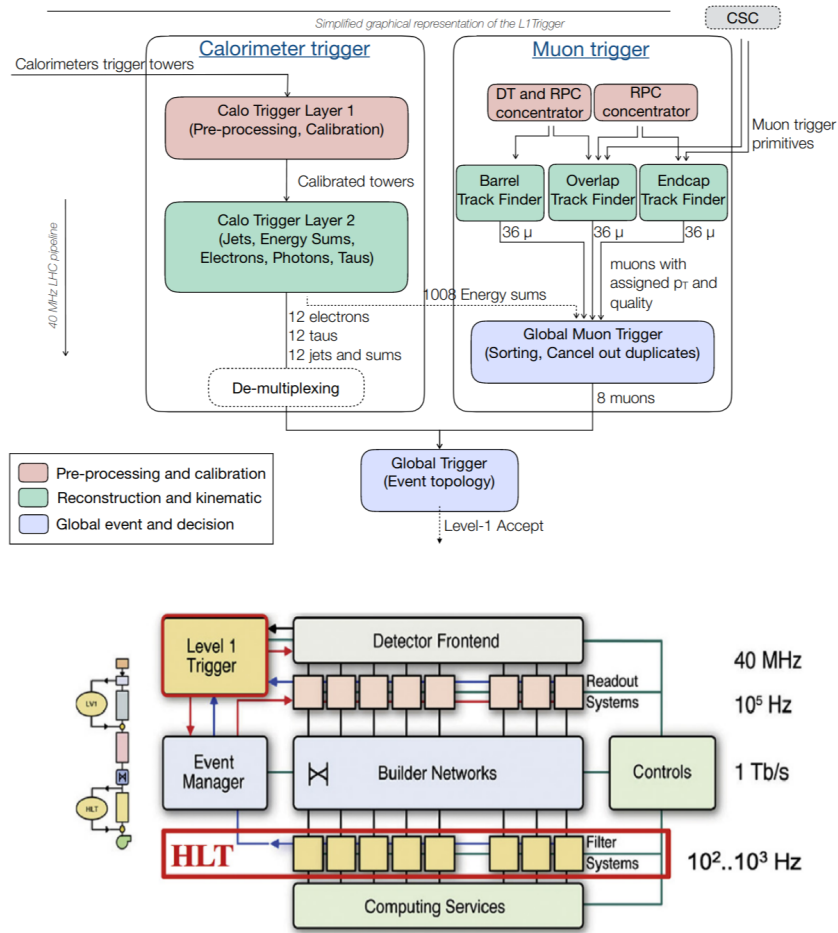


Figure 14: Top: An overview of the L1 triggering system. Bottom: An overview of the CMS triggering system

reduced to 100 kHz. The calorimeter trigger makes use of information from all calorimeters to reconstruct candidate jets, electrons or photons, and τ leptons, as well as the Missing Energy Transverse (MET) in the event.

Similarly, the global muon trigger combines the hit information in RPCs, CSCs, and DTs to reconstruct muon candidates. This two sub-triggers are combined in the global trigger where further information like muon isolation or muon-jet distance is measured. The events that pass these selection criteria are transferred to the HLT for further offline analysis.

The rest part of the events are carried out by the HLT. By the end of this process the event rate is reduced to ~ 100 events/s. During this process, particles that passed the L1 triggering may be re-examined offline and their variables, like the distance from the primary vertex, their P_T or other information may change during the offline reconstruction. Any offline analysis depends on the outcome of HLT.

The HLT software [26] consists of a streamlined version of the offline reconstruction algorithms, optimised to comply with the strict time requirements of the online selection. Particle flow objects, objects that are reconstructed using signals from all detectors like τ leptons and jets, are used in the HLT system. The use of PF reconstruction algorithm in the HLT system improves the energy resolution of trigger objects, increasing their efficiency with respect to offline selection, and provided more refined methods for pile-up mitigation.

2 The Particle Flow and Event Reconstruction

In all particle detector experiments, the process that is followed to interpret the electronic signals recorded in the detectors is called event reconstruction. The purpose of this process is to determine the original particles that created these signals, which means to measure their momenta, directions, primary vertices or even to attribute mass to the tracks and identify completely the particles, so as the initial process that occurred at the interaction point can be determined.

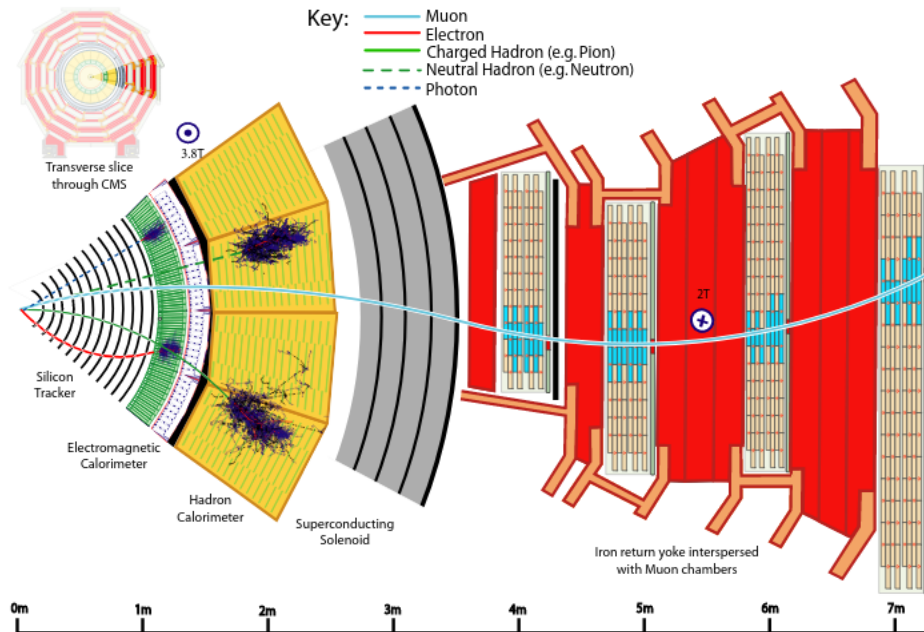


Figure 15: The characteristic signatures of particles in a transverse slice of the CMS collaboration. The muon and the charged pion are positively charged, and the electron is negatively charged.

Produced particles, like electrons, photons, kaons and pions, charged or neutral, are identified based on their specific signatures in the CMS detector. All charged particles are leaving small deposits of their energy, called hits, in the CMS tracking system. In iteration process is used to combine the hits into tracks while at the same time, the curvature of the reconstructed tracks (due to the strong 3.8 T magnetic field) is used to measure the particles' momenta. Electrons and photons, charged and neutral hadrons are absorbed in the ECal and HCal respectively, where measurements of their energy are carried out, while, muons are the only particles that can reach the outermost layers of the detector and create their own tracks in the muon chambers. The energy of electrons is determined from a combination of the electron momentum at the primary vertex as determined by the tracker, the energy of the corresponding ECAL cluster, and the energy sum of all bremsstrahlung photons spatially

compatible with originating from the electron track. On the other hand, neutrinos do not interact with any of the detectors and are completely invisible. However missing energy transverse is usually one hint for the presence of one or more neutrinos. The kinematic properties of final state particles are measured by combining information and signals from different parts of detector.

The collection of advanced algorithms, that are set up to reconstruct all the basic elements, is forming the Particle Flow Algorithm [36]. This collection is composed of two independent steps. The first one is the the reconstruction of the PF elements, which are the tracks, the muon tracks and the calorimeter clusters. The second is the link between the reconstructed objects in different part of the detector, for example the connection bewteen the tracks and their hits in calorimeters.

2.1 Tracks, Primary vertices and Beamspots

2.1.1 Track Reconstruction

As mentioned in the A typical track is made of ~ 15 hits and is characterized by $\sigma(p_T)/p_T \sim 1\text{-}2\%$ at 100 GeV/c and $\sigma(\text{IP}) \sim 10\text{-}20 \mu\text{m}$ at 10-100 GeV/c.

Iteration	Name	Seeding	Targeted Tracks
1	InitialStep	pixel triplets	prompt, high p_T
2	DetachedTriplet	pixel triplets	from b hadron decays, $R \lesssim 5$ cm
3	LowPtTriplet	pixel triplets	prompt, low p_T
4	PixelPair	pixel pairs	recover high p_T
5	MixedTriplet	pixel+strip triplets	displaced, $R \lesssim 7$ cm
6	PixelLess	strip triplets/pairs	very displaced, $R \lesssim 25$ cm
7	TobTec	strip triplets/pairs	very displaced, $R \lesssim 60$ cm
8	JetCoreRegional	pixel+strip pairs	inside high p_T jets
9	MuonSeededInOut	muon-tagged tracks	muons
10	MuonSeededOutIn	muon detectors	muons

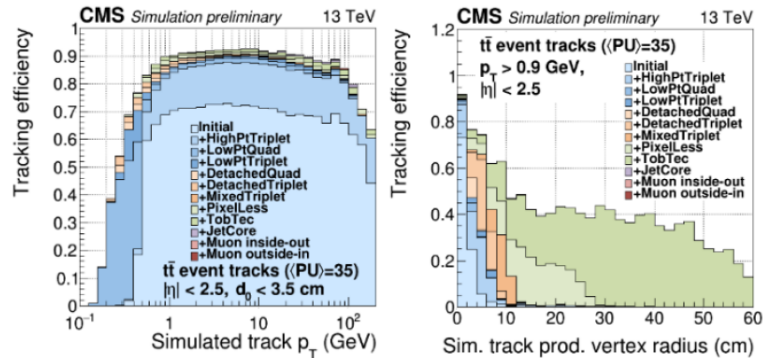


Figure 16: The iterative steps and their associated seeds.

Tracks are reconstructed iteratively in four steps which are called seeding, pattern recognition, final fitting and selection respectively. In the first step, the seeding process "seeds-starting points" are searched in the innermost layers. These seeds are proto-tracks and are consisted of hit pairs and the primary vertex or three hits. The position of the primary

vertices are known thanks to the pixels which are also planned to detect the primary vertices. In the second step, the pattern recognition, the Kalman filter builds the trajectories by propagating the tracks inside-out and searching for compatible hits in the rest layers of the tracking system. Also track parameters are updated. In the third part, trajectories are fitted using a Kalman filter algorithm. After combining all associated hits the Kalman provides the best estimation of the parameters for all trajectories. Missing hits or outlier hits are rejected leading to a refitting process. Finally, in the last step, the selection, tracks are selected based on χ^2 -test and other quality criteria. These criteria aim to reject the ghost and fake tracks.

After each iteration, all hits that have already been used for tracks are removed and the whole process is made again and again. In the initial iteration, high- p_T pixel quadruplets and triplets coming from the beam spot are used as seeds. In the following iterations, seeds are composed of detached pixel triplets, low p_T pixel triplets and pixel pairs. In the following four iterations seeds combine hits from both pixels reaching progressively to even bigger detachments from the beam spots. In the last two iterations muon tracks are seeded from inside-out and from outside-in.

Nuclear interactions in the tracker material may lead to either a kink in the original hadron trajectory, or to the production of a number of secondary particles. On average, two thirds of these secondary particles are charged. Their reconstruction efficiency is enhanced by the sixth and seventh iterations of the iterative tracking. The tracking efficiency and mis-reconstruction rate with all iterations included are displayed in Figure (16). While the displaced-track iterations typically add 5% to the tracking efficiency, they also increase the total misreconstruction rate by 1% for tracks with p_T between 1 and 20 GeV. The relative misreconstruction rate of these iterations is therefore at the level of 20%. A dedicated algorithm was thus developed to identify tracks linked to a common secondary displaced vertex within the tracker volume.

Using simulated data, we can measure the reconstruction efficiency for all iterative steps. We can see that efficiency is increasing reaching a plateau higher than 80% for all iterations. We can also see that this plateau is reached for $p_T > 0.7$. The main reason for this behavior is due to the fact that tracks with lower p_T are the so called loopers, which means that they do not have enough energy to reach neither the electromagnetic calorimeters nor the outer layers of tracker and they indeed loop again again in the tracker until they are absorbed.

Tracks are usually helical. Such a trajectory can be expressed by 6 parameters. In general, these parameters are

- the sign of the radius' curvature which is according to Lorentz force proportional to the particle charge.
- the transverse momentum p_T (units of GeV).
- the azimuthal ϕ angle of the trajectory at a given point on the helix in the plane transverse to the beamline.
- the pseudorapidity η . Pseudorapidity is calculated by $\eta = -\ln(\tan(\frac{\theta}{2}))$ where θ is the track's angle with respect to the transverse plane to the beam axis.

- the impact parameter d_{xy} relative to a reference point (usually beamspots or primary vertices) along the beamline.
- the impact parameter d_z relative to a reference point (usually beamspots or primary vertices) along the beamline.
- the impact parameter or offset d_{xy} relative to a reference point (usually beamspots or primary vertices) in the plane transverse to the beamline.

During the reconstruction, the hit position uncertainty are constantly updated by propagating the available information from inside out. In the last steps of reconstruction removed hits are rejected based on χ^2 criteria, and the reject hits are available for the following iterations. At the same time a smoothing process is followed in order to measure the parameters with the minimum bias and uncertainty.

As mentioned above, the Kalman Filter is used to build the particles' trajectories. This algorithm uses single Gaussians to model the probability for energy losses in the detector material when propagating from layer to layer. However this process is not very effective for electrons' tracks since electrons by emitting Bremsstrahlung photons have high probability for large non-Gaussian energy losses. In order to parameterize these energy losses, mixture of several Gaussians and the Bethe-Heitler model are used.

The iterative process of hits merging to tracks is repeated until some stopping criterion is reached for example when no more detector layers have available hits.

At the end of these processes tracks are labelled as Loose, Tight and HighPurity, according to what criteria and cuts are satisfied. HighPurity tracks are the most well measured and the category that are actually used in almost all cases and analysis.

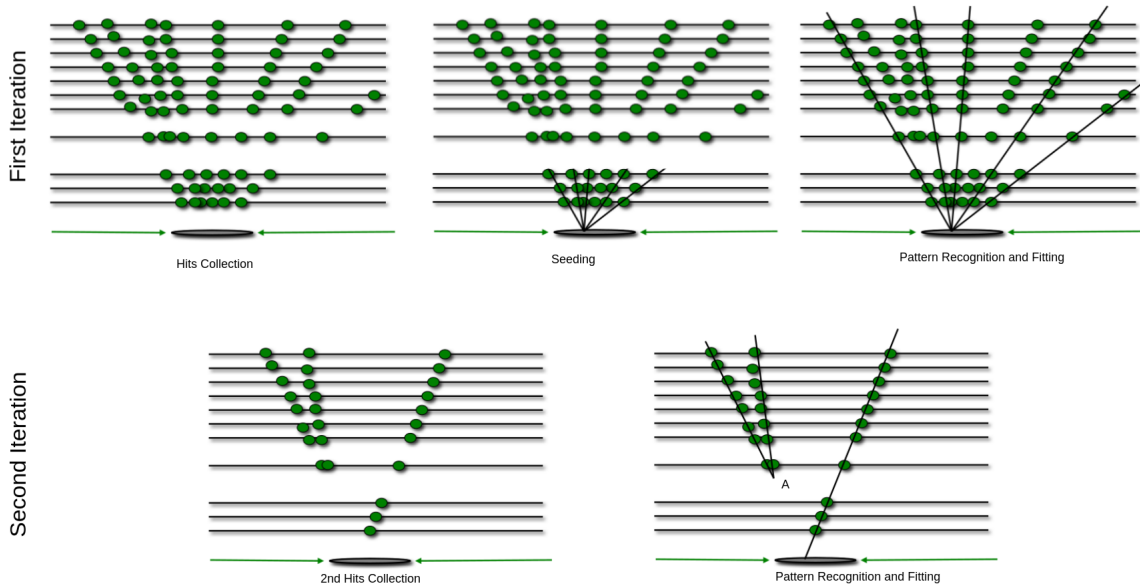


Figure 17: Tracks Reconstruction.

As we can see in Figure (17) two tracks (usually reconstructed during next iterations) can form a new vertex in point A. These vertices are displaced from the beam axis and are the points where unstable particles coming from the primary vertices decayed. Vertices that are even more displaced from the beam axis may be the points where particles from secondary vertices decayed. These vertices are called tertiary vertices.

However, tracking is a time-consuming process and demands most of the computing time of CMS event reconstruction. And this is the reason why tracking can not be used for HLT triggering. Most of the time is spent during pattern recognition especially when hits from strips are checked for their compatibility with the inner parts of the tracks.

A trajectory from one hit to another is extrapolated taking into account the magnetic field (see subsection 1.2.4) and the energy losses due to material effects. This extrapolation is made by using propagators, like AnalyticalPropagator, PropagatorWithMaterial, and RungeKuttaPropagator.

2.1.2 Primary Vertices and Beamspot

For almost all analyses, it is very useful to reconstruct the primary-vertices, the points where two protons interacted, in other words to measure the location and the associated uncertainty of all proton-proton interaction vertices. This reconstruction is comprised of three steps: 1. selection of the tracks, 2. clustering of the tracks that appear to originate from the same interaction vertex, and 3. fitting for the position of each vertex using its associated tracks.

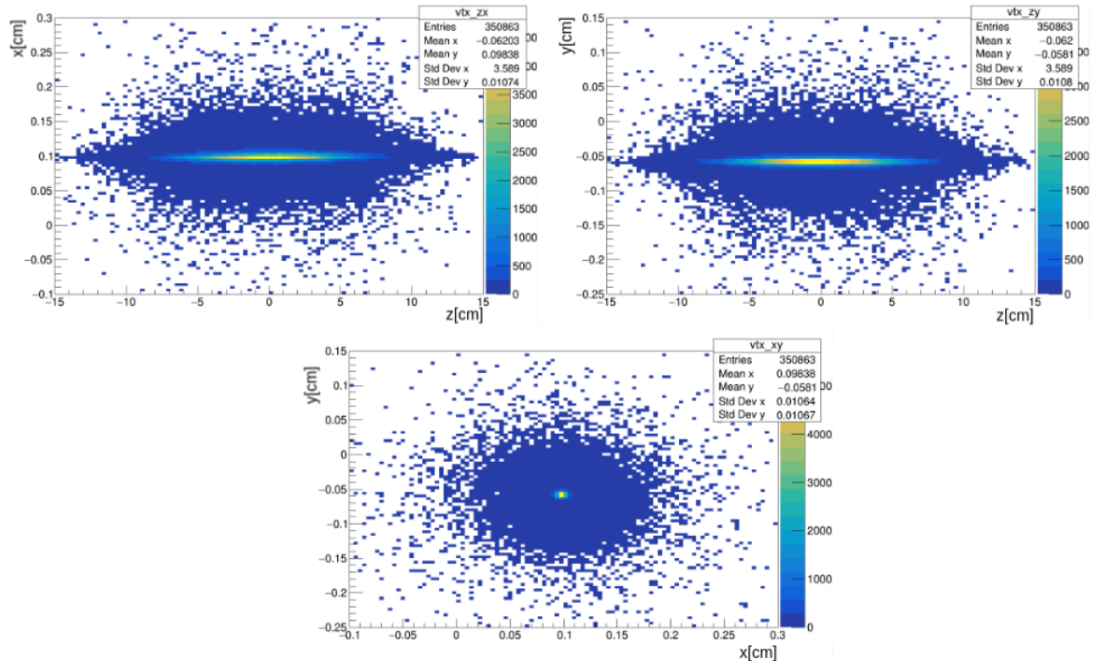


Figure 18: Reconstructed Primary Vertices in data (taken from "Tracking and Vertexing Short Exercise" CMSvDAS 2020).

Tracks are selected by imposing requirements on the maximum value of significance of the transverse impact parameter equal to 5 relative to the centre of the beam spot, the number of strip and pixel hits associated with a track (at least hits in two 2 pixel layers and at least 5 hits in pixel and strips layers), and the normalized χ^2 from a fit to the trajectory ($\chi^2 < 20$). In order to achieve the highest possible reconstruction efficiency, even for minimum-bias events, there is no p_T requirements for the tracks.

The selected tracks are then clustered on the basis of their z-coordinates at their point of closest approach to the centre of the beam spot.

This clustering allows for the reconstruction of any number of proton-proton interactions in the same LHC bunch crossing. The clustering algorithm must balance the efficiency for resolving nearby vertices in cases of high pileup against the possibility of accidentally splitting a single, genuine interaction vertex into more than one cluster of tracks. Track clustering is now performed using a deterministic annealing (DA) algorithm finding the global minimum for a problem with many degrees of freedom.

It is very necessary to distinguish primary vertices from the beamspots. An event can have many primary vertices, each of which usually corresponds to a point in space where two protons collide. The higher the number of primary vertices that are reconstructed the higher the pile-up the event has. The beamspot is an estimation of where protons are expected to collide, derived from the distribution of primary vertices [13]. That means that beamspots are determined from an average over many events, in contrast to the event-by-event primary vertex that gives the precise position of a single collision. Not only does an event have only one beamspot, but the beamspot is constant for a lumi-section (time interval of 23.31 consecutive seconds). In other words, the beam spot is the luminous region produced by the collisions of proton beams or equivalently it represents a 3-D profile of the area where the LHC beams collide in the CMS detector.

The position and spread of the beam spot needs to be measured precisely because of the following six reasons:

1. Important input for physics e.g. b-tagging, lifetime, etc.
2. For patten recognition (input for HLT and offline reconstruction).
3. Extraction of the tracking impact parameter resolution.
4. Quick check of global alignment.
5. Provide feedback to accelerator groups.
6. Beam monitor.

The position of the centre of the beam spot, is used, especially in the HLT, 1 to estimate the position of the interaction point prior to the reconstruction of the primary vertex, 2. to provide an additional constraint in the reconstruction of all the primary vertices of an event and 3. to provide the primary interaction point in the full reconstruction of low-multiplicity data.

Beamsports and primary vertices reconstruction are strongly associated with the detector's alignment since any discrepancy between the assumed and the actual location and surface deformation of detector elements will affect the whole reconstruction process.

2.2 Muons

2.2.1 Muon Tracks Reconstruction

Muon tracking is performed by combing hits from the muon chambers and the inner tracking system ([36],[35],[34]). This procedure is carried out in the $|\eta| < 2.5$ region. Muons' tracks are usually high purity tracks since all particles (except from neutrinos) have been absorbed in the calorimeters. The momentum is measured precisely mainly in the inner tracking system of the CMS. If the P_T of an inner track that is identified as a muon is smaller than 200 GeV, the muon's P_T is chosen to be the P_T of the inner track. Above this value, the momentum is chosen according to the smallest χ^2 probability from the different track fits e.g. global fit, tracker only, tracker and first muon detector plane e.t.c. As muons pass through the magnet return yokes, their trajectories may be affected significantly due to multiple scattering and radiative emissions leading to momentum measurements that are not compatible with their true value. However these problems are avoid by using specialized algorithms for high- P_T muons, like the Tune-P Algorithm, Tracker-Plus_First_Muon_Station, the Picky fit or Dynamic-Truncation fit.

After the reconstruction process, muons are separated in three categories. The first category is made of the standalone muons. The reconstruction of these muons is based on hits patterns that are found in DT or CSC detectors. These patterns are combined with hits along the pattern, and if possible from all kind of chambers. The track that is formed result of this fitting, which is limited only in the muon chambers, is called a standalone muon.

The second category is the tracker muon category. According to this reconstruction all tracks with P_T in range [0.5, 2.5] GeV from the inner detector are extrapolated to the muon chambers. If at least one muon segment (in the muon chambers) is matched to the inner track, the inner track is labelled as a tracker muon track. The matching between the segments and the tracks is made only in the transverse plane. The extrapolated track and the segment are matched either if the absolute value of the difference between the best measured coordination is smaller than 3 cm, or if the ratio of this distance to its uncertainty is smaller than 4.

The last category is composed of global muons. If the parameters of a track in the inner tracker are compatible with that of a standalone tracks and can be propagated onto a common surface, the combined track is forming a global-muon track.

In Figure (15), the muon track is a global muon track. The parts of the trajectory in the muon chambers are forming a standalone muon and the parts of the trajectory in the tracker are forming a tracker muon.

Reconstructing muons as global muons demands hits in at least two muon stations. However, this requirement is satisfied from muons with $P_T > 10$ GeV, since all less energetic muons are scattered in the return yoke. Owing to the high efficiency of the inner track

and muon segment reconstruction, about 99% of the muons produced within the geometrical acceptance of the muon system are reconstructed either as a global muon or as a tracker muon and very often as both. Global muons and tracker muons that share the same inner track are merged into a single candidate. Muons reconstructed only as standalone-muon tracks have worse momentum resolution and a higher admixture of cosmic muons than global and tracker muons.

2.2.2 Muon Identification

However, if a particle shower got away from the calorimeters and reached the muon chambers, the "hits" may be misreconstructed as muons. For this reason, there is a whole set of selection criteria in the PF algorithm (where tracks are identified as particles) to minimize the misreconstruction rate.

Muon Identification, is succeeded by a set of selection criteria based on the global and tracker muon properties.

The first muons that are first selected are the isolated global muons. Global muons are considered to be isolated if the energy deposits in the the calorimeters and the contributions from inner tracks within a $\Delta R \leq 0.3$ from the muon track does not exceed 10% of the muon P_T . This isolation criterion is very sufficient to reject energetic hadrons that could be possibly misidentified as muons.

Loose muon identification is used to identify the prompt muons originating at the primary vertex and muons from both light and heavy quarks aiming to maintain the low rate of misidentification of charged hadrons as muons. Loose muons can be both tracker or global muons.

Muons are identified as medium if they are prompt muons or they are coming from heavy flavor decays. Different reconstruction criteria (e.g. for the number of the hits or for the compatibility of the segments with the tracker track) are used for this identification if the muon is reconstructed as a tracker muon or as both a tracker muon and a global muon.

However, if muons are coming in flight from semileptonic heavy-flavour decays or from jets, more criteria are required to be identify correctly. On the one hand, unidentified muons will be considered as neutral hadrons and on the other hand, misidentified hadrons as muons will lead to additional fake neutral particles. So for these nonisolated muons the tight muon selection is applied. Tight muon ID also aims to suppress muons from hadronic punch-through. According to this selection, the global track (which is now reconstructed outside-in requiring $\chi^2/\text{ndf} < 10$) must be reconstructed with at least two matched segments in the muon chambers, more than 10 inner-tracker hits with at least one pixel hit and have a transverse impact parameter $|d_{xy}| < 2$ mm and a longitudinal impact parameter $|d_z| < 0.5$ cm with respect to the primary vertex. Otherwise, three matching track segments in the muon detectors are required or the calorimeter deposits associated with the track must be compatible with the muon hypothesis in order to a muon track be identified as a tight muon. Muons may fail the tight-muon selection due to poor global fit or poorly reconstructed inner track due to hit confusion. Tight Muons are used in many physics analyses in CMS, in particular in the measurements of inclusive W and Z cross sections.

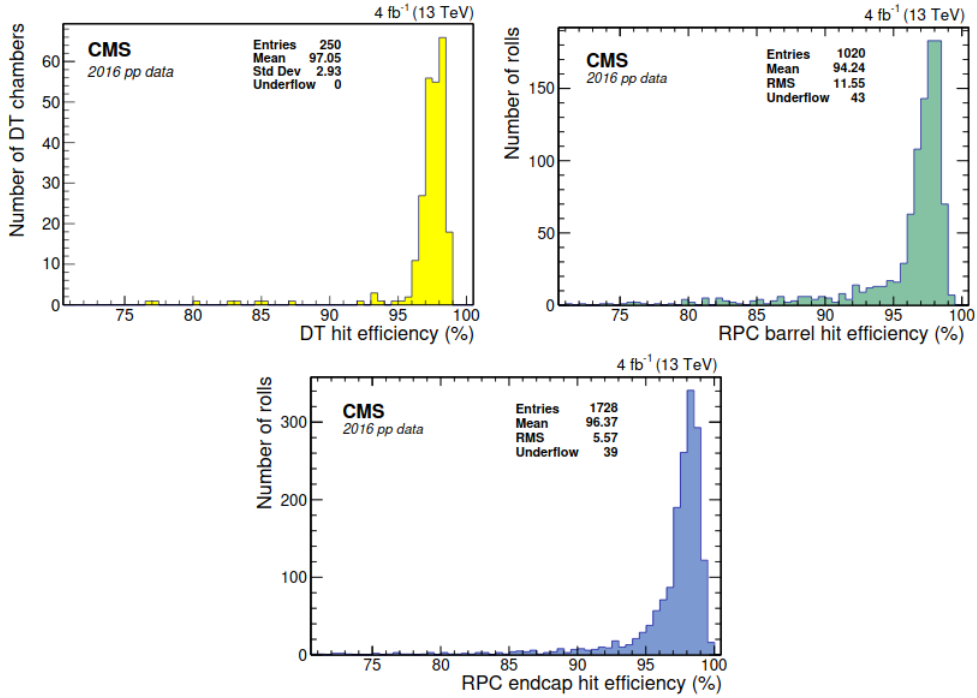


Figure 19: Hit reconstruction efficiency measured with the 2016 data in (upper left) DT, (upperright) RPC barrel, and (lower) RPC endcap chambers.

Soft muon ID is optimized for low- P_T muons for B-physics and quarkonia analyses. A soft muon is a tracker muon with a tracker track that satisfies a high purity flag and uses hits from at least six layers of the inner tracker including at least one pixel hit. The tracker muon reconstruction must have tight segment matching, having pulls for the two coordinators in the transverse plane less than 3. A soft muon is loosely compatible with the primary vertex, having $|d_{xy}| < 0.3$ cm and $|d_z| < 20$ cm.

If a muon's P_T is higher than 200 GeV, then the muon is identified as a high momentum muon. These muons are reconstructed both as a tracker muon and a global muon in a similar way with the one followed in the tight muon identification except for the χ^2 cut. To avoid any mismeasurements due to high relativistic radiations a relative P_T uncertainty $\sigma(P_T)/P_T < 30\%$ is required.

The PF elements that make up these identified muons are not used to build any other PF elements for other particles.

Finally, muons are labelled as tag and probe. This identification is based on a data-driven technique for measuring particle detection efficiencies. According to this identification, reconstructed muons that pass tight selection criteria and fired at least one of the triggers are labelled as tag and all the rest unbiased set of muon candidates, that satisfy very loose selection criteria are labelled as Probe muons.

The μ -reconstruction efficiency as a function of η for tight and loose muons is depicted

in Figure (20). The hit reconstruction efficiency for the three types of muon chambers is depicted in Figure (19).

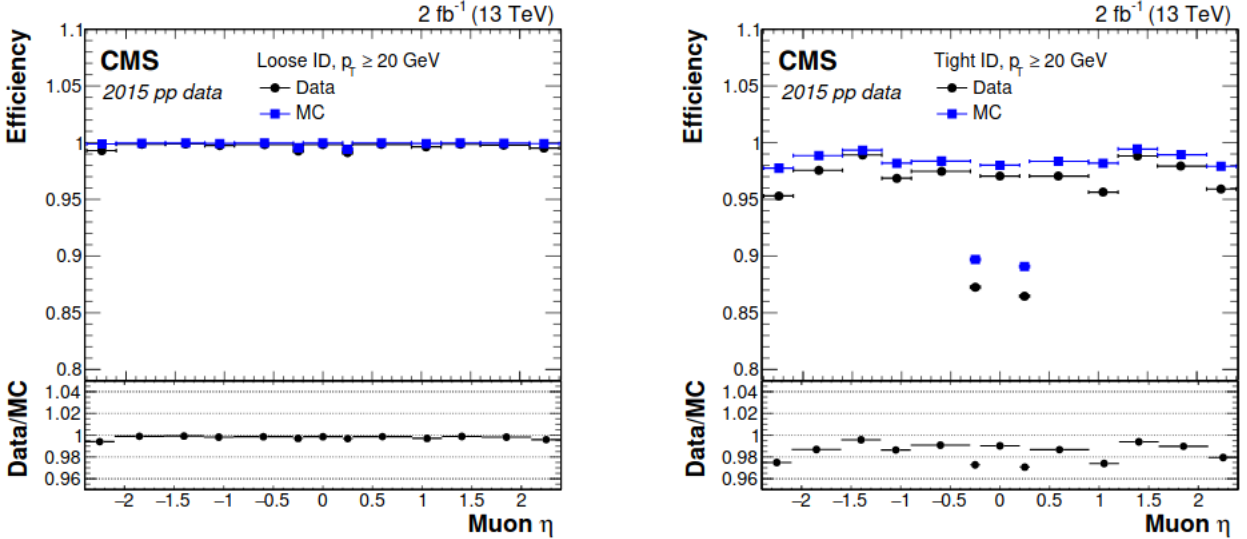


Figure 20: The reconstruction + ID efficiency for loose (left) and for tight muons (right) as a function of η for both data (2015) and simulation.

The total muon reconstruction can be described as a very effective process since the hit reconstruction efficiency is 94-99%, the reconstruction and identification efficiency is more than 96% and the isolation efficiency is more than 95%, while the hit spatial resolution is 50-300 μ m and the timing resolution is <3ns.

2.2.3 High Level Triggering Muons

Muons, due to their effective and precise reconstruction are widely used as triggering objects. The process for this process is made in two steps [38]. During the first step, Level-2 (L2) the muon is reconstructed in the muon chambers only, while in the second step, the Level-3 (L3), a global fit is used to match the hits in the muon spectrometers with a track from the tracking system, which means that for High Level Triggering (HLT) Muons, the reconstructed P_T is mainly seeded by the hits in the muon chambers which is in contrast with the fact that all tracks are seeded by the hit-triplets from the tracker.

The reconstruction for HLT muons starts with the reconstruction of the local hit positions within the different muon detectors, where hits inside the multi-layer DT and CSC chambers are combined in “track segments”. Then, the segments are used to create an initial state (seed), which is the starting point for the Kalman filter that fits a track through the muon spectrometer. After the track reconstruction in the muon chambers, the L2 candidates are filtered on the track quality and p_T^{L2} .

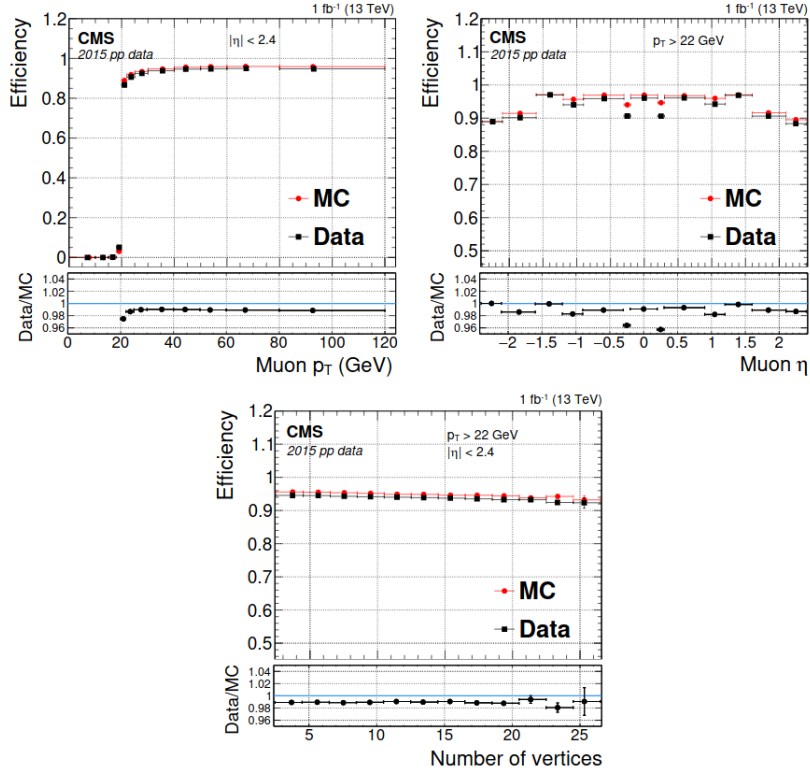


Figure 21: Trigger reconstruction efficiency [35] as a function of offline reconstructed P_T and η measured with 2015 data and simulated events fired Isolated single-muon trigger with HLT P_T threshold at 20 GeV. The efficiency as a function of reconstructed muon P_T (top-left) rises sharply at the threshold. Above 22 GeV, the inefficiency of a few percent is primarily caused by the L1 trigger and the relative isolation criteria. Variations in efficiency as a function of η are caused by geometrical features of the detector that affect the L1 trigger efficiency. The isolation requirement is responsible for the mild efficiency drop as a function of the number of offline reconstructed vertices.

The reconstructed L2 Muon track is used to point a small volume of the tracker, where the reconstructed hits are used to extrapolate the muon track to the tracker area firing the L3 Muon reconstruction.

This is followed by the seeding step that initiates the Kalman filter. The track reconstruction needs to balance quality with speed. Therefore there are 3 different seeding algorithms, depending on whether the seeding is Outside-In or Inside-Out and whether only tracker or muon system information is used. If the first (fastest) algorithm fails to reconstruct a L3 Muon, then the next algorithm is used. The L3 candidates are again filtered on quality, P_T^{L3} and a beamspot constraint before the event is accepted or rejected.

After the track reconstruction process, relative isolation requirements ($\Delta R < 0.03$) or $\Delta z < 0.2$ cm with respect to the PV can be used to reduce the rate, correct the tracks and to allow for lower P_T^{L3} threshold.

2.3 Calorimeter Clustering, Electrons and Photons

The two major contributions for the deposits in the electromagnetic calorimeter are the electrons and the photons ([36],[33]), since all hadrons are expected to deposit their energy in the hadronic calorimeter. However, electrons are charged leptons and photons are neutral particles, so the first are producing hits in the tracker layers while the latter are detected directly from their hits in the electromagnetic crystals. In front of the ECal, there is significant amount of material that forms the tracker detector, thus electrons and photons may interact with the material and the electrons may emit bremsstrahlung photons and the photons may convert into an electron-positron pair.

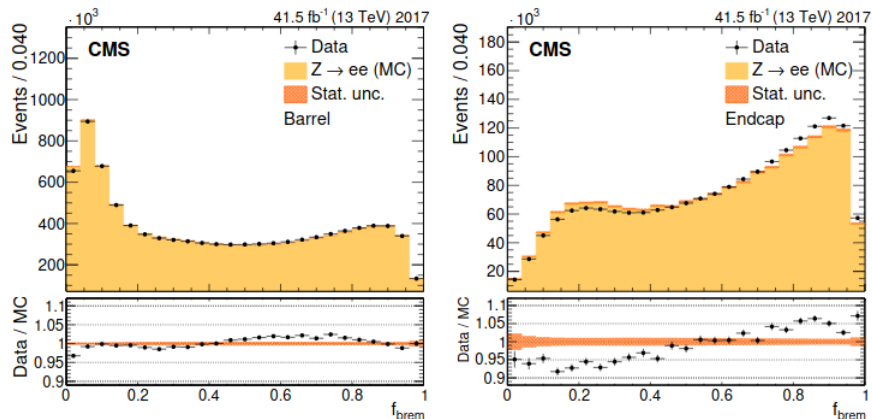


Figure 22: Fraction of the momentum lost by bremsstrahlung between the inner and outer parts of the tracker for electrons from Z boson decays in the barrel (left) and in the endcaps (right). The upper panels show the comparison between data and simulation. The lower panels show the data-to-simulation ratio.

Hence, by the time the electron or photon reaches the ECAL, it may no longer be a single particle, but it could consist of a shower of multiple electrons and photons. A dedicated algorithm is used to combine the clusters from the individual particles into a single object to recover the energy of the primary electron or photon. Furthermore, the electron that losing more and more energy by emitting bremsstrahlung photons, has less and less momentum, creating a trajectory whose curvature changes in the tracker material.

A dedicated tracking algorithm, based on the Gaussian sum filter (GSF), is used for electrons to estimate the track parameters. This process is carried out in 9 steps.

According to the first step, the reconstruction starts by gathering crystals with energies exceeding a threshold (typically ~ 80 MeV in EB and ~ 300 MeV in EE), which is generally 2 or 3 times bigger than the electronic noise expected for these crystals. The crystal that is containing most of the energy deposited in any specific region with a minimum transverse energy above 1 GeV is defined as the seed cluster. The traditional electron seeding strategy, uses ECAL clusters with $E_T > 4$ GeV. For a particle of mass m and transverse momentum P_T is defined as $E_T = \sqrt{m^2 + P_T^2}$. The cluster energy and position are used to infer the

position of the hits expected in the innermost tracker layers under the assumptions that the cluster is produced either by an electron or by a positron.

During the second step, the superclustering step, superclusters (SC) are formed by combining clusters within a certain geometric area ($\Delta\eta, \Delta\phi$) to include photon conversions and bremsstrahlung losses. Because of the significant tracker thickness, most of the electrons emit a sizeable fraction of their energy in the form of bremsstrahlung photons before reaching the ECAL. The performance of the method therefore depends on the ability to gather all the radiated energy, and only that energy. The energy of the electron and of possible bremsstrahlung photons is collected by grouping into a supercluster. The ECAL clusters reconstructed in a small window in η and an extended window in ϕ around the electron direction. The ϕ window is more wide to account the azimuthal bending of the electron in the magnetic field. For electrons in jets, however, the energy and position of the associated supercluster are often biased by the overlapping contributions from other particle deposits, leading to large inefficiencies. In addition, the backward propagation from the supercluster to the interaction region is likely to be compatible with many hits from other charged particles in the innermost tracker layers, causing a substantial misreconstruction rate. To keep the latter under control, the ECAL-based electron seeding efficiency has to be further limited, e.g. by strict isolation requirements, to values that are unacceptably small in jets when a global event description is to be achieved. Similarly, for electrons with small P_T , whose tracks are significantly bent by the magnetic field, the radiated energy is spread over such an extended region that the supercluster cannot include all deposits.

In the third step, trajectory seeds in the pixel detector that are compatible with the SC position and the trajectory of an electron are used to seed the fourth step, the GSF tracking step. In step five, generic tracks, tracks with $P_T > 2$ GeV reconstructed from hits in the tracker through an iterative algorithm known as the Kalman filter, are used to find whether they originate from photons converting into e^+e^- pairs. Then, in the sixth step, ECAL clusters, SCs, GSF tracks and generic tracks associated with electrons, as well as conversion tracks and associated clusters, are all imported into the PF algorithm that links the elements together into blocks of particles. Subsequently, step seven, these blocks are resolved into electron and photon (e and γ) objects, starting from either a GSF track or a SC, respectively. The linked ECAL clusters for each candidate is promoted to a refined supercluster. After this process there is not a differentiation between electron and photon candidates. In the prefinal step, electron or photon objects are built from the refined SCs based on loose selection requirements. All objects passing the selection with an associated GSF track are labeled as electrons and without a GSF track they are labeled as photons. This collection is known as the unbiased e/γ collection. In the final step, electrons and photons are separated from hadrons in the PF framework, since a tighter selection is applied to all e/γ objects to decide if they are accepted as an electron or as an isolated photon. If the e/γ object passes both the electron and the photon selection criteria, its object type is determined by whether it has a GSF track with a hit in the first layer of the pixel detector. If it fails the electron and photon selection criteria, its basic elements (ECAL clusters and generic tracks) are further considered to form neutral hadrons, charged hadrons or nonisolated photons in

the PF framework.

In a given PF block, an electron candidate is seeded from a GSF track, provided that the corresponding ECAL cluster is not linked to three or more additional tracks. A photon candidate is seeded from an ECAL supercluster with E_T larger than 10 GeV, with no link to a GSF track. For ECAL-based electron candidates and for photon candidates, the sum of the energies measured in the HCAL cells with a distance to the supercluster position smaller than 0.15 in the (η, ϕ) plane must not exceed 10% of the supercluster energy. To ensure an optimal energy containment, all ECAL clusters in the PF block linked either to the supercluster or to one of the GSF track tangents are associated with the candidate. Tracks linked to these ECAL clusters are associated in turn if the track momentum and the energy of the HCAL cluster linked to the track are compatible with the electron hypothesis. The tracks and ECAL clusters belonging to identified photon conversions linked to the GSF track tangents are associated as well. The total energy of the collected ECAL clusters is corrected for the energy missed in the association process, with analytical functions of E and η . These corrections can be as large as 25% at $|\eta| \approx 1.5$ where the tracker thickness is the largest. This corrected energy is assigned to the photons, and the photon direction is taken to be that of the supercluster. The final energy assignment for electrons is obtained from a combination of the corrected ECAL energy with the momentum of the GSF track and the electron direction is chosen to be that of the GSF track.

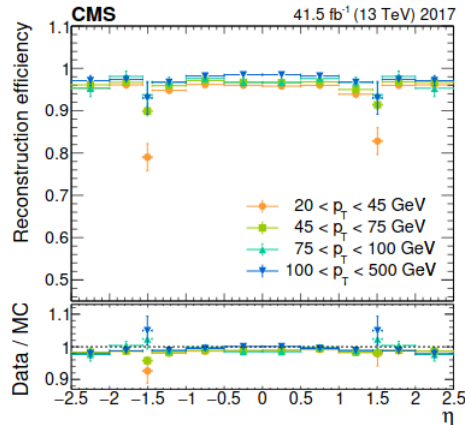


Figure 23: Electron reconstruction efficiency as a function of η for the 2017 data taking period [33]. The region $1.44 < |\eta| < 1.57$ corresponds to the transition region between the barrel and endcap regions of ECAL and is not considered in physics analyses.

Electron candidates must satisfy additional (up to fourteen) identification criteria, like the amount of energy radiated off the GSF track, the distance between the GSF track extrapolation to the ECAL entrance and the position of the ECAL seeding cluster and many others. Photon candidates are retained if they are isolated from other tracks and calorimeter clusters in the event, and if the ECAL cell energy distribution and the ratio between the HCAL and ECAL energies are compatible with those expected from a photon shower.

3 Electroweak theory and Flavour Changing Neutral Currents

In the 1960s, Glashow, Salam and Weinberg (GSW) developed a unified picture of the electromagnetic and weak interactions. At low energy, electromagnetism and weak interactions seem to be quite different, since the first one appear to extend in great distances while the latter extends only across the atomic distances, or even to smaller distances. However, it was proved that these two forces are just two different facets of a single and fundamental electroweak force. Apart from the unification, the CSW electroweak model predicts the weak neutral current propagated by the neutral Z boson. From the mathematical point of view the two forces are unified as a $SU(2) \times U(1)$ Yang-Mills gauge theory. The term "gauge theory" means that the Lagrangian does not change under local transformations and the "Yang-Mills" term means that the gauge theory is based on non-Abelian Special Unitary $SU(N)$ group. Apart from these characteristics the electroweak theory should be renormalizable, that means that it should not contain non physical infinite quantities.

3.1 Electrodynamics as a Gauge Theory

Gauge invariance is already known from electromagnetism ([37],[23],[31]) where the electric field \vec{E} and the magnetic field \vec{B} , which are obtained from the scalar and vector potentials Φ and \vec{A} respectively, do not change under the gauge transformation:

$$\Phi(t, \vec{x}) \rightarrow \Phi'(t, \vec{x}) = \Phi(t, \vec{x}) - \frac{\partial \chi(t, \vec{x})}{\partial t} \quad \vec{A}(t, \vec{x}) \rightarrow \vec{A}'(t, \vec{x}) = \vec{A}(t, \vec{x}) + \vec{\nabla} \chi(t, \vec{x}) \quad (3.1)$$

For simplicity, from now on, the time-space dependence of the two potentials and of the scalar function χ will be omitted. This gauge transformation can be written in a common way using indices, as:

$$A_\mu \rightarrow A'_\mu = A_\mu - \partial_\mu \chi \quad (3.2)$$

where² $A_\mu = (\Phi, -\vec{A})$ is the four-vector electromagnetic potential and $\partial_\mu = (\partial_t, \vec{\nabla}) = \left(\frac{\partial}{\partial t}, -\frac{\partial}{\partial x}, -\frac{\partial}{\partial y}, -\frac{\partial}{\partial z} \right)$

It is easy to prove that the Electric field \vec{E} and the magnetic field \vec{B} , defined as:

$$\vec{E} = -\vec{\nabla} \Phi - \frac{\partial \vec{A}}{\partial t} \quad \vec{B} = \vec{\nabla} \times \vec{A} \quad (3.3)$$

is invariant under the (3.1) transformations.

In relativistic quantum mechanics, the gauge invariance of electromagnetism can be related to a local gauge principle. Let's suppose that a Dirac spinor Ψ is transformed using a local gauge transformation as following:

$$\Psi(x) \rightarrow \Psi'(x) = \hat{U}(x) \Psi(x) = e^{iq\chi(x)} \Psi(x) \quad (3.4)$$

²for simplicity the time-space dependence has been omitted. Another usefull notation is using just the x letter without any vector or index that corresponds to four-vector $x=(t, \vec{x})$.

where the phase $q\chi(x)$ can be different at all points in space-time.

The free Dirac equation

$$i\gamma^\mu\partial_\mu\Psi = m\Psi \quad (3.5)$$

in order to satisfy the Lorentz invariance under the (3.4) U(1) local phase transformation needs to be modified as following:

$$i\gamma^\mu(\partial_\mu + iqA_\mu)\Psi = m\Psi \quad (3.6)$$

Let's focus for a while on the term $q\gamma^\mu A_\mu\Psi$. This term is the Quantum Electrodynamics's (QED) interaction term. The requirement that physics is invariant under local U(1) phase transformations implies the existence of a gauge field which couples to Dirac particles in exactly the same way as the photon. This is a profound statement that all of QED, including ultimately Maxwell's equations, can be derived by requiring the invariance of physics under local U(1) transformations of the form

$$\hat{U}(x) = e^{iq\chi(x)} \quad (3.7)$$

The QED Lagrangian density, which will be called simply Lagrangian from now on and for the rest of this thesis, is give by:

$$\mathcal{L} = \bar{\Psi}(i\gamma^\mu\partial_\mu - m)\Psi + e\bar{\Psi}\gamma^\mu\Psi A_\mu - \frac{1}{4}F_{\mu\nu}F^{\mu\nu}, \quad (3.8)$$

where Ψ is the Dirac (4×1) spinor for fermions with mass m , $\bar{\Psi} = \Psi^\dagger\gamma^0$, the adjoint spinor multiplied from right with the γ^0 Dirac matrix, $\gamma^\mu = (\gamma^0, \gamma^1, \gamma^2, \gamma^3)$ the four Dirac γ -matrices, that satisfy the property $\{\gamma^\mu, \gamma^\nu\} = \gamma^\mu\gamma^\nu + \gamma^\nu\gamma^\mu = 2\eta^{\mu\nu}$, $A^\mu = (\Phi, \vec{A})$ and $F^{\mu\nu} = \partial^\mu A^\nu - \partial^\nu A^\mu$ the electromagnetic tensor.

In this Lagrangian the term $\mathcal{L} = \bar{\Psi}(i\gamma^\mu\partial_\mu - m)\Psi$ is the kinetic term of the fermion, the second term is the interaction term and the last one is the kinetic term of the electromagnetic field. Terms of the $\sim m^2 A_\mu A^\mu$ form are forbidden in this lagrangian since the A^μ field must remain massless.

If we demand the Euler-Lagrange equations,

$$\partial_\mu\left(\frac{\partial\mathcal{L}}{\partial(\partial_\mu A_\nu)}\right) - \frac{\partial\mathcal{L}}{\partial A_\nu} = 0, \quad (3.9)$$

for the A^μ fields and we keep in mind that the term $e\bar{\Psi}\gamma^\mu\Psi$ is the electromagnetic current J_{EM}^μ , then we will end up with the equation

$$\partial_\mu F^{\mu\nu} = J_{EM}^\nu, \quad (3.10)$$

which includes the two of the four Maxwell equations. In order to reveal the other two equations, we need to use the Jacobi identity for the antisymmetric tensors

$$\partial_\kappa F_{ij} + \partial_i F_{j\kappa} + \partial_j F_{i\kappa} = 0. \quad (3.11)$$

The free photon field A_μ can be written in terms of a plane wave and a four-vector $\varepsilon_\mu(\lambda)$ for the polarisation state λ ,

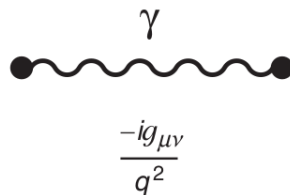
$$A_\mu = \varepsilon_\mu^\lambda e^{i(\vec{p}\cdot\vec{r} - Et)}. \quad (3.12)$$

For a real photon (and not for a virtual), the polarisation vector is always transverse to the direction of motion. Hence, a photon propagating in the z-direction can be described by two orthogonal polarisation states $\varepsilon^{(1)} = (0, 1, 0, 0)$ and $\varepsilon^{(2)} = (0, 0, 1, 0)$.

Finally, the sum over the polarisation states of the virtual photon which is the propagator for the QED is associated with the $g_{\mu\nu}$ term

$$\sum_\lambda \varepsilon_\lambda^\mu \varepsilon_\lambda^{*\nu} = -g^{\mu\nu} \quad (3.13)$$

in the Feynman rule for QED.



$$\frac{-ig_{\mu\nu}}{q^2}$$

Figure 24: The Feynman propagator for QED where q^2 is the propagated momentum.

3.2 Weak Interactions as Gauge Theory

The weak interactions are responsible for the radioactive decay of nuclei and for subatomic interactions which can change the flavor of a particle. These interactions are mediated by the exchange of both electric charged bosons W^\pm and neutral bosons Z^0 .

3.2.1 Weak Isospin Doublets and Singlets

Heisenberg suggested that if someone could switch off the electric charge of the proton, there would be no way to distinguish between a proton and a neutron. To reflect this observed symmetry of the nuclear force, it was proposed that the neutron and proton could be considered as two states of a single entity, the nucleon, analogous to the spin-up and spin-down states of a spin-half particle. This led to the introduction of the idea of isospin, where the proton and neutron form an isospin doublet with total isospin $I=1/2$ and third component of isospin $I_3 = \pm 1/2$. The charge independence of the strong nuclear force is then expressed in terms of invariance under unitary transformations in this isospin space. One such transformation would correspond to replacing all protons with neutrons and vice versa. Physically, isospin has nothing to do with spin apart from the fact that both satisfy the same $SU(2)$ algebra.

The idea of combining the quarks to isospin doublets that are used to describe QCD interactions is extended also in the weak interactions. This combination of quarks into doublets is also required by the fact that the generators of the SU(2) gauge transformation are the 2×2 Pauli spin-matrices. Hence, the wavefunction $\phi(x)$ must be written in terms of two components. Since the weak charged-current interaction associated with the W^\pm couples together different fermions, these doublets must contain flavours differing by one unit of electric charge. For example a possible weak doublet could be a vector, which the first component is the electron spinor and the second is the electron neutrino ν_e . The whole doublet is with weak isospin $I_W = 1/2$. The upper member of the doublet is with $I_W^{(3)} = +1/2$ while the lower member is with $I_W^{(3)} = -1/2$ and is always the particle state which differs by -1 unit in electric charge relative to the upper member of the doublet.

However, the observed form of the weak charged-current interaction couples only to left-handed chiral particle states and right-handed chiral antiparticle states, the gauge transformation can affect only LH particles and RH antiparticles. To achieve this, RH particle and LH antiparticle chiral states are placed in weak isospin singlets with $I_W=0$ and are therefore unaffected by the SU(2) local gauge transformation. The weak isospin doublets are composed of only LH chiral particle states and RH chiral antiparticle states and, for this reason, the symmetry group of the weak interaction is referred to as SU(2)_L. The weak isospin doublets are constructed from the weak eigenstates and therefore account for the mixing in the CKM. For example, the u quark appears in a doublet with the weak eigenstate d'. The complete set of weak doublets for the particles are

$$\begin{pmatrix} \nu_e \\ e_- \end{pmatrix}_L, \begin{pmatrix} \nu_\mu \\ \mu_- \end{pmatrix}_L, \begin{pmatrix} \nu_\tau \\ \tau_- \end{pmatrix}_L, \begin{pmatrix} u \\ d' \end{pmatrix}_L, \begin{pmatrix} c \\ s' \end{pmatrix}_L, \begin{pmatrix} t \\ b \end{pmatrix}_L, \quad (3.14)$$

while the RH particle chiral states are placed in weak isospin singlets with $I_W=I_W^{(3)}=0$,

$$e_R^-, \quad \mu_R^-, \quad \tau_R^-, \quad u_R, \quad d_R, \quad c_R, \quad s_R, \quad t_R, \quad b_R \quad (3.15)$$

3.2.2 Weak Interactions as Yang-Mills Theory

In the previous section the electromagnetic interaction was introduced by requiring the Dirac equation to be invariant under a U(1) local phase transformation. It was proved that the Lagrangian of the free particles is not invariant under this U(1) local phase transformation. However, the required gauge invariance could be restored by replacing the derivative ∂_μ with the covariant derivative capital D μ

$$\partial_\mu \rightarrow D_\mu = \partial_\mu + iqA_\mu, \quad (3.16)$$

where A_μ is a new field, Which has to transform under (3.2), so that the lagrangian is invariant.

The weak interaction and QCD are obtained by extending the local gauge principle to require that the Lagrangian is invariant under SU(2) and SU(3) local phase transformations ([37],[23],[31]). These transformations U are special (S), which means that the determinant of

the transformation is +1, and unitary (U), which means that these transformations preserve the inner product of two vectors expressed as $U^\dagger = U^{-1}$, while the number in the () stands for the dimension of the transformation or equivalently for the $n \times n$ representation of the transformations as matrices.

The prescription for achieving the required gauge invariance is to replace again the four-derivative ∂_μ with the covariant derivative D_μ but now defined in terms of the generators of the group. For example, for the SU(2) symmetry of the weak interaction

$$\partial_\mu \rightarrow D_\mu = \partial_\mu + ig_W \vec{T} \cdot \vec{W}_\mu(x), \quad (3.17)$$

where the $\vec{T} = (T_1, T_2, T_3) = \frac{1}{2}\vec{\sigma}$ are the three generators of SU(2) and $\vec{W}(x)$ are the three new gauge fields. The generators of the SU(2) and SU(3) symmetry groups do not commute and the corresponding local gauge theories are termed non-Abelian. In a non-Abelian gauge theory, the transformation properties of the gauge fields are not independent and additional gauge boson self-interaction terms have to be added to the field-strength tensor for it to be gauge invariant.

The commutation relations that the three generators satisfy is

$$[T_i, T_j] = \frac{1}{4}[\sigma_i, \sigma_j] = \frac{1}{4}2i\varepsilon_{ijk}\sigma_k = i\varepsilon_{ijk}T_k, \quad (3.18)$$

where ε_{ijk} is the totally antisymmetric Levi-Civita tensor. This tensor is the structure constant of the group.

In order to define completely such a Theory we need to determine one more thing. This is the hyper-spinors, where each one of the two components is a Dirac spinor³

An infinitesimal SU(2) local gauge transformation can be written as

$$\phi(x) = \begin{pmatrix} \nu_e(x) \\ e_-(x) \end{pmatrix} \rightarrow \phi'(x) = (I + ig_W \vec{\alpha}(x) \cdot \vec{T})\phi(x) \quad (3.19)$$

and for the adjoint spinors $\bar{\phi} = \phi^\dagger \gamma^0$ as:

$$\bar{\phi}(x) \rightarrow \bar{\phi}'(x) = \bar{\phi}(x)(I - ig_W \vec{\alpha}(x) \cdot \vec{T}) \quad (3.20)$$

For simplicity let's consider the fermion mass to be zero. The Lagrangian giving the Dirac equations for both the first ψ_1 and the second component ψ_2 of the SU(2) doublet can be written as

$$\mathcal{L} = i\bar{\phi}\gamma_\mu\partial^\mu\phi = i\bar{\psi}_1\gamma_\mu\partial^\mu\psi_1 + i\bar{\psi}_2\gamma_\mu\partial^\mu\psi_2. \quad (3.21)$$

The gauge invariance of the Lagrangian can be ensured by replacing the derivatives ∂_μ with the corresponding covariant derivatives, defined by (3.17), where $\vec{W}^\mu = (W_1^\mu, W_2^\mu, W_3^\mu)$ are the three gauge fields of the SU(2) symmetry. Therefore, the Lagrangian 3.20 becomes

³For the QCD and the SU(3) the hyper-spinors are defined as with three Dirac components respectively.

$$\mathcal{L} = i\bar{\phi}\gamma_\mu\partial^\mu\phi = i\bar{\phi}\gamma_\mu(\partial^\mu + ig_W\vec{T} \cdot \vec{W}^\mu)\phi \quad (3.22)$$

This Lagrangian includes the interactions between the fermions and W fields, but is only gauge invariant if the W fields have the correct transformation properties. Demanding

$$D^\mu\phi' = (I + ig_W\vec{\alpha}(x) \cdot \vec{T})D^\mu\phi. \quad (3.23)$$

and replacing (3.17) and keeping in mind the commutation equations of (3.18), one can see that the transformations of the three W fields are no longer independent and are given by the compact form

$$\vec{W}^\mu \rightarrow W'^\mu = W^\mu - \partial^\mu\vec{\alpha} - g_W\vec{\alpha} \times \vec{W}^\mu, \quad (3.24)$$

where the time-space dependence of the W fields and the phase α has been omitted. The cross product is coming as a result from the existence of the structure constant in the commutation relations (3.18).

Comparing (3.22) with (3.8), the kinetic term for the W fields are missing and have to be included, but of course this term must also be gauge invariant under a SU(2) local transformation. $F^{\mu\nu}$ tensor for the case of QED must be replaced by

$$\vec{W}^{\mu\nu} = \partial^\mu\vec{W}^\nu - \partial^\nu\vec{W}^\mu - g_W\vec{W}^\mu \times \vec{W}^\nu. \quad (3.25)$$

Therefore, in agreement with the term of the A_μ field, the terms of the three W^μ fields is equal to $-\frac{1}{4}W^{\mu\nu}W_{\mu\nu}$

Finally, let's focus for a while in the $-\frac{1}{4}\vec{W}^{\mu\nu} \cdot \vec{W}_{\mu\nu}$ term. This term is equal to

$$\begin{aligned} -\frac{1}{4}\vec{W}^{\mu\nu} \cdot \vec{W}_{\mu\nu} &= -\frac{1}{4}(\partial^\mu\vec{W}^\nu - \partial^\nu\vec{W}^\mu - g_W\vec{W}^\mu \times \vec{W}^\nu) \cdot (\partial_\mu\vec{W}_\nu - \partial_\nu\vec{W}_\mu - g_W\vec{W}_\mu \times \vec{W}_\nu) = \\ &= -\frac{1}{4}[(\partial^\mu W_i^\nu - \partial^\nu W_i^\mu) - g_W(W^\mu \times W^\nu)_i][(\partial_\mu W_{i\nu} - \partial_\nu W_{i\mu}) - g_W(\vec{W}_\mu \times \vec{W}_\nu)_i] = \\ &= -\frac{1}{4}(\partial^\mu W_i^\nu - \partial^\nu W_i^\mu)(\partial_\mu W_{\nu i} - \partial_\nu W_{\mu i}) + \frac{1}{2}g_W(\partial^\mu W_i^\nu - \partial^\nu W_i^\mu)(\vec{W}_\mu \times \vec{W}_\nu)_i \\ &\quad - \frac{1}{4}g_W^2(\vec{W}^\mu \times \vec{W}^\nu)_i(\vec{W}_\mu \times \vec{W}_\nu)_i \Rightarrow \\ -\frac{1}{4}\vec{W}^{\mu\nu} \cdot \vec{W}_{\mu\nu} &= -\frac{1}{4}(\partial^\mu W_i^\nu - \partial^\nu W_i^\mu)(\partial_\mu W_{\nu i} - \partial_\nu W_{\mu i}) + \frac{1}{2}g_W\varepsilon_{ijk}(\partial^\mu W_i^\nu - \partial^\nu W_i^\mu)\vec{W}_{\mu j}\vec{W}_{\nu k} \\ &\quad - \frac{1}{4}g_W^2\varepsilon_{ijk}\varepsilon_{ilm}W_j^\mu W_k^\nu W_{\mu l}W_{\nu m} \end{aligned}$$

The term with $+\frac{1}{2}$ is the triple gauge boson vertices and the term with the two Levi-Civita tensors is the quartic gauge boson vertices, as shown in Figure (25). These self-interactions are a consequence of non-commuting generators of the SU(2) group, and the associated fields are referred to as Yang–Mills fields. In terms of the physical fields obtained from electroweak unification of the Standard Model, there are two triple gauge boson vertices, $\gamma W^+ W^-$ and $Z W^+ W^-$, and three quartic gauge boson vertices $W^+ W^- W^+ W^-$, $W^+ W^- Z Z$ and $W^+ W^- \gamma \gamma$.

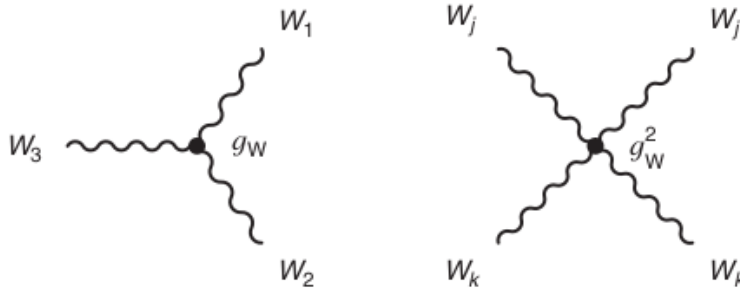


Figure 25: The triple and quartic gauge boson vertices arising from the SU(2) local gauge invariance.

3.2.3 The Cabibbo-Kobayashi-Maskawa Matrix, the W propagator and the Flavour Changing Neutral Currents

From the observed decay rates, the strength of the coupling at quarks is different among different quarks and with that of the lepton coupling. These observations were originally explained by the Cabibbo hypothesis. In the Cabibbo hypothesis, the weak interactions of quarks have the same strength as the leptons, but the weak eigenstates that are used to describe the interaction of quarks differ from the mass eigenstates ([37],[23],[31]). The weak eigenstates, are labelled with a ' (e.g. d') and are related to the mass eigenstates by the unitary matrix Cabibbo-Kobayashi-Maskawa (CKM) matrix

$$\begin{pmatrix} d' \\ s' \\ b' \end{pmatrix} = \begin{pmatrix} V_{ud} & V_{us} & V_{ub} \\ V_{cd} & V_{cs} & V_{cb} \\ V_{td} & V_{ts} & V_{tb} \end{pmatrix} \begin{pmatrix} d \\ s \\ b \end{pmatrix} \quad (3.26)$$

The d, s, b (as u, c and t) are spinors which satisfy the Dirac equation. The values of the CKM elements are measured using branching ratios where the specific transitions are observed. The CKM elements are measured as

$$\begin{pmatrix} |V_{ud}| & |V_{us}| & |V_{ub}| \\ |V_{cd}| & |V_{cs}| & |V_{cb}| \\ |V_{td}| & |V_{ts}| & |V_{tb}| \end{pmatrix} = \begin{pmatrix} 0.974 & 0.225 & 0.004 \\ 0.225 & 0.973 & 0.041 \\ 0.009 & 0.040 & 0.999 \end{pmatrix}$$

Because of the near diagonal nature of the CKM matrix, it is convenient to express it as an expansion in the relatively small parameter $\lambda = \sin \theta_c = 0.225$. In the widely used

Wolfenstein parameterisation, the CKM matrix is written in terms of four real parameters, λ, A, ρ, η . To \mathcal{O}^4 the CKM matrix can be parameterised as

$$\begin{pmatrix} V_{ud} & V_{us} & V_{ub} \\ V_{cd} & V_{cs} & V_{cb} \\ V_{td} & V_{ts} & V_{tb} \end{pmatrix} = \begin{pmatrix} 1 - \lambda^2/2 & \lambda & A\lambda^3(\rho - i\eta) \\ -\lambda & 1 - \lambda^2/2 & A\lambda^2 \\ A\lambda^3(1 - \rho - i\eta) & -A\lambda^2 & 1 \end{pmatrix}$$

Consequently, the weak charged-current vertices involving quarks are given by using the weak eigenstates and not the mass eigenstates.

From the observation of parity violation, which was initially discovered in 1957 by Wu and collaborators, the weak interaction vertices are required have a different form from those of QED and QCD. The general bilinear combination of two spinors can be written as $\bar{u}(p')\Gamma u(p)$, where Γ is a 4×4 matrix formed from products of the Dirac γ -matrices. However in order the bilinear combination to respect the Lorentz invariance, there are only 5 possible Γ matrices that correspond to scalar, pseudoscalar, vector, axial vector and tensor currents.

The most general Lorentz-invariant form for the interaction between a fermion and a boson is a linear combination of the bilinear covariants. If this is restricted to the exchange of a spin-1 (vector) boson, the most general form for the interaction is a linear combination of vector and axial vector currents,

$$j^\mu \sim \bar{u}(p')(g_V\gamma^\mu + g_A\gamma^\mu\gamma^5)u(p) = g_V j_V^\mu + g_A j_A^\mu, \quad (3.27)$$

where g_V and g_A are vector and axial vector coupling constants and the current has been decomposed into vector and axial vector components

$$j_V^\mu = \bar{u}(p')g_V u(p)\gamma^\mu \quad j_A^\mu = \bar{u}(p')\gamma^\mu\gamma^5 u(p) \quad (3.28)$$

Furthermore, the observed maximal parity violation occurs when $|g_V|=|g_A|$, corresponding to a pure V - A or V + A interaction. From experiments, it is known that the weak charged current due to the exchange of W^\pm bosons is a vector minus axial vector (V-A) interaction of the form $\gamma^\mu(1 - \gamma^5)$. For the weak interaction, the V-A vertex factor of already includes the left-handed chiral projection operator. This property of the weak current forces only left-handed chiral states for particle spinors involving non-zero contributions, since the product of the left-handed chiral projection operator and the right-handed chiral projection is zero. Hence, only left-handed chiral particle states participate in the charged- current weak interaction. As for antiparticle spinors v the $P_L = \frac{1}{2}(1 - \gamma^5)$ projects out right-handed chiral states, $v_R = P_L v$ and therefore only the right-handed chiral antiparticle states participate in the charged- current weak interaction. In the ultra relativistic limit the chiral and helicity states are the same, and therefore the V-A term in the weak interaction vertex projects out left-handed helicity particle states and right-handed helicity antiparticles states.

The weak interaction not only differs from QED and QCD in the form of the interaction vertex, but it is mediated by the massive W and bosons, with mass $m_W = 80.4$ GeV and $m_Z = 91.2$ GeV and therefore, the Feynman rule associated with the exchange of a virtual W boson is given by

$$\begin{array}{c}
\text{W/Z} \\
\text{---} \\
\frac{-i(g_{\mu\nu} - q_\mu q_\nu / m^2)}{q^2 - m^2}
\end{array}$$

Figure 26: The Feynman propagators for Weak interactions. q^2 is again the propagated momentum.

As mentioned in 3.2.1 the quark spinors that are involved in the charged currents are not the mass eigenstates but the weak eigenstates given by (3.26). In correspondences with the electromagnetic current the weak Flavour Changing Charged Currents involving quarks are given by

$$j_+^\mu = -i \frac{g_W}{\sqrt{2}} (\bar{u}, \bar{c}, \bar{t}) \gamma^\mu \frac{1}{2} (1 - \gamma^5) \begin{pmatrix} V_{ud} & V_{us} & V_{ub} \\ V_{cd} & V_{cs} & V_{cb} \\ V_{td} & V_{ts} & V_{tb} \end{pmatrix} \begin{pmatrix} d \\ s \\ b \end{pmatrix}, \quad (3.29)$$

$$j_-^\mu = -i \frac{g_W}{\sqrt{2}} (\bar{d}, \bar{s}, \bar{b}) \begin{pmatrix} V_{ud}^* & V_{cd}^* & V_{td}^* \\ V_{us}^* & V_{cs}^* & V_{ts}^* \\ V_{ub}^* & V_{cb}^* & V_{tb}^* \end{pmatrix} \gamma^\mu \frac{1}{2} (1 - \gamma^5) \begin{pmatrix} u \\ c \\ t \end{pmatrix}, \quad (3.30)$$

where g_W is the constant coupling for the W boson. For example, for the transition $u \rightarrow d$ the FCCC is given by

$$j_{ud}^\mu = -i \frac{g_W}{\sqrt{2}} \bar{u} \gamma^\mu \frac{1}{2} (1 - \gamma^5) V_{ud} d$$

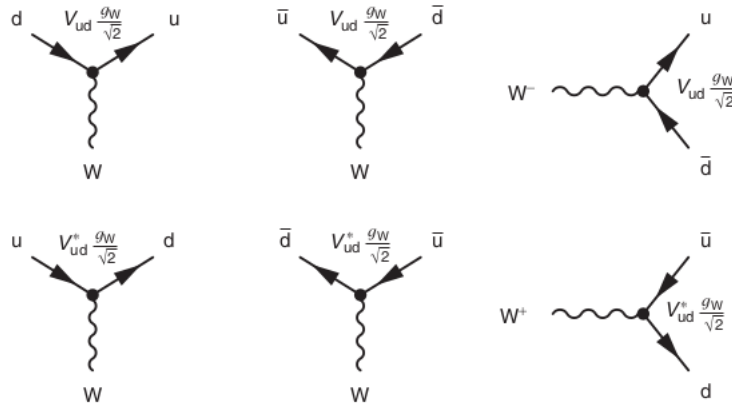


Figure 27: The charged current vertices for transitions $u \leftrightarrow d$.

Furthermore, the leptonic charged current are given by

$$j_+^\mu = \frac{g_W}{\sqrt{2}} \bar{\nu}_\ell \gamma^\mu \frac{1}{2} (1 - \gamma^5) \ell, \quad (3.31)$$

$$j_-^\mu = \frac{g_W}{\sqrt{2}} \bar{\ell} \gamma^\mu \frac{1}{2} (1 - \gamma^5) \nu_\ell, \quad (3.32)$$

where ℓ and ν_ℓ are the leptonic Dirac spinors for the charged leptons and their associated neutrinos respectively.

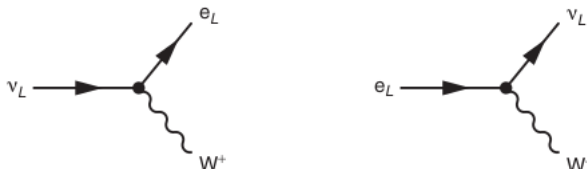


Figure 28: The charged current vertices for transitions $e^- \leftrightarrow \nu_e$

3.2.4 The Z propagator and weak Neutral Currents

The Weak Neutral currents were first discovered at CERN in 1973 by observing $\bar{n}u_\mu + e^- \rightarrow \bar{n}u_\mu + e^-$ in the bubble chamber of Gargamelle. However, these neutral currents had already been proposed in a series of separate works in the 1960s by Glashow, Weinberg and Salam, who were trying to come up with a theory that would unify electromagnetic and weak interactions between elementary particles. The total cross section that was measured back in 1973 was $\sim \frac{1}{3}$ compared with one from charged weak currents using, but this cross section was bigger than the charged weak current of higher order like the right diagram in Figure (29).

Therefore, this observation is the first experimental proof for the existence of the electroweak theory. In agreement with the FCCCs, the neutral currents have to be of the V-A form, which mean that the neutral current must include again the $\gamma^\mu(1 - \gamma^5)$ factor, but now the coefficients for the two currents may be different. The propagator is described again as the W propagator (Figure (26))

Indeed, there are four types of weak neutral currents that leave unaffected the leptonic and fermionic currents. The weak neutral current is given ([37],[23],[31]) by the form

$$- \frac{ig_Z}{2} \gamma^\mu (c_V^f - c_A^f \gamma^5), \quad (3.33)$$

where f is either the three neutrino types, the three charged leptons, the three u-like quarks or the three d-like quarks and g_Z is the weak coupling with the Z boson. The two coefficients are given by

$$c_V^f = I_W^{(3)} - 2Q^f \sin^2 \theta_W \quad c_A^f = I_W^{(3)} \quad (3.34)$$

In Table (1) the c_V^f and c_A^f factors for the weak neutral currents are presented.

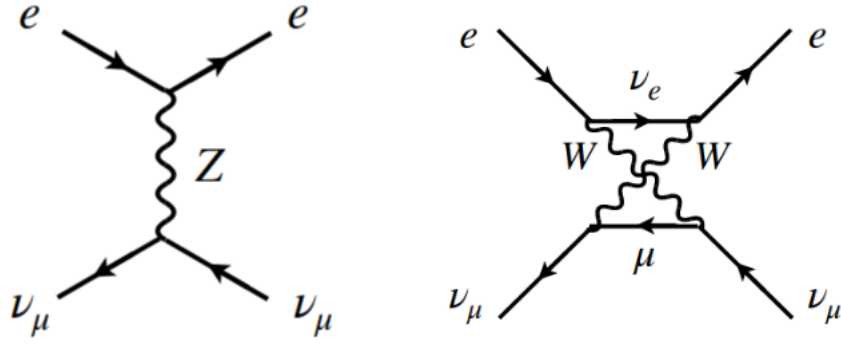


Figure 29: Left: An event in which the leptonic flavours are unaffected but the electron and neutrino changes momentum by exchange of the neutral Z^0 . Right: A higher order charged current for the same interaction. The total measured cross section is higher predicted by the higher order charged current on the right.

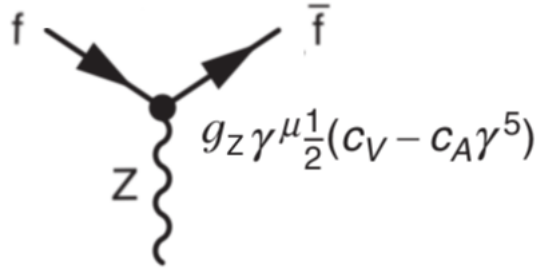


Figure 30: The weak Z vertex.

3.3 Electroweak Unification

Up to now, we have talked about four bosons of QED and the weak interaction, the neutral photon γ , the neutral Z and the charged W^\pm bosons, while we have used the A^μ and $W_1^\mu, W_2^\mu, W_3^\mu$. Consequently, it is plausible that the neutral bosons can be expressed in terms of quantum state formed from two neutral bosons, one of which is associated with the $SU(2)_L$ local gauge symmetry and the other one with the $U(1)$ local symmetry, while the other two charged boson are associated with the remaining two W^μ fields.

In the electroweak model of Glashow, Salam and Weinberg (GSW) ([37],[23],[31]) the $U(1)$ gauge symmetry of electromagnetism is replaced with a new $U(1)_Y$ local gauge symmetry

$$\Psi(x) \rightarrow \Psi'(x) = \hat{U}(x)\Psi(x) = e^{ig' \frac{Y}{2} \zeta(x)} \Psi(x). \quad (3.35)$$

In complete agreement with 3.1 section, the electric charge has been replaced by the $g' \frac{Y}{2}$ factor, where Y is the hypercharge, and the now the interaction term of Dirac spinor and the A^μ field has been replaced by the $g' \frac{Y}{2} \gamma^\mu B_\mu \psi$ term, where now a new B_μ field has been used. I

Table 1: The c_V and c_A coefficients for the weak neutral currents. The $\theta_W = 28.75^\circ$ is the Weinberg weak-mixing angle with $\sin^2 \theta_W = 0.2314$.

f	c_V	c_A
ν_e, ν_μ, ν_τ	$\frac{1}{2}$	$\frac{1}{2}$
e^-, μ^-, τ^-	$-\frac{1}{2} + 2 \sin^2 \theta_W$	$-\frac{1}{2}$
u, c, t	$+\frac{1}{2} - \frac{4}{3} \sin^2 \theta_W$	$\frac{1}{2}$
d, s, b	$-\frac{1}{2} + \frac{2}{3} \sin^2 \theta_W$	$-\frac{1}{2}$

As mentioned above, all the right-handed components of charged particles form weak isospin singlets with $I_W = I_W^3 = 0$. For all the components, charged and neutrals, left or right-handed, the electric charge and the I_W^3 projection of the isospin is combined with the hypercharge Y with the equation

$$Q = I_W^3 + \frac{Y}{2}. \quad (3.36)$$

Table 2: The charge, the third projection of the isospin and the hypercharge for the left and right-handed chiral components.

f	Q_f	$I_W^{(3)}$	Y_L	Y_R
ν_e, ν_μ, ν_τ	0	$+\frac{1}{2}$	-1	0
e^-, μ^-, τ^-	-1	$-\frac{1}{2}$	-1	-2
u, c, t	$+\frac{2}{3}$	$+\frac{1}{2}$	$+\frac{1}{3}$	$+\frac{4}{3}$
d, s, b	$-\frac{1}{3}$	$-\frac{1}{2}$	$+\frac{1}{3}$	$\frac{2}{3}$

For simplicity let's work only with the first lepton generation. Following exactly the same steps the whole procedure can be reproduced for the other two generations. The Lagrangian for the $U_Y \times SU(2)_L$ theory for the electronic doublet L_e , is given by

$$\mathcal{L}_0 = \bar{L}_e \gamma^\mu \left(i\partial_\mu - g_W T_\alpha W_\mu^\alpha - g' \frac{Y_L}{2} B_\mu \right) L_e + \bar{e}_R \gamma^\mu \left(i\partial_\mu - g' \frac{Y_R}{2} B_\mu \right) e_R - \frac{1}{4} W_{\mu\nu}^\alpha W_\alpha^{\mu\nu} - \frac{1}{4} B_{\mu\nu} B^{\mu\nu}, \quad (3.37)$$

where g_W is the coupling constant for the weak current and g' is the coupling constant for the electromagnetic current. B_μ the photonic field, $B_{\mu\nu}$ the tensor for the $U(1)_Y$ symmetry, $\vec{T} = (T_1, T_2, T_3)$ and $\vec{W} = (W_1, W_2, W_3)$ the three generators and three gauge fields of $SU(2)_I$, and $W_{\mu\nu}^\alpha$ the tensor of $SU(2)_I$.

The Lagrangian (3.37) is invariant under the transformations of (3.35) and (3.19), which means that it describes the unified electroweak theory of $U(1)_Y \times SU(2)_I$, and hence the partial derivative has been replaced properly by the covariant derivative for the left-handed and right-handed components of spinors. We can see that the right-handed components are involved only in the derivative with the $U(1)_Y$ covariant derivative, while the left-handed

components are involved both with the $SU(2)_I$ and the $U(1)_Y$ covariant derivative. This mixing is in agreement with the fact that virtual photons couples with both the left and right-handed components while the weak currents couples only with the left-handed components of the spinors.

However, despite the fact that this theory is renormalizable and is in agreement with the experimental observations, this Lagrangian assumes that there is not a intrinsic reason so that the gauge bosons have different masses, as the fermions too. So there is one fundamental reason that this $U(1)_Y \times SU(2)_I$ underlying symmetry must be violated. In the Standard Model this violation can be expressed by the existence of two scalar fields, which will couple naturally with different strength to the gauge bosons and the fermions.

3.3.1 The Higgs Mechanism and the Spontaneous Symmetry Breaking

To break the underlying symmetry of (3.37) under the transformations of (3.35) and (3.19), we need to add terms for the two scalar field in the (3.37) Lagrangian. Because the Higgs mechanism ([37],[23],[31]) is required to generate the masses of the electroweak gauge bosons, one of the scalar fields must be neutral, written as ϕ^0 , and the other must be charged such that ϕ^+ and $(\phi^+)^* = \phi^-$ give the longitudinal degrees of freedom of the W^+ and W^- . The two complex scalar fields are placed in a weak isospin doublet

$$\phi = \begin{pmatrix} \phi^+ \\ \phi^0 \end{pmatrix} = \frac{1}{\sqrt{2}} \begin{pmatrix} \phi_1 + i\phi_2 \\ \phi_3 + i\phi_4 \end{pmatrix} \quad (3.38)$$

As usual, the upper and lower components of the doublet differ by one unit of charge. The Lagrangian for this doublet of complex scalar fields is

$$\mathcal{L} = \frac{1}{2}(\partial_\mu \phi)^\dagger (\partial^\mu \phi) - \mu^2 \phi^\dagger \phi - \lambda(\phi^\dagger \phi)^2 \quad (3.39)$$

For $\mu^2 < 0$, the potential has an infinite set of degenerate minima satisfying

$$\phi^\dagger \phi = \frac{1}{2}(\phi_1^2 + \phi_2^2 + \phi_3^2 + \phi_4^2) = \frac{v^2}{2} = -\frac{\mu^2}{2\lambda} \quad (3.40)$$

while for the case $\mu^2 > 0$, the potential has only one minimum which is $\phi_1 = \phi_2 = \phi_3 = \phi_4 = 0$

After symmetry breaking, the neutral photon is required to remain massless, and therefore the minimum of the potential must correspond to a non-zero vacuum expectation value only of the neutral scalar field ϕ^0 , which is express as $\langle 0|\phi|0\rangle = \frac{1}{\sqrt{2}} \begin{pmatrix} 0 \\ v \end{pmatrix}$

The fields then can be expanded about this minimum by writing

$$\Phi = \sqrt{\frac{1}{2}} \begin{pmatrix} \phi_1 + i\phi_2 \\ v + \eta(x) + i\phi_4 \end{pmatrix} \quad (3.41)$$

Let's focus now in the (3.39) Lagrangian. This Lagrangian is not invariant under the $U(1)_Y \times SU(2)_I$ local gauge symmetry of the electroweak model. Hence, we will replace the partial derivative with the appropriate covariant derivatives

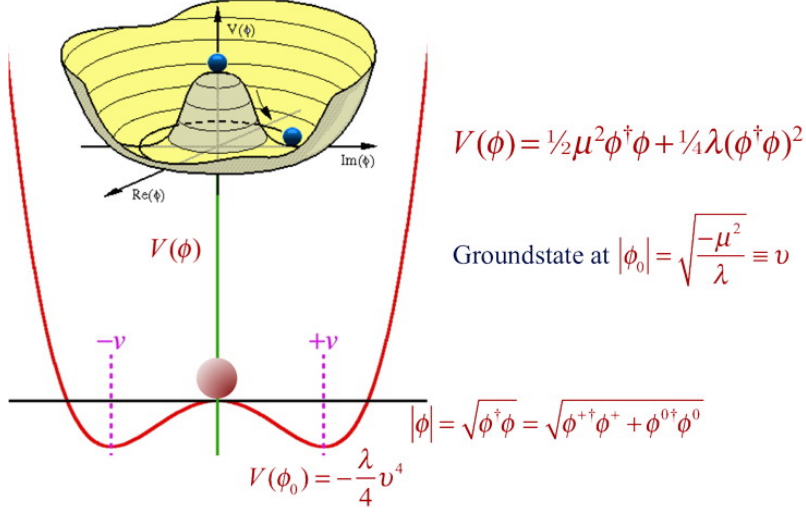


Figure 31: The Higgs potential for the case of one complex scalar field with $\mu^2 < 0$. As we can see the minima which is given by $\phi^\dagger\phi = \frac{1}{2}(\phi_1^2 + \phi_2^2) = v^2 = -\frac{\mu^2}{\lambda}$ form a circle in the bottom.

$$\partial_\mu \rightarrow D_\mu = \partial_\mu + ig_W \vec{T} \cdot \vec{W}_\mu + ig' \frac{Y}{2} B_\mu \quad (3.42)$$

Since the lower component of the Higgs doublet is neutral and has $I_W^{(3)} = -\frac{1}{2}$ and thus the Higgs doublet, according to (3.36) has hypercharge $Y=1$. If we absorb properly the three Goldstone fields, the Higgs doublet will be rewritten in the form

$$\phi = \begin{pmatrix} 0 \\ v + h \end{pmatrix} \quad (3.43)$$

and hence by calculating the $(D_\mu\phi)^\dagger(D^\mu\phi)$ term, the mass terms for the gauge fields will be given by terms that are quadratic in the gauge boson fields (e.g. $W_\mu^{(1)}W^{\mu(1)}$). But to give a meaning to these fields we will define the four natural fields

$$W_\mu^\pm = \frac{1}{2}(W_\mu^1 \mp W_\mu^2), \quad (3.44)$$

$$A_\mu = +B_\mu \cos\theta_W + W_\mu^{(3)} \sin\theta_W, \quad (3.45)$$

$$Z_\mu = -B_\mu \sin\theta_W + W_\mu^{(3)} \cos\theta_W, \quad (3.46)$$

where $\cos\theta_W = \frac{g_W}{\sqrt{g_W^2 + g'^2}}$ and $\sin\theta_W = \frac{g'}{\sqrt{g_W^2 + g'^2}}$

Therefore the masses of the four natural fields are equal to

$$m_{W^+} = m_{W^-} = m_W = \frac{1}{2}g_W v \quad (3.47)$$

$$m_A = 0 \quad (3.48)$$

$$m_Z = \frac{1}{2}v\sqrt{g_W^2 + g'^2} \quad (3.49)$$

and we can now conclude that the masses of the massive weak particles are satisfying the equation

$$\frac{m_W}{m_Z} = \cos \theta_W, \quad (3.50)$$

where θ_W is the weak mixing angle satisfying $\sin^2 \theta_W = 0.2315$. Similar with the four bosons, we can use the potential terms to calculate the Higg's field mass which is equal to

$$m_H^2 = 2\lambda v^2. \quad (3.51)$$

As mentioned above the left and right-handed chiral components of the Dirac spinors transform in a different way under the $SU(2)_I$ and $U(1)_Y$ gauge transformations. Hence, $-m\bar{\Psi}\Psi$ terms must be omitted from the Dirac Lagrangian since such terms include products of right-handed and left handed chiral components. However, in order to retrieve the fermion masses, we need to add to the (3.37) Lagrangian terms where the left and right components are coupled, but in way that the whole term is invariant under the $U(1)_Y \times SU(2)_I$ gauge transformations. This invariance is ensured by adding term where the left-handed chiral states are coupled with the Higgs isodoublet and with the right-handed chiral states. Hence, the terms that will be added are

$$\mathcal{L}_e = -g_e \left[(\bar{\nu}_e \quad \bar{e})_L \begin{pmatrix} \phi^+ \\ \phi^0 \end{pmatrix} e_R + \bar{e}_R (\phi^{\dagger*} \quad \phi^{0*}) \begin{pmatrix} \nu_e \\ e \end{pmatrix}_L \right] \quad (3.52)$$

where g_e is a constant known as the Yukawa coupling of the electron to the Higgs field. If someone use again the Higgs doublet after the spontaneously symmetry breaking (3.43) the retrieved electron mass will be equal to

$$m_e = g_e \frac{v}{\sqrt{2}} \quad (3.53)$$

To retrieve the mass of the other two lepton someone should use a different Higgs coupling constants, e.g. g_μ and g_τ instead of g_e . In similar way, someone could generate the masses of the quarks. However the non-zero vacuum expectation value occurs in the lower (neutral) component of the Higgs doublet, and hence the Higgs mechanism can be used to generate masses only for the charged leptons and the down-type quark, d,s and b, and therefore one more interaction term is required. This is achieved by using the charged conjugated Higgs isodoublet,

$$\mathcal{L}_u = -g_u \left[(\bar{u} \quad \bar{d})_L \begin{pmatrix} -\phi^{0*} \\ \phi^- \end{pmatrix} u_R + h.c. \right], \quad (3.54)$$

which after the symmetry breaking will retrieve the up-type quark masses as

$$m_u = g_u \frac{v}{\sqrt{2}} \quad (3.55)$$

To conclude for all the fermions, their mass, the Higgs coupling constant (which is also called Yukawa coupling) and the vacuum expectation value of the Higgs field v are combined in the formula

$$g_f = \sqrt{2} \frac{m_f}{v} \quad (3.56)$$

where the vacuum expectation value of the Higgs field is $v=246$ GeV.

3.4 Lepton Flavour Universality

In the Standard Model of particle physics the three charged leptons are identical copies of each other. The only property that can separate the charged leptons are their mass, which is different due to the Yukawa coupling which are their couplings with the Higgs Field. Even for the electroweak coupling of the gauge bosons to leptons is independent of the lepton flavour. This characteristic is called Lepton Flavour Universality (LFU) ([37],[23],[31],[31]). In tree level decays, any violation of LFU would be a clear sign of physics beyond the Standard Model. Rare b decays are highly sensitive to New Physics particles which preferentially couple to the 2nd and 3rd generations of leptons. Indeed, if someone consider the experimental decay rates and the slightly different phase space would consider that the couplings with the W boson for the charged leptons G_e, G_μ, G_τ are

$$\frac{G_e}{G_\mu} = 1.000 \pm 0.004 \quad (3.57)$$

and

$$\frac{G_\tau}{G_\mu} = 1.0021 \pm 0.0033 \quad (3.58)$$

so that within the SM and withing the experimental uncertainties the measurements are in agreement with SM lepton Flavour Universality, which is expressed as

$$G_e = G_\mu = G_\tau = 1 \quad (3.59)$$

The identical W^\pm and Z couplings to all three lepton flavours can be expressed as the independence of the branching fractions of decays involving different lepton families of the lepton flavours. This branching fractions could only differ due to the differences of the phase space (since the leptons have different mass) and due to helicity-suppressed contributions. Therefore, any experimental evidence [6] of Lepton Flavour Non-Universality using semileptonic or rare decays would be a clear sign of physics beyond the SM (BSM), BSM theories involving leptoquarks or Z' particles.

A very clean test for New Physics (NP) can be performed by taking ratios of $b \rightarrow s\ell\ell$ decays to different lepton species. These decays are not allowed at tree level, since they are Flavour Changing Neutral Currents, and due to their low value matrix element are highly sensitive to NP effects.

3.5 $R_K(\mu)$

As discussed in Paragraph (3.4), the decay⁴ $B^+ \rightarrow K^+\ell^+\ell^-$, where ℓ stands for either a muon or an electron, is a flavor-changing neutral current process and are highly suppressed in the standard model as they proceed through amplitudes involving electroweak loop (penguin and box) diagrams. These electroweak loops are making the branching fraction $B^+ \rightarrow K^+\ell^+\ell^-$ highly sensitive to the presence of new physics, like leptoquark models⁵ or models that contain the Z' boson⁶.

Owing to the equality of the electroweak couplings of electrons and muons in the SM, known as lepton universality, the branching fraction of $B^+ \rightarrow K^+\mu^+\mu^-$ to $B^+ \rightarrow K^+e^+e^-$ is expected to be unity within an uncertainty of $\mathcal{O}(10^{-3})$ in the SM (3.6).

The value of R_K [1],[21] within a given range of the dilepton mass squared from q_{min}^2 to q_{max}^2 is given by

$$R_K = \frac{\int_{q_{min}^2}^{q_{max}^2} \frac{d\Gamma[B^+ \rightarrow K^+\mu^+\mu^-]}{dq^2} dq^2}{\int_{q_{min}^2}^{q_{max}^2} \frac{d\Gamma[B^+ \rightarrow K^+e^+e^-]}{dq^2} dq^2}. \quad (3.60)$$

where Γ is the q^2 -dependent partial width of the decay. The value of R_K is determined using the ratio of the relative branching fractions of the decays $B^+ \rightarrow K^+\ell^+\ell^-$ and $B^+ \rightarrow J/\psi K^+, J/\psi \rightarrow \ell^+\ell^-$ with $\ell = e, \mu$ respectively. This transformed formula:

$$R_K = \left(\frac{\mathcal{B}(B^+ \rightarrow K^+\mu^+\mu^-)}{\mathcal{B}(B^+ \rightarrow K^+J/\psi(\mu^+\mu^-))} \right) / \left(\frac{\mathcal{B}(B^+ \rightarrow K^+e^+e^-)}{\mathcal{B}(B^+ \rightarrow K^+J/\psi(e^+e^-))} \right), \quad (3.61)$$

where \mathcal{B} is each time the branching ratio of the decay inside the two parentheses and $N(B^+)$ is the number of produced B^+ mesons.

This formula is much useful, since it uses the large branching fraction of the $B^+ \rightarrow K^+J/\psi$ to cancel potential sources of systematic uncertainties between electrons and muons. The first ratio (the one with the muons) is also known as $R_K(\mu)$ and the latter (the one with the electrons) is also known as $R_K(e)$. The purpose of this thesis is to measure the $R_K(\mu)$,

$$R_K(\mu) = \frac{\mathcal{B}(B^+ \rightarrow K^+\mu^+\mu^-)}{\mathcal{B}(B^+ \rightarrow K^+J/\psi(\mu^+\mu^-))} \quad (3.62)$$

However, in all particles physics experiments, branching ratios are not measured directly, since a part of the total particles are within the detector's acceptance and are efficiently reconstructed. The number of the B-candidates for the two decays that will be reconstructed in the data is equal to:

$$N(B^+ \rightarrow K^+\mu^+\mu^-)_{data} = N(B^+) \times \mathcal{B}(B^+ \rightarrow K^+\mu^+\mu^-) \times (\alpha \times \varepsilon)_{B^+ \rightarrow K^+\mu^+\mu^-} \quad (3.63)$$

⁴For the rest of this thesis, the charge conjugate process will be implied for all processes with the same notation for each decay.

⁵Leptoquarks are hypothetical particles that would interact with quarks and leptons carrying both lepton and baryon numbers at the same time and would allow common vertices for leptons and quarks in the Feynman diagrams.

⁶ Z' (and W') bosons refer to hypothetical gauge bosons that arise from extensions of the electroweak symmetry of the Standard Model.

$$N(B^+ \rightarrow K^+ J/\psi(\mu^+ \mu^-))_{data} = N(B^+) \times \mathcal{B}(B^+ \rightarrow K^+ J/\psi(\mu^+ \mu^-)) \times (\alpha \times \varepsilon)_{B^+ \rightarrow K^+ J/\psi(\mu^+ \mu^-)} \quad (3.64)$$

where $\alpha \times \varepsilon$ is the total acceptance \times efficiency factor for each decay. Keeping in mind that B^\pm notation stands for both B^+ and B^- mesons, $N(B^+)$ is the sum of produced B^+ and B^- mesons. The probability of forming a B^- (B^+) meson from a b (\bar{b}) quark is equal to $f_u=0.375 \pm 0.023$ [2]. Hence the total number of B^+ is equal to

$$N(B^+) = N(B^+) + N(B^-) = N(b\bar{b}) \times f_u + N(b\bar{b}) \times f_u = 2 \times N(b\bar{b}) \times f_u, \quad (3.65)$$

where $N(b\bar{b})$ is the number of produced $b\bar{b}$ produced pairs. The production process for the B^+ (B^-) meson is independent of its decay mode and indeed $N(B^+)$ is cancelled out.

Combing the equations (3.63) and (3.64) with (3.62), the $R_K(\mu)$ is expressed in terms of measured quantities as

$$R_K(\mu) = \frac{\frac{N(B^+ \rightarrow K^+ \mu^+ \mu^-)_{data}}{(\alpha \times \varepsilon)_{B^+ \rightarrow K^+ \mu^+ \mu^-}}}{\frac{N(B^+ \rightarrow K^+ J/\psi(\mu^+ \mu^-))_{data}}{(\alpha \times \varepsilon)_{B^+ \rightarrow K^+ J/\psi(\mu^+ \mu^-)}}} = \left(\frac{N(B^+ \rightarrow K^+ \mu^+ \mu^-)_{data}}{N(B^+ \rightarrow K^+ J/\psi(\mu^+ \mu^-))_{data}} \right) \times \left(\frac{(\alpha \times \varepsilon)_{B^+ \rightarrow K^+ J/\psi(\mu^+ \mu^-)}}{(\alpha \times \varepsilon)_{B^+ \rightarrow K^+ \mu^+ \mu^-}} \right) \quad (3.66)$$

The first ratio will be calculated from data and the second ratio will be calculated using Monte Carlo (MC) samples. Finally, this ratio will be measured using only for the tag side, which means that only reconstructed muons that fired at least one trigger will be used to reconstruct the B candidates.

For a cross check we will also measure the

$$R_{\psi(2S)}(\mu) = \frac{\mathcal{B}(B^+ \rightarrow K^+ \psi(2S)(\mu^+ \mu^-))}{\mathcal{B}(B^+ \rightarrow K^+ J/\psi(\mu^+ \mu^-))} \quad (3.67)$$

ratio, where instead of the rare B decay the $B^+ \rightarrow K^+ \psi(2S), \psi(2S) \rightarrow \mu^+ \mu^-$ will be used⁷.

3.6 $B^\pm \rightarrow K^\pm \ell^- \ell^+$

In the Standard Model, transitions like $b \rightarrow s$ or more general flavor-changing neutral currents (FCNCs) are forbidden, since there is no direct coupling between the b quark and the s or d quarks [3]. Effective FCNC are induced by one-loop, or ‘‘penguin’’ diagrams [28], where a quark emits and re-absorbs a W thus changing flavor twice, as it is shown in the following Feynman diagram:

These loop diagrams with their interesting combinations of CKM matrix elements give insight into the Standard Model. In addition, they are quite sensitive to new physics.

At the quark level, the decays $B \rightarrow K^{(*)} \mu^+ \mu^-$, where $(*)$ stands for either the charge of the B meson or the for the K-star meson in case of the neutral B meson, are proceed via $b \rightarrow s$ flavour changing neutral currents (FCNC) transitions. FCNC transitions are interactions that change the flavor of a fermion without altering its electric charge. Two kinds of Feynman diagram contributes to these transitions, a) the so-called electroweak penguin diagram and b) the W box diagram.

⁷Again, the contamination from the Cabibbo suppressed decay $B^+ \rightarrow \pi^+ \psi(2S)$ needs to be subtracted.

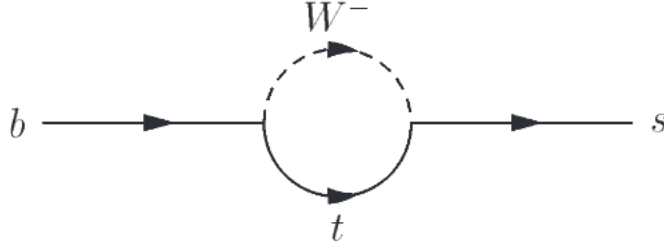


Figure 32: One loop Feynman Diagram for the $b \rightarrow s$ transition [28].

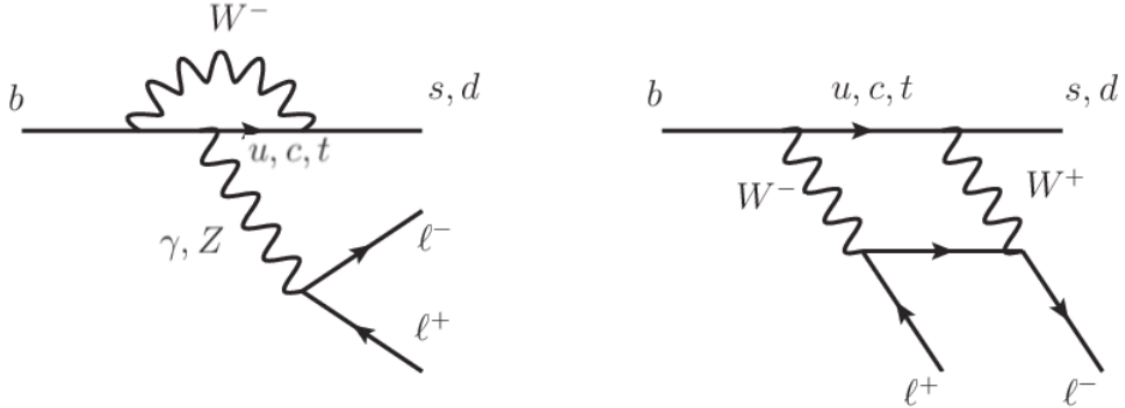


Figure 33: Left: the electroweak penguin diagram. Right: the W box diagram. [28]

In the penguin diagram an emitted virtual photon or a Z^0 produces a pair of leptons. The final quark can be either the s quark from the second generation or the d quark from the first generation.

At high energy scales, ~ 80 GeV, quark decays are governed by Feynman diagrams such as those depicted in Figure (33). To obtain an effective low energy theory relevant for scales close to the mass of b quark ~ 5 GeV, heavy degrees of freedom must be integrated out to obtain an effective coupling for point-like interactions of initial and final state particles. For semileptonic decays like the β -decays this integration corresponds to derivation of the Fermi theory of point-like four-fermion interactions from Electroweak Quantum Field Theory.

The heavy degrees of freedom in loop decays are W, Z^0 and t quarks. We should keep in mind that due to the CKM matrix the dominant virtual quark is the top quark. After the integration they don't appear explicitly in the theory, but their effects are hidden in the effective gauge coupling constants, running masses and in the so-called Wilson coefficients (C_i) describing the effective strength of the local operators (\mathcal{O}_i) generated by electroweak and strong interactions. There are 10 operators. These operators are grouped in three categories.

The first category is the current-current operator group and is formed by the first two operators ($i=1,2$). These operators are used for Flavor-Changing-Charged-Currents. The next four operators ($i=3,4,5,6$) are called gluonic penguin operators and are grouped in the

second category. In this category, a gluon either on-shell or off-shell can be emitted as a final state particle. The last four operators are grouped in the third category and are used in the electroweak penguin diagrams.

The effective Hamiltonian for $b \rightarrow s$ penguin decays has the following form:

$$\mathcal{H}_{eff} = -\frac{4G_F}{\sqrt{2}} V_{tb} V_{ts}^* \sum_{i=1}^{10} C_i(\mu) \mathcal{O}_i(\mu) \quad (3.68)$$

Technically, the calculations are performed at a high energy scale $\mu \sim M_W$, and then evolved to a low energy scale $\mu \sim m_b$ using renormalization group equations. This evolution mixes the operators:

$$C_i(\mu) = \sum_j U_{ij}(\mu, M_W) C_j(M_W) \quad (3.69)$$

The renormalization guarantees that the μ dependence of C_i is canceled by the μ dependence of \mathcal{O}_i , thus any observable quantity should not depend on the renormalization scale μ . However, since the calculations are performed perturbatively, the truncation of the perturbative series induces μ dependence of the theoretical predictions, which often dominates the theoretical uncertainty. Higher order terms must be included to minimize the μ dependence.

Even though renormalization mixes the operators, specific processes are mostly sensitive to a small subset of Wilson coefficients. For example the $b \rightarrow sl^+l^-$ is dominated by the C_7, C_9 and C_{10} , while C_8 enters at higher order in the strong coupling.

$$\mathcal{O}_7 = \frac{e}{(4\pi)^2} \bar{m}_b [\bar{s} \sigma^{\mu\nu} P_R b] F_{\mu\nu} \quad (3.70)$$

$$\mathcal{O}_8 = \frac{g_s}{(4\pi)^2} \bar{m}_b [\bar{s} \sigma^{\mu\nu} P_R T^a b] G_{\mu\nu}^a \quad (3.71)$$

$$\mathcal{O}_9 = \frac{e^2}{(4\pi)^2} [\bar{s} \gamma_\mu P_L b] [\bar{l} \gamma^\mu l] \quad (3.72)$$

$$\mathcal{O}_{10} = \frac{e^2}{(4\pi)^2} [\bar{s} \gamma_\mu P_L b] [\bar{l} \gamma^\mu \gamma_5 l] \quad (3.73)$$

where $P_{R/L} = (1 \pm \gamma_5)/2$ denote chiral projectors and $m_b(\mu)$ the $\bar{M}Sb$ -quark mass at the scale μ .

While Wilson coefficients represent short distance (i.e. high energy) electroweak and strong interactions, the operator elements $\langle X | Q_i | B \rangle$ are influenced by long distance (i.e. low energy) strong interactions (here $|B\rangle$ represents the B meson and $|X\rangle$ its decay mode). Therefore, unlike the Wilson coefficients, the operator elements cannot be obtained perturbatively due to the confining nature of strong interactions at large distances.

A systematic treatment of the hadronic matrix element

$$M[B \rightarrow Kll] = \langle l(p_-) \bar{l}(p_+) K(p_K) | \mathcal{H}_{eff} | B(p_B) \rangle \quad (3.74)$$

is available in the large recoil region. We denote by p_B , p_K , p_- and p_+ the 4-momenta of the B-meson, kaon, lepton l and antilepton \bar{l} , respectively, and M_B , M_K and m_l are the corresponding masses. At large recoil the energy E of the K-meson is large compared to the typical size of hadronic binding energies $\Lambda_{QCD} \ll E$ and the dilepton invariant mass squared $q^2 = (p_- + p_+)^2$ is low, $q^2 \ll M_B^2$. Consequently, in this region the virtual photon exchange between the hadronic part and the dilepton pair and hard gluon scattering can be treated in an expansion in $1/E$ using either QCDF or Soft Collinear Effective Theory (SCET). Furthermore, only one soft form factor $\xi_P(q^2)$ appears in the $B \rightarrow K$ heavy-to-light decay amplitude due to symmetry relations in the large energy limit of QCD.

$$\begin{aligned} \mathcal{M}[B \rightarrow K l \bar{l}] = & i \frac{G_F \alpha_e}{\sqrt{2} \pi} V_{tb} V_{ts}^* \xi_P(q^2) \left(F_V p_B^\mu [\bar{l} \gamma_\mu l] + F_A p_B^\mu [\bar{l} \gamma_\mu \gamma_5 l] + (F_S + \cos \theta F_T) [\bar{l} l] \right) \\ & + (F_P + \cos \theta F_{T5}) [\bar{l} \gamma_5 l] \end{aligned} \quad (3.75)$$

Here, θ denotes the angle between the direction of motion of the B and the negatively charged lepton l in the dilepton center of mass frame. The F_i factors are given in [5]

Finally, the decay rate Γ_l [5], for the standard model prediction is given by

$$\Gamma_l^{SM} = \frac{\Gamma_0}{3} \int_{q_{min}^2}^{q_{max}^2} dq^2 \xi_P^2(q^2) \sqrt{q^3} (|F_A|^2 + |F_V|^2) \times \left\{ 1 + \mathcal{O}\left(\frac{m_l^4}{q^4}\right) + \frac{m_l^2}{M_B^2} \times \mathcal{O}\left(a_s, \frac{q^2}{M_B^2} \sqrt{\frac{\Lambda_{QCD}}{E}}\right) \right\} \quad (3.76)$$

and therefore, if the total decay rate Γ is known, the branching ratio for this decay is calculated as

$$\mathcal{B} = \frac{\Gamma_l^{SM}}{\Gamma}. \quad (3.77)$$

Owing to (3.76) decay rate, R_K is expected to be unity within an uncertainty of $\mathcal{O}(10^{-3})$ in the SM.

3.7 $B \rightarrow J/\psi K, J/\psi \rightarrow \mu^+ \mu^-$

3.7.1 $B \rightarrow J/\psi K$

At the quark level the decay $B^+ \rightarrow J/\psi K^+$ can be described as the \bar{b} -quark decay (by exchanging a W-boson) into a $c\bar{c}$ -pair and a \bar{s} -quark. Using the same notation someone could also study the $B^+ \rightarrow J/\psi \pi^+$ decay, where the \bar{b} quark decays into a $c\bar{c}$ -pair and a d quark. $B^+ \rightarrow J/\psi K^+$ process is dominated by a Cabibbo-favoured tree diagram. Right diagram in Figure(34) is expected to exhibit negligible CP violation. However on the other hand $B^+ \rightarrow J/\psi \pi^+$ decay is a Cabibbo suppressed decay and is described by the $b \rightarrow \bar{c} d$ transition, and therefore the contribution from the gluonic penguin may lead now to CP violation up to the percent level in contrast with the $B^+ \rightarrow J/\psi K^+$. Hence, the branching fraction $\mathcal{B}(B^+ \rightarrow J/\psi K^+)/\mathcal{B}(B^+ \rightarrow J/\psi \pi^+)$ is estimated to be $\sim 4\%$. The reason we are

also interested in this decay, is that the CMS detector does not include any detector that could be used for particle identification, and therefore, by assuming the kaon's mass for all reconstructed tracks, the contamination from $B^+ \rightarrow J/\psi\pi^+$ to $B^+ \rightarrow J/\psi K^+$ can not be avoidable and must be subtracted.

The branching ratio $\mathcal{B}(B^+ \rightarrow J/\psi K^+)$ is calculated using the leading logarithm approximation [4].

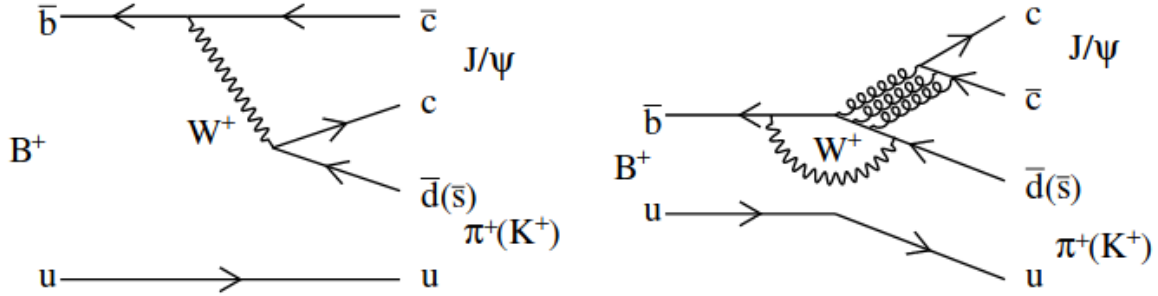


Figure 34: Feynman diagrams for $B^+ \rightarrow J/\psi K^+$ decays at the tree (left) and one-loop (right) level.

The starting point of this mode is again an effective Lagrangian⁸ \mathcal{L} of $\Delta B=1$ electroweak interaction. The Lagrangian for the $b \rightarrow (c\bar{c})s$ transition is given by

$$\mathcal{L}_W = -\frac{4G_F}{\sqrt{2}}V_{cb}V_{cs}^* \left(C_0(\mu_b)\mathcal{O}_0 + C_8(\mu_b)\mathcal{O}_8 \right) \quad (3.78)$$

This Lagrangian (3.78) has been obtained at the first order in perturbation theory in the electroweak coupling G_F (Fermi coupling) and the CKM-matrix elements $V_{cb}V_{cs}^*$. The flavor changing $\Delta B = 1$ operators \mathcal{O}_i are products of two quark currents

$$\mathcal{O}_0 = [\bar{s}\gamma_\mu P_L b][\bar{c}\gamma^\mu P_L c] \quad (3.79)$$

$$\mathcal{O}_8 = [\bar{s}\gamma_\mu P_L T^{\alpha b}][\bar{c}\gamma^\mu P_L T^{\alpha c}] \quad (3.80)$$

These operators are related to the electroweak W -boson exchange operators with the “natural” spinor content $[\bar{s}\dots c][\bar{c}\dots b]$ by a Fierz transformation. In the following, \mathcal{O}_0 and \mathcal{O}_8 as to the singlet and octet operators, respectively. The Wilson coefficients C_i depend on the scale $\mu_b \sim m_b$ which is of the order of the b -quark mass and contain the resummed leading QCD logarithms of the form $\ln(\mu_b/\mu_W)$ to all orders in α_s .

The NLO central values of C_0^{NLO} and C_8^{NLO} can be calculated as 0.209 and 2.230 respectively using $\alpha_s(M_Z) = 0.1176$, $M_W = 80.403$ GeV, $M_Z = 91.1876$ GeV, $m_b(m_b) = 4.2$ GeV, $\mu_W = M_W$ and $\mu_b = m_b$. It should be noted firstly, that the octet Wilson coefficient is one order

⁸Someone could use an effective Hamiltonian as 3.6.

larger than that one for the singlet and secondly, that the NLO correction to the singlet and Wilson coefficient is roughly +50% since $C_0^0 = 0.110$. More details for this approximation can be found in [4]. Similar calculation can be carried out for the $\psi(2S)$ resonance.

3.7.2 $J/\psi \rightarrow \mu^+ \mu^-$

The J/ψ meson consists of a charm quark and a charm antiquark. It is the lightest meson of the "charmonium" family. Despite the fact that the hadronic and semi-hadronic decay modes are the dominant ($\mathcal{B} \sim 85\%$), they are strongly suppressed due to the color factors ($\mathcal{O} \alpha_s^6$), and hence, electromagnetic modes ($\mathcal{B} \sim 10\%$) are more easy to be detected. Furthermore, charmonium states are on the boundary between perturbative and non-perturbative regimes so their decays, especially the hadronic ones, could be used to study QCD. However, the experimental signature of the electromagnetic modes and especially from the one with the two muons in the final state, are powerful and clear observation of these modes. And therefore, we will also use the dimuon decay mode to normalize the rare decay mode and to cancel as more as possible systematic uncertainties.

The study of this decay can be made by studying the $c + \bar{c} \rightarrow \ell + \bar{\ell}$ scattering. However, the two c quarks are not free particles but form bound states, and therefore NLO contributions (like the one in Figure (35)) need to be considered, but these contributions in order to be added properly need to be renormalized. After the renormalization process the decay width can be estimated[29] as

$$\Gamma(J/\psi \rightarrow \ell^+ \ell^-) = 16\pi \frac{\alpha^2}{Q_c^2} m_{J/\psi} |\Psi_{J/\psi}(0)|^2 \left(1 - \frac{16}{3} \frac{\alpha_s}{\pi}\right) \quad (3.81)$$

where the terms $16\pi \frac{\alpha^2}{Q_c^2} m_{J/\psi}$ are due to the $c - c\bar{c} \rightarrow \ell^+ + \ell^-$ scattering process and the terms $|\Psi_{J/\psi}(0)|^2 \left(1 - \frac{16}{3} \frac{\alpha_s}{\pi}\right)$ are due to the higher order contributions and $\Psi_{J/\psi}(0)$ the radial wave function of the J/ψ at the origin [29].

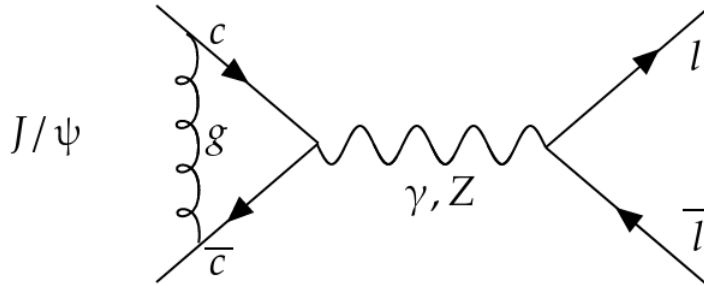


Figure 35: Feynman diagram for $J/\psi \rightarrow \ell \bar{\ell}$

4 Analysis

4.1 Trigger Strategy

CMS collaboration reconstruct muons as described in (2.2.1). Muons are used widely as triggering objects, due to their effective reconstruction and their clear signature. For example there are triggers searching for two muons in specific charmonium resonances or other quarkonium resonances. There are also triggers that search for displaced muons or for highly energetic muons.

In this analysis, we benefit from the fact that according to QCD, flavors are produced in particle-antiparticle pairs. For example a b quark is not produced as a standalone particle, but as a $b\bar{b}$ pair. The trigger logic is to detect muon(s) from semi-leptonic decays of the one b hadron leaving the other b hadron totally unbiased, and free to decay via any decay mode. In order to collect enough statistics for the $B^+ \rightarrow K^+ e^+ e^-$ channels and since there is not a dedicated electron trigger, a single-muon triggering strategy was used to collect more than 10^{10} events were parked tagging at muons coming from one b quark. Using this technique the second b quark (or the other quark from the $b\text{-}b\bar{b}$ pair) would remain totally unbiased and free to decay via all possible modes. In order to tag muons from b-decays, the single-muon trigger that is looking for displaced muons ($d_{xy}/\sigma(d_{xy}) > 4$). With the sample size of $\mathcal{O}(10^{10})$ decays, one could probe rare B hadron decays with branching fractions as low as $\sim 10^{-7}$ making it possible to search for lepton non-universality. Hence, if we really detect the first b candidate decayed via the semi-leptonic mode, we do know that in the rest event the other b decay mode must be recorded.

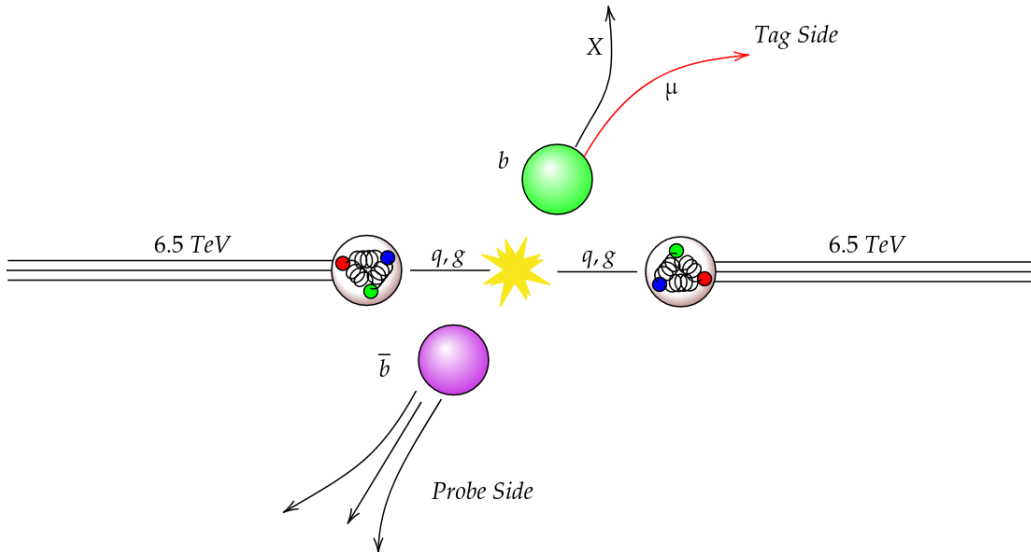


Figure 36: A schematic view of the Trigger Logic. The "Tag Side" candidate is biased by the trigger cuts while the other b decay is totally unbiased.

The trigger logic for event selection is to detect semi-leptonic decays of b hadrons ("tag-side") that emit a muon with high transverse momentum. The logic based on the presence of a single muon accounts for approximately 20 % of all b hadron decays. This strategy allowed to record both the (signal-side) muonic and electronic final states required for the R_K measurements. The purity (number of events that include a hadronic decay with at least one muon direct or indirect from a b decay over all events) firing the trigger is estimated to be $\sim 60-90\%$ with discrepancies depending on the P_T and $|d_{xy}|/\sigma(d_{xy})$ cuts. For the HLT_Mu9_IP6 bPurity is estimated to be 75-82%

The L1 logic requires the presence of a muon with $P_T > 7$ but satisfying $|\eta| < 1.5$. This requirement helps to control the L1 rate. All the HLT paths are seeded by the same soup of L1 seeds, which are activated by the instantaneous luminosity, for example HLT_Mu9_IP6 is fed by L1_SingleMu10er1p5. HLT_Mu9_IP6 is the trigger that will be used for the measurement of R_K since it is the one with the higher statistics and a measurement using the overlap between other triggers is very complex. Both in the names of L1 seeds and HLT paths, Mu"X" stands for the P_T threshold of the HLT muon, er"X"p"Y" stands for the $|\eta|$ cut, IP"X" for the $|d_{xy}|/\sigma(d_{xy})$ cut that the HLT muons need to pass during the online reconstruction of the L1 triggering. In the case of HLT_Mu9_IP6, online L1 triggering muons will be excluded if they fail to pass either the $P_T > 10$ GeV or the $|\eta| < 1.5$ cut or the online HLT $P_T > 9$ GeV, $|\eta| < 1.5$ and $IP > 6$ cuts.

4.2 HLT-Reco Muon Matching

$R_K(\mu)$ given in (3.66) will be measured for the purpose of this thesis only in the tag side, since for a standalone measurement for the $R_K(\mu)$ the tag side is superior due to much higher statistics. The tag side is formed by the reconstructed muons in each event that fired at least one trigger. If a B candidate is reconstructed by at least such a muon, the B candidate will be labelled as a tag candidate. To begin with, let's find the tag muons.

As mentioned in (2.2.3), HLT muons' P_T is mainly measured using tracks in the muons' chambers, while for the rest muons their P_T is measured using the track in the tracking system. Hence the resolution for the two reconstructions is slightly different. Furthermore, HLT muons may have been scattered multiple times passing through the iron yoke or through the superconducting solenoid and therefore, tracks in the muons chambers may not be matched exactly with the reconstructed tracks in the tracking system. Since, the P_T for the two muon categories is measured using different segments of the tracks, it is possible that a reconstructed track will not be identical with a HLT track.

In the barking dataset, reconstructed muons and their properties are stored in the MiniAODs file without labelling them as tag or probe muons. So the first thing that is required to reconstruct the B candidates is to find the tag muons, which means that a matching process between them and the HLT-muons needs to be done. For this purpose, two functions

- `if(muon.triggerObjectMatch(i)!=0`
- `muon.triggerObjectMatch(i)->hasPathName("path",true,true))`

from the CMSSW environment will be used. The first function ensures that the muon is matched with a trigger object and the second that the trigger muon is recorded by the HLT "path".

The first true option is used for the 'pathLastFilterAccepted' forcing the HLT object to be used in the final filter of a succeeding path and the second true option for the 'pathL3FilterAccepted' is used to consider only objects from L3 filters⁹. But this matching function do not ensure that reconstructed muons are matched correctly with the HLT muons. Indeed, if two or more reco muons are close, both could be matched with the same HLT muon, and vice versa, if two or more HLT muons are close they could be matched with the same reco muon. To avoid all these multiple matching-candidates, the $\Delta R = \sqrt{\Delta\eta^2 + \Delta\phi^2}$ value is calculated manually between all reconstructed muons and their matched HLT muons and only the pair per reconstructed muon with the minimum ΔR is kept. After this process if there are multiple reconstructed muon matching the same HLT muon, only the minimum ΔR pair is kept.

This process, ensures basically two things: The first one is that there is a one-to-one correspondence between the reconstructed and the HLT muon collections forcing one reconstructed muon to be matched with only one HLT muon and vice versa even for events with multiple HLT muons. The second one is that the "path" option¹⁰ ensures no contamination from one trigger to another allowing muons' matching even for events with multiple and different trigger bits.

Since there is not a straight-forward connection between the HLT muons and the reconstructed muons from the muon chambers and the tracking system. During this offline matching process between the two muons' collections, reconstructed muons from the muon chambers and the tracking system may be matched with HLT objects but may not satisfy the online trigger cuts. This means that plotting the characteristics of the reconstructed muons, "tails" to lower P_T and IP or bigger η regions may appear. In our case the matching is succeed without any explicit matching but by the usage of those two CMSSW functions.

Reconstructed muons that have passed this process and are matched with HLT muons are labelled as Tag muons. The result of this process is shown in Table (3) and in Figures (37), (38) and (39).

⁹https://cmsdoxygen.web.cern.ch/cmsdoxygen/CMSSW_10_2_15/doc/html/d4/d55/classpat_1_1PATObject.html?fbclid=IwAR2b_qmvYnkQuBilw4Cx6i7qXzPSzIURd8jCq7L8CvfuLPdpDLUBBjoR8oM#a332b56f8f978ea9382cf51f87adee245

¹⁰which in our case will be replaced with the "HLT_Mu_9IP6".

Table 3: Almost 97% of the events passing all triggers have one HLT muon and the rest 3% has multiple HLT muons. After the above-mentioned matching process, in almost 0.5% of the events, none of the reconstructed muons are matched with any of the HLT muons and more than 99% of the events have a reconstructed muon that is labelled as a tag muon. As we can see there is an inefficiency for the events with multiple HLT muons, but this is due to fake HLT muons (tracks that are created by a single muon) and due to mismeasurements and failed extrapolations from different parts of the detector.

Events with	Fraction (%)
0 HLT Muons	0
1 HLT Muons	97.2
2 HLT Muons	2.7
>2 HLT Muons	0.1
0 Tag Muons	0.51
1 Tag Muons	99.17
2 Tag Muons	0.23
>2 Tag Muons	0.001

Let's focus now on the HLT_Mu9_IP6 trigger. All the following distribution were plotted using 1 million events from ParkingBPH1-Run2018A samples.

As we can see in Figure (37) (left), the ΔR distribution is limited to $\Delta R \leq 0.1$ values between reconstructed and HLT muons that are below 0.1. This feature is inherited by the used CMSSW functions. Since this matching process is not explicit but it is coming from the CMSSW itself, no stricter cut is used for the ΔR value. Another feature that someone should notice, is the bumpy area in range $[0.006, 0.025]$, which is considered to be created by muons that have been scattered multiple times and as a result the reconstructed track and the HLT track are not identical. In Figure (37) (right), we see the ΔP_T -relative distribution for the tag muons that have succeed in the previous matching process. As we can see, there is a suppression to positive ΔP_T relative values which means that the P_T of the HLT muon is smaller than the corresponding P_T of the reconstructed muon. This is in agreement with the fact that reconstructed muon's P_T is mainly seeded by the track of the tracking system where the muon has not interact yet with significant amount of material and has not loose significant part of its energy. On the other hand, HLT muons' track is seeded by the hits in the muon chambers, where the arriving muons have been scattered and have lost parts of their energy, passing through the calorimeters and the solenoid.

In Figure (38) (left) we see a 2D comparison of the two previous distributions. The P_T of the reconstructed muons that are labelled as tag muons is represented in Figure (38) (right). As we can see this spectrum does not appear a sharp cut at 9 GeV, but in contrast there is a normal raise for the yield up to 9 GeV and for the rest of the spectrum, the raise is replaced by an almost linear decrease. Furthermore, in Figures (39) (left) and (39) (right) the η and the $|d_{xy}|/\sigma(d_{xy})$ of the tag muons are depicted. In Figures (38) (left), (39) (left),

right), we can see that, indeed, there are tails beyond the cut regions. As mentioned above this tails are due to the offline matching process. Someone could also notice that indeed, the η spectrum is mainly limited in the $|\eta| < 1.5$ region, where the barrel is extended, and the spectrum is highly affected by the L1 seed, it is strictly limited up to $|\eta|=2.5$ (where the muon chambers can detect muons) and finally, the small gaps in $\sim \pm 1$ and $\sim \pm 0.3$ which correspond to the areas where the 5 barrel wheels are combined composing the barrel part of the detector.

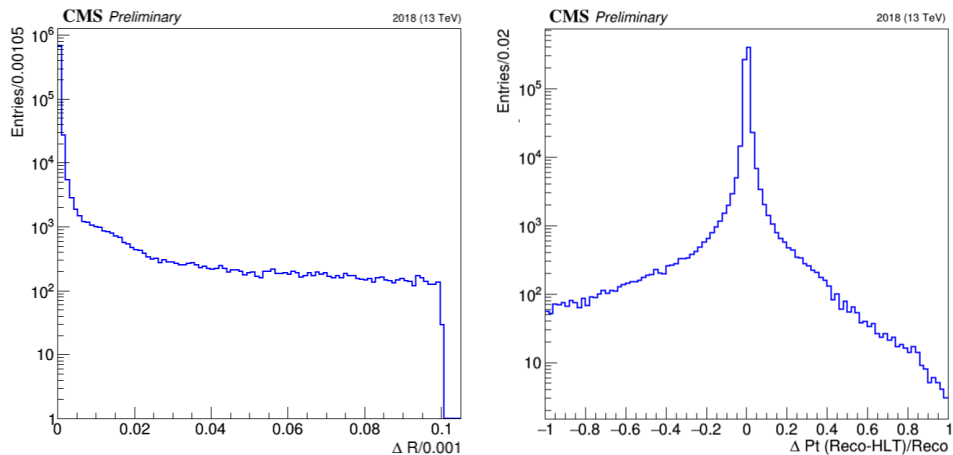


Figure 37: Left: ΔR value between tag muons and their matched HLT muons. Right: ΔP_T relative distribution for tag muons and their HLT partners.

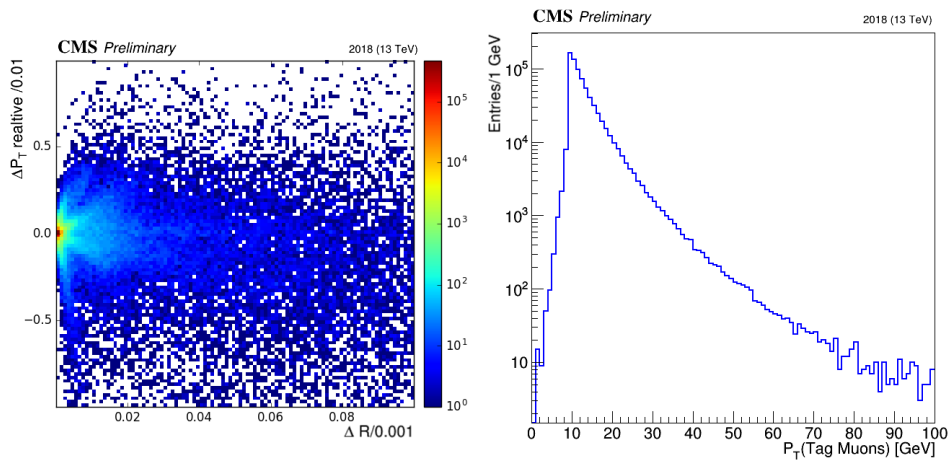


Figure 38: Left: 2D comparison of the P_T relative Vs ΔR values for tag muons with their corresponding HLT muons. Right: Reconstructed P_T spectrum of Tag muons that fired HLT_Mu9_IP6 trigger.

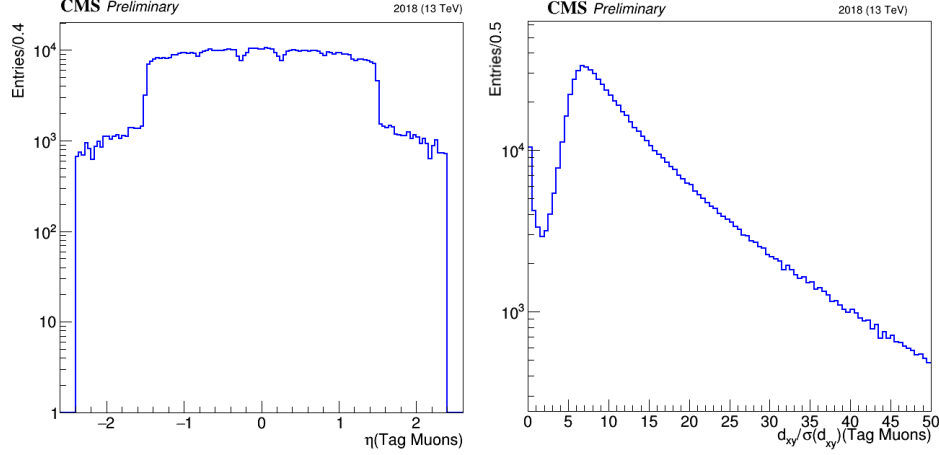


Figure 39: Left: Reconstructed η spectrum of Tag muons that fired HLT_Mu9_IP6 trigger. Right: Reconstructed Impact Parameter spectrum of Tag muons that fired HLT_Mu9_IP6 trigger.

4.3 Dimuon Mass Region

The two decays, $B \rightarrow J/\psi K$, $J/\psi \rightarrow \mu\mu$ and $B \rightarrow \mu\mu K$, that will be reconstructed for the $R_K(\mu)$ measurement, are two decays governed by different kinematics and decay mechanism but with the same particles in final state, a muon, an antimuon and a kaon. The first decay is a two body decay, since the B meson decays to a J/ψ and a Kaon, where the J/ψ decays to a muon-antimuon pair. Therefore, reconstructing only the muons a sharp peak in the J/ψ resonance coming from the $B \rightarrow J/\psi K$, $J/\psi \rightarrow \mu\mu$ decay chain, will be visible. However, the latter is a three body decay and therefore, reconstructing only the two muons, no peak will be visible in the dimuon mass spectrum. In construct, a wide spectrum in the region $2m_\mu = 2 \cdot 0.105 \text{ GeV} < m(\mu\mu) < 5.28 - 0.493 = m_B - m_K$ is expected.

The dimuon mass spectrum at generation level using MC samples is depicted in figure (40). As we can see in figure (40), the dimuon mass spectrum for the three body decay is extended in $[0.2, 4.8] \text{ GeV}$ region and the J/ψ mass region is included in the dimuon mass spectrum of the rare three-body decay. This means that the decays are overlapping in the dimuon mass spectrum and hence they can not be discriminated completely using a mass window in the dimuon mass spectrum, since the rare decay contaminates the J/ψ region. Therefore, a scale factor is required to estimate the number of candidate from the rare decay that are reconstructed as candidates for the resonant mode. A similar scale factor is also required to estimate the number of candidates from the rare decay that are reconstructed as $B^+ \rightarrow \psi(2S)K^+$, $\psi(2S) \rightarrow \mu^+\mu^-$.

Hence, the different signal regions will be defined according to diffent q^2 regions, where q^2 is the invariant mass of the lepton pair. Each reconstructed B candidate with dimuon mass less than 2.5 GeV (low q^2 region) is identified as a $B^+ \rightarrow \mu^+\mu^- K^+$ candidate, while reconstructed B candidates with dimuon mass in $[2.9, 3.2] \text{ GeV}$ region and in $[3.4, 4] \text{ GeV}$ region are identified as $B^+ \rightarrow J/\psi K^+$, $J/\psi \rightarrow \mu^+\mu^-$ and $B^+ \rightarrow \psi(2S)K^+$, $\psi(2S) \rightarrow \mu^+\mu^-$

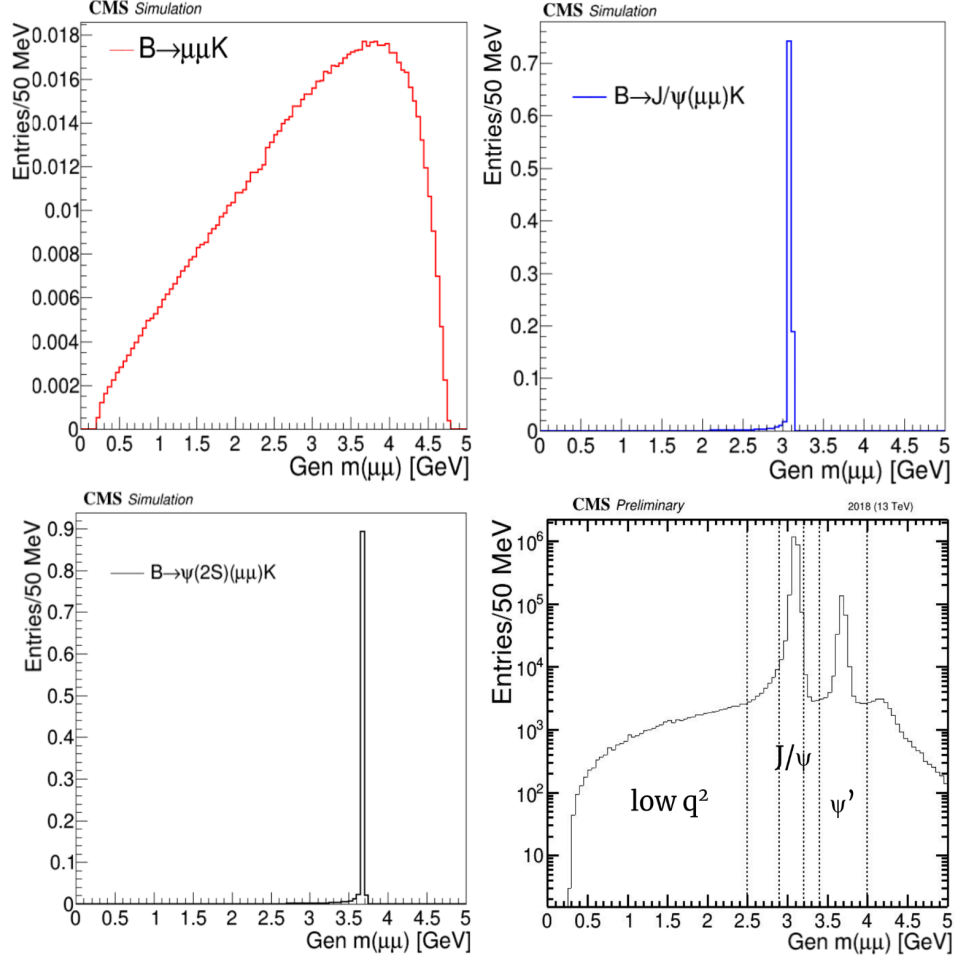


Figure 40: Generated dimuon spectrum for the three decays $B^+ \rightarrow \mu^+\mu^-K^+$ (top left), $B^+ \rightarrow J/\psi K^+$, $J\psi \rightarrow \mu^+\mu^-$ (top right) and $B^+ \rightarrow \psi(2S)K^+$, $\psi(2S) \rightarrow \mu^+\mu^-$ (bottom left). In the bottom right plot the reconstructed dimuon mass spectrum is depicted.

candidates respectively. All candidates in $[2.5, 2.9]$ and $[3.2, 3.4]$ GeV regions will be excluded since in these regions radiative tails are expected. As for the dimuon mass spectrum overlap in the J/ψ and ψ' resonances, it will be subtracted using scale factor.

4.4 B meson reconstruction and preselection cuts

Now, since the reconstructed muons that fired HLT_Mu9_IP6 have been found, they can be used to reconstruct the B candidates.

The B^+ candidates are formed by combining two charged muonic trajectories with a track from the tracking system. For the purpose of this thesis, The $R_K(\mu)$ will be measured only in the tag side, which means that at least one of the muons that will be used for the B meson reconstruction must be a tag muon.

The reconstruction begins by creating doublets of opposite charged muons. However, not all doublets are used for this process, since we know that the dimuon mass spectrum from the rare mode is expanded in the $[0,4.8]$ GeV region. Hence, only doublets with mass in the $[0,5]$ GeV region are kept. To avoid ghost and fake tracks (tracks that are reconstructed by hits that in reality belong to other tracks but are rejected by the fitting processes and therefore they form different tracks but they are fake tracks), all tracks with that are within $\Delta R < 0.03$ with respect to tag muons are rejected. To limit the combinatorics and the random candidates with the desired mass windows, all tracks must be within $\Delta z < 1$ cm with respect to the tag muon. Also, low P_T thresholds for the muons' and kaons' tracks are used to reduce combinatorics. Muonic doublets and B candidate need to satisfy loose probability criteria to form SV vertices.

There are some extra preselection cuts that are applied in order to reconstruct a B candidate, like the reconstructed $P_T(B) > 3$ GeV requirement or the $\cos \alpha_{2D_{xy}} > 0$, where the angle $\alpha_{2D_{xy}} > 0$ is the angle formed by the line segment, connecting the PV and the SV, and the vector of the reconstructed $P\vec{P}(B)$, projected in the 2D x-y surface, as depicted in figure (41). In figure (41), the L_{xy} decay length in the xy surface is also defined. The absolute value of this distance divided by its error bar defines the L_{xy} significance.

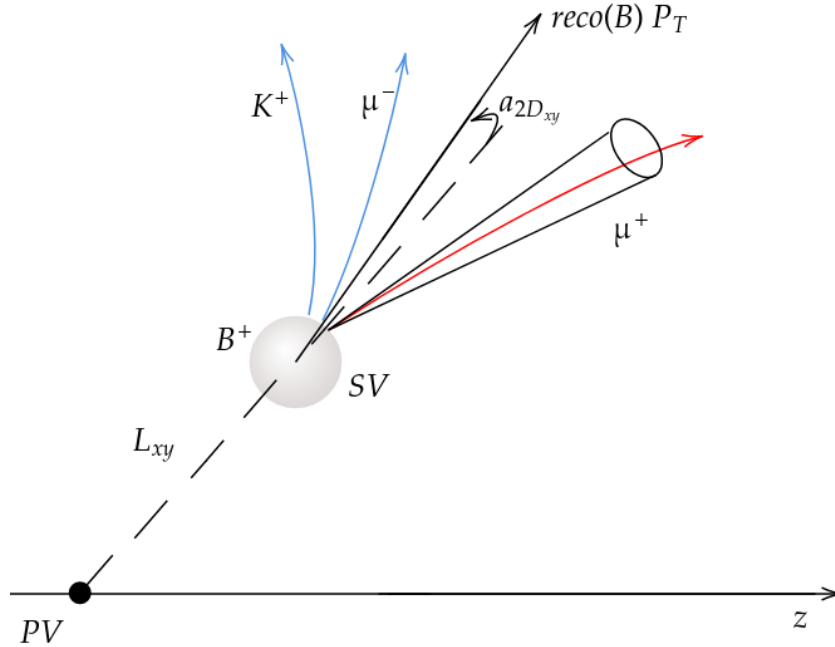


Figure 41: The reconstructed decay vertex and its properties. The tag muon is labelled with red color.

The complete set of preselection cuts is shown in figure (42).

The two lepton tracks and the hadron track are fitted to a common vertex through the KinematicFit package available in CMSSW. The algorithm, which is based on Least Means

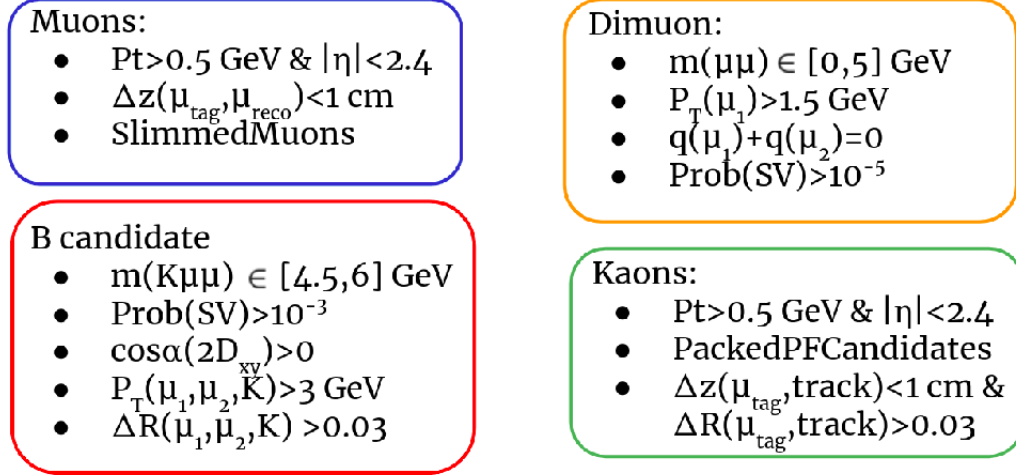


Figure 42: The reconstructed decay vertex and its properties. The tag muon is labelled with red color.

Square minimisation, constrains the tracks of the B^+ daughter particles to come from a single vertex and provides the vertex position, covariance matrix, and χ^2 .

Since the vertexing is performed, the particle trajectories are refitted to a common vertex applying additional constraints. For the rest parts of reconstruction and calculations, the refitted momenta and kinematic variables are used.

4.5 acceptance \times efficiency for Tag Side

To measure the R_K ratio, we need to know the fraction of the decays that are either not detected by the detector, for example particles that are in the forward region are not detected at all since they are not creating hits and tracks, either fail to pass the reconstruction process, either fail to pass the preselection criteria or fail to pass the rest selection criteria. The first fraction, the part of decays with products that are moving towards region with no detector or they are moving towards regions where specific thresholds are required, is given by the acceptance factor. Acceptance is therefore, the fraction of decays that can be detected by the different parts of the detector.

On the other hand, even if a particle is within detector's (geometrical or not) acceptance, it may not be reconstructed. Hence, we need to match the generated particles with their reconstructed tracks and we need to combine them in vertices. Particles that fail this matching process can not be used to reconstruct B candidates. All these cases, where particles are not reconstructed, or fail to pass reconstruction criteria are taken into account in the efficiency factors.

To begin with, as mentioned in (3.66), $R_K(\mu)$ will be measured only in the tag side. Therefore the $\alpha \times \varepsilon$ factor must consider the fraction of decays that the trigger detects. We are working with HLT_Mu9_IP6 trigger fed by the L1_SingleMu10er1p5 seed. Therefore,

we need to calculate the fraction of B^+ meson with at least one muon passing the trigger, namely to measure the $(\alpha \times \varepsilon)_{trg}$.

In order to measure the $\alpha \times \varepsilon$ factor with precision lower than 1%, two different MC samples are used, one unbiased sample¹¹ and one filtered sample¹², where generated B^+ candidates with at least one muon passing $P_T > 5$ GeV and $|\eta| < 2.5$ are stored to save statistics and to measure lower error bars. Thus, the unbiased sample will be used to measure the fraction of B^+ mesons, decaying to $B^+ \rightarrow \mu^+ \mu^- K^+$ and to $B^+ \rightarrow J/\psi K^+$, $J/\psi \rightarrow \mu^+ \mu^-$ with at least one generated muon passing the filter cuts ($P_T > 9$ GeV and $|\eta| < 2.5$) and, then, the biased-filtered samples, with enriched statistics (~ 10 millions events) will be used for the rest part of acceptance \times efficiency calculation.

In figure (43), the $P_T(B^+)$ and $y(B^+)$ spectra at generation level are depicted.

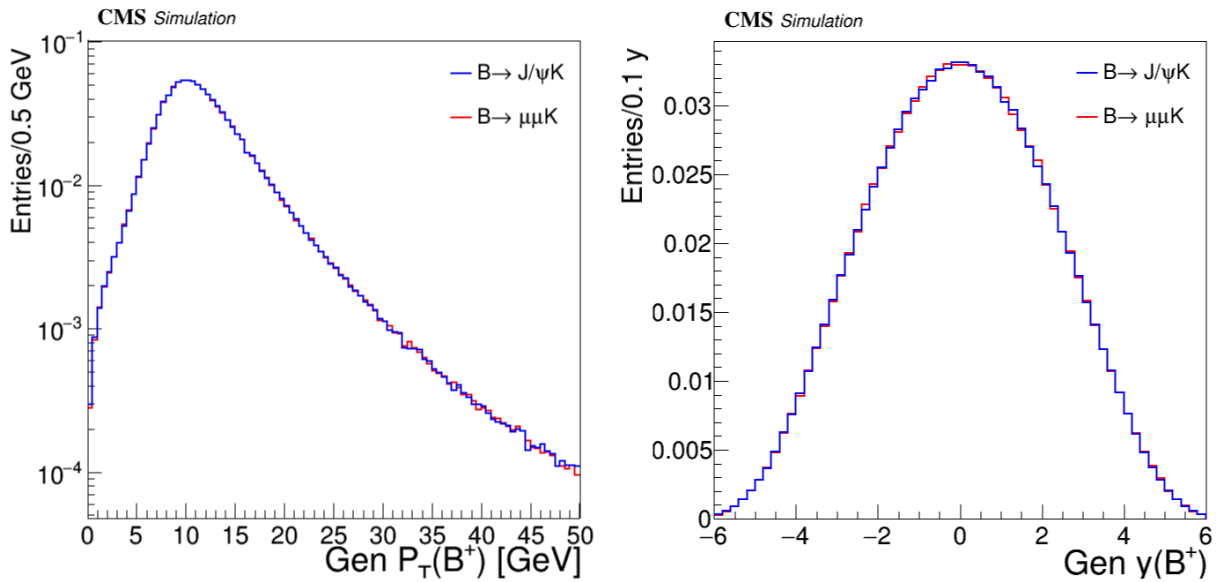


Figure 43: The $P_T(B^+)$ and $y(B^+)$ spectra at generation level for the two decays. As we can see the spectra for the two decay modes are identical, which reflects the fact that this spectra are associated with the production mechanism of the B^+ meson and not with the decay mechanism.

In figure (44), the $P_T(\mu)$ and $\eta(\mu)$ spectra for the leading muon (higher P_T) are depicted superimposed with the corresponding spectra for the subleading muon (lower P_T). In the same figure the ratio of the leading μ spectra are depicted.

¹¹which, however, is not totally unbiased. In contrast, a $P_T(b(\text{Hat})) > 9$ GeV was applied, where $P_T(b(\text{hat}))$ is the b quark's momentum which is hadronised to the B^+ meson.

¹²To be more precise, these samples have been produced centrally for the full CMS analysis and hence they were not produced for the specific measurement in the tag side. Indeed, the production was made demanding three generated muons, that could affect the spectra and the acceptance factors in case the two B mesons are kinematically associated.

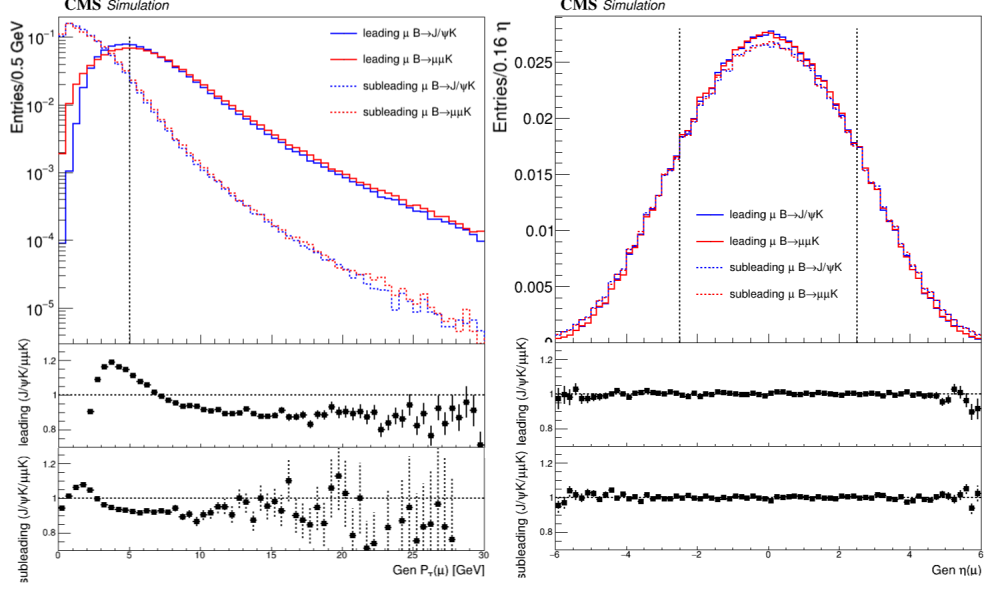


Figure 44: The leading and subleading $P_T(\mu)$ (left) and $\eta(\mu)$ (right) spectra at generation level for the two decays. As we can see, the P_T spectrum for the resonant mode is suppressed with respect to the rare mode above 7 GeV for the leading μ and above 3 GeV for the subleading μ . This effect is due to the fact that the acceptance increases with the dimuon mass. As we can see with the corresponding plot (in section (4.10)) for the $B^+ \rightarrow \psi(2S)K^+, \psi(2S) \rightarrow \mu^+\mu^-$ comparison, the $P_T(\mu)$ spectrum for the resonant mode is even more suppressed with respect to the $\psi(2S)$ mode. The η distributions do not appear significant deviations and hence the ratio is close to unity. The dashed lines represents the P_T and η cuts.

Therefore, in table (4) the α_{filter} factors, fraction of generated B^+ candidates with at least one muon passing $P_T > 5$ GeV and $|\eta| < 2.5$ over all generated B, for the two decays are listed.

Table 4: α_{filter} factor for the two decays.

Channel	$\alpha_{filter}(\%)$
$B^+ \rightarrow J/\psi(\mu^-\mu^+)K^+$	43.679 ± 0.064
$B^+ \rightarrow \mu^-\mu^+K^+$	44.021 ± 0.063
ratio	0.9922 ± 0.063

Since we have calculated the fraction of two decays that passed the filter, we will calculate now the fraction of B candidates whose decay products passed at generation level the P_T and η cut given the fact that at least one muon passed the filter cuts. In figure (45) the filtered spectra for the leading and subleading μ are shown. In figure (46), the acceptance of B^+ meson as a function of $P_T(B^+)$ and $y(B^+)$ at generation level is shown.

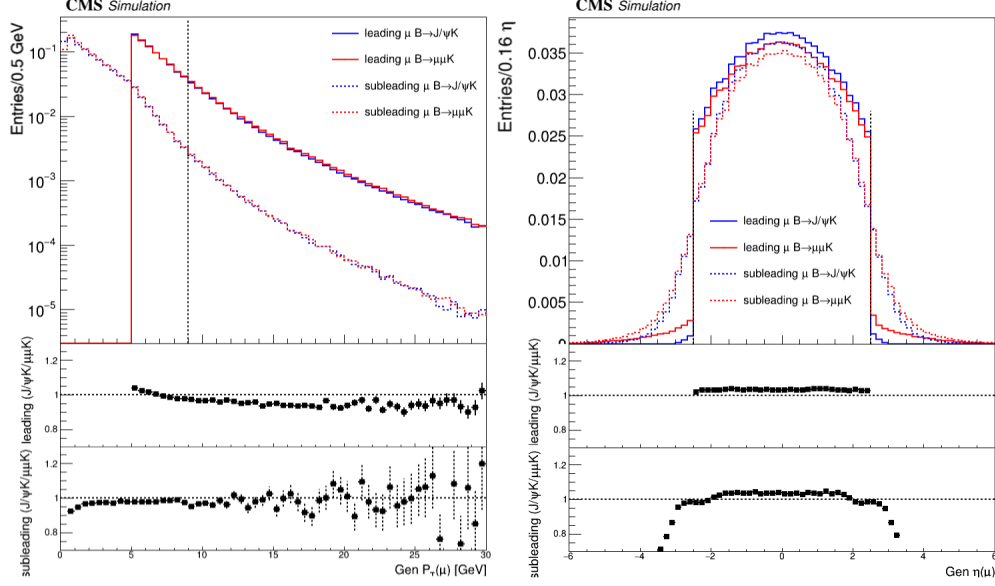


Figure 45: Filtered Spectra at generation level for leading and subleading μ for the two decays. The tails that are visible in the η spectrum are due to events where the subleading μ is the one that passed the filter, and since it satisfies the two filter cuts the leading μ must satisfy the $P_T(\text{leading}) > P_T(\text{subleading}) > 5$ GeV requirement.

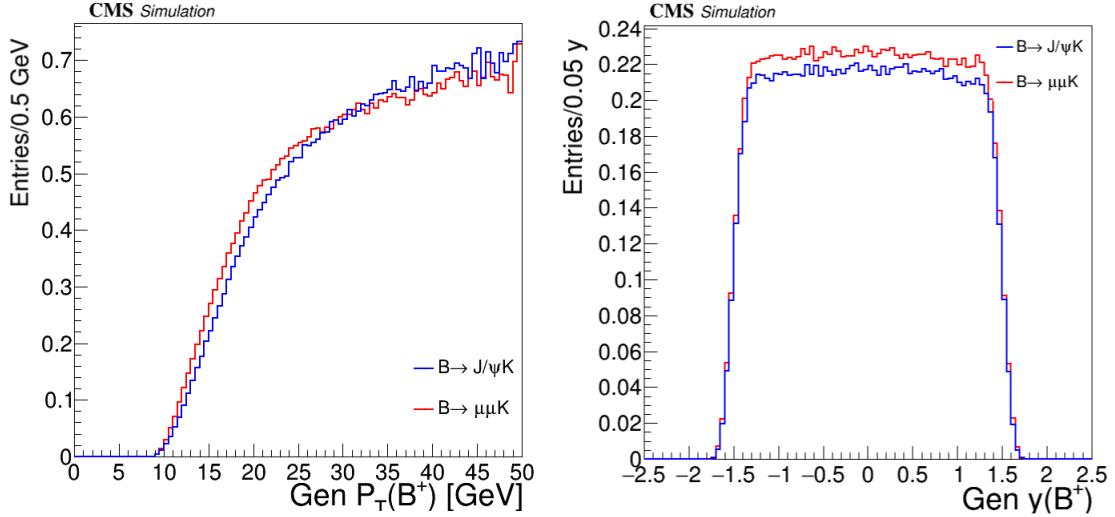


Figure 46: Acceptance as a function of $P_T(B^+)$ and $y(B^+)$ at generation level.

In table (5) the acceptance factors using filtered samples and hardening the cut up to the trigger cuts are list. All numbers are relative.

Therefore, the total trigger acceptance factors (α_{trg}) listed in table (6), the fraction of generated B^+ mesons decaying via the desired modes with at least one muon satisfying at gen

Table 5: $\alpha(|\eta| < 1.5)\%$ and $\alpha(P_T > 9 \text{ GeV})$ factors for the two decays given they passed the filter cuts.

Channel	$\alpha(\eta < 1.5)(\%)$	$\alpha(P_T > 9 \text{ GeV}) (\%)$
$B^+ \rightarrow \mu^- \mu^+ K^+$	65.087 ± 0.034	21.509 ± 0.021
$B^+ \rightarrow J/\psi(\mu^- \mu^+) K^+$	64.964 ± 0.032	22.456 ± 0.020

Level the P_T and η cuts over all decays satisfying or not the trigger-filter cuts is calculated by multiplying the factors of tables (4) and (5).

Table 6: The α_{trg} factor for the two decays. The error bars have been calculated using error propagation and by adding them quadratic.

Channel	$\alpha_{trg}(\%)$
$B^+ \rightarrow J/\psi(\mu^- \mu^+) K^+$	6.137 ± 0.011
$B^+ \rightarrow \mu^- \mu^+ K^+$	6.442 ± 0.010
ratio	0.953 ± 0.014

As mentioned above, the triggers are not searching only for muons satisfying $P_T > 9 \text{ GeV}$ and $|\eta| < 1.5$ requirements but also for displaced muons satisfying $IP_{sig} = |d_{xy}|/\sigma(d_{xy}) > 6$. However, the IP_{sig} can not be measured at generation level since the desired information is not stored in NanoAODs root files. Hence, the effect of this cut can only be measured at reconstruction level. Thus, we need to match the generated muons passing the trigger cuts with reconstructed tracks. This matching is done again by calculating the ΔR for the generated muon with all reconstructed muons. The reconstructed muon with the minimum ΔR among all reconstructed muons is the one that is matched with the generated particles. To avoid matching generated particles with random tracks or with multiple scattered tracks, matching process is limited by using pair with minimum ΔR less than 0.03. Instead of keeping all the reconstructed muons, we are keeping only those, that have been labelled as "SoftId" muons (2.2.2). The reconstruction efficiency for these muons is measured in table (7). This process can be also done for the rest muons that failed passing the trigger cuts at generation level and for the kaon. The minimum ΔR distribution for the leading and subleading muon and for the kaon is shown in figure (49).

The reconstructed spectra for muons passing all the trigger cuts given they passed the matching process and the SoftId requirement is also shown in figure (47). As we can see in comparison with ε_{cuts} in table (7), the low efficiency factor is due to the $|d_{xy}|/\sigma(d_{xy}) > 6$ requirement.

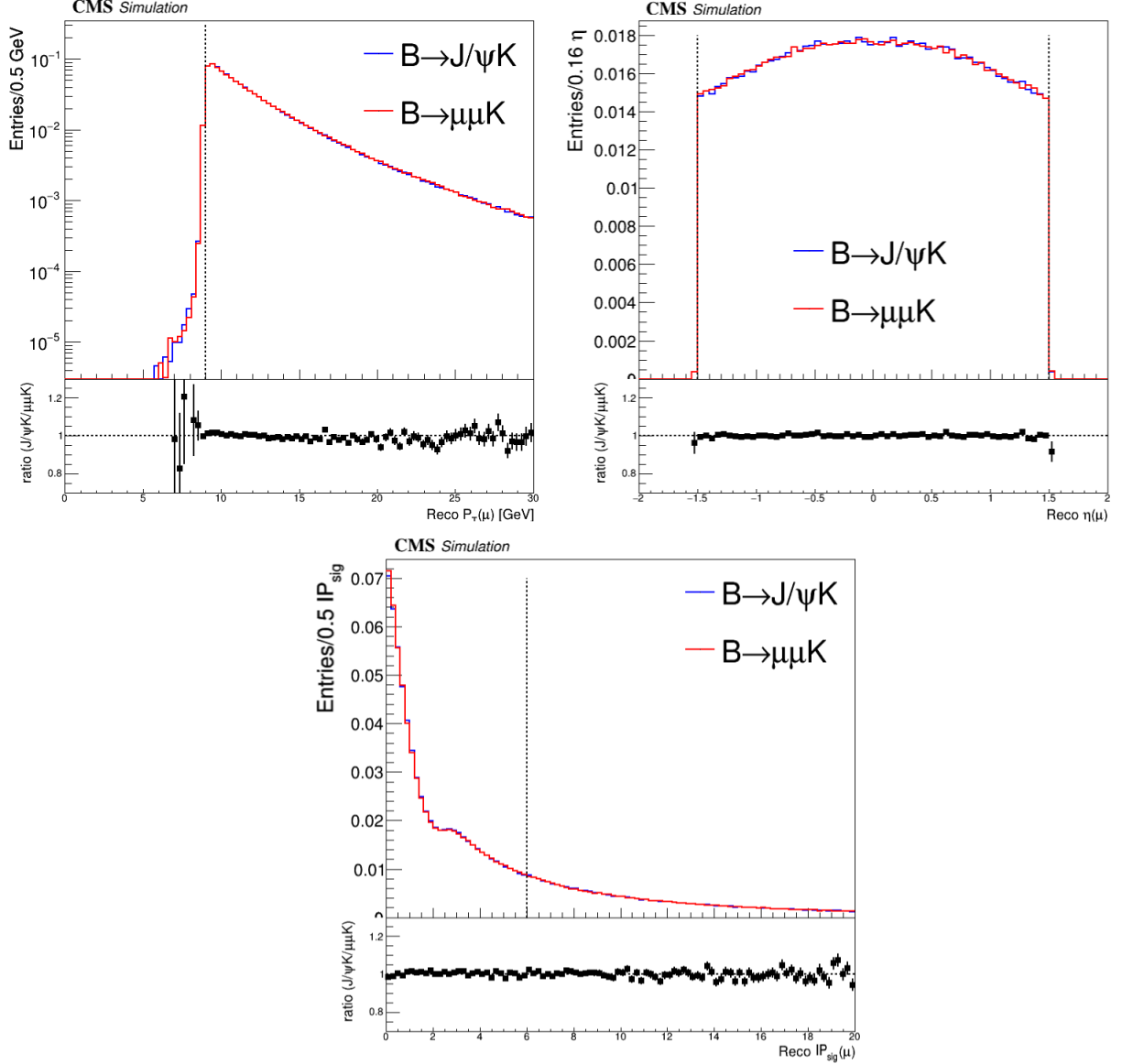


Figure 47: $P_T(\mu), \eta(\mu)$ and $IP_{sig}(\mu)$ spectra for muon passing at generation level the P_T and η trigger cuts.

Table 7: Reconstruction and Trigger efficiency for the two channels.

Channel	$\varepsilon_{reco}(\%)$	$\varepsilon_{cuts}(\%)$	$\varepsilon_{HLT}(\%)$	$\varepsilon_{total}(\%)$
$B^+ \rightarrow J/\psi(\mu^- \mu^+) K^+$	97.43 ± 0.12	30.699 ± 0.057	93.43 ± 0.22	27.95 ± 0.05
$B^+ \rightarrow \mu^- \mu^+ K^+$	97.46 ± 0.11	30.717 ± 0.051	93.27 ± 0.20	27.92 ± 0.05

Then, we calculate ε_{HLT} factor, which is the fraction of reconstructed muons labelled as tag according to process in (4.2) given they passed the trigger cuts at reconstruction level.

This factors are also listed in (7) and the trigger efficiency as a function of reconstructed $P_T(\mu)$, reconstructed $\eta(\mu)$ and reconstructed $|d_{xy}|/\sigma(\mu)$ is shown in figure (48).

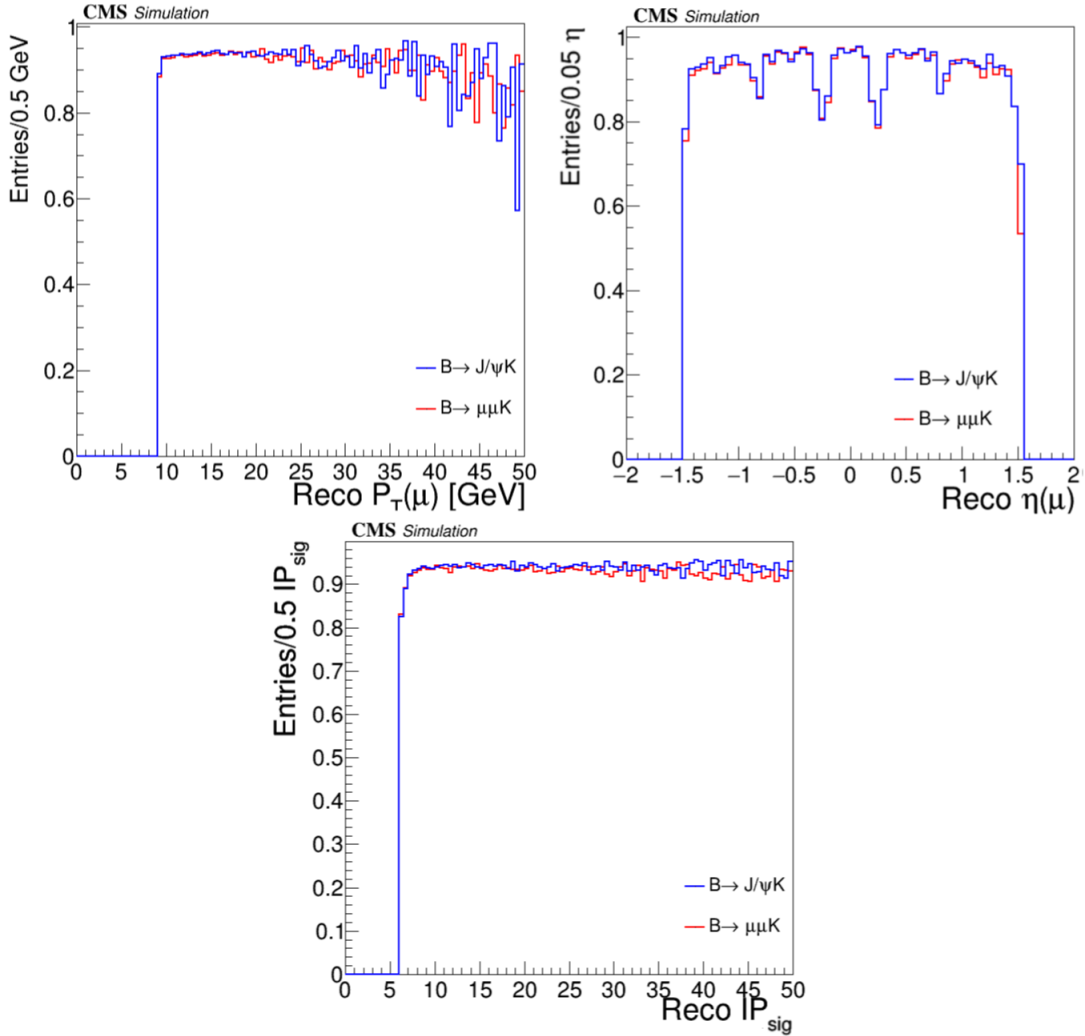


Figure 48: Trigger efficiency as a function of reconstructed $P_T(\mu)$, reconstructed $\eta(\mu)$ and reconstructed $|d_{xy}|/\sigma(\mu)$.

Therefore the total $(\alpha \times \varepsilon)_{trg}$ factor for the two decays can be calculated by multiplying the α_{trg} , ε_{total} (tables (6) and (7)).

Table 8: The total $(\alpha \times \varepsilon)_{trg}$ factor for the two decays.

Channel	$(\alpha \times \varepsilon)_{trg}$
$B^+ \rightarrow J/\psi(\mu^- \mu^+) K^+$	1.7153 ± 0.0039
$B^+ \rightarrow \mu^- \mu^+ K^+$	1.8048 ± 0.0038
ratio	0.9535 ± 0.003

Now, since we have calculated the fraction of decays that the trigger can detect, we calculate the acceptance and reconstruction efficiency factors for the second muon and then we can reconstruct the whole B candidate using at the same time the preselection cuts. The second muon is accepted if it is within $|\eta| < 2.4$ and above $P_T > 2$ GeV, while the kaon is accepted if it is with $|\eta| < 2.4$ and above $P_T > 1$ GeV. Thus, the α_B factor is calculated. Both particles are matched with a reconstructed track if their minimum ΔR with the reconstructed track is below $\Delta R < 0.03$. The second (subleading) muon is required to be a "SoftID" muon again, and hence, the reconstruction efficiency for the subleading muon and the kaon is calculated.

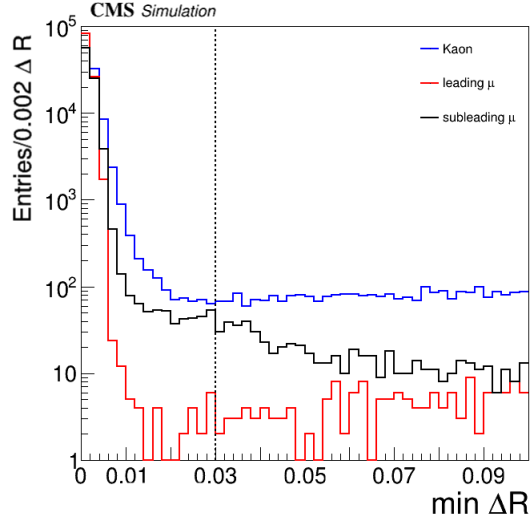


Figure 49: Minimum ΔR Distributions for leading μ , subleading μ and Kaon.

Since, we have matched all generated particles with their reconstructed tracks, the B candidate is reconstructed if the preselection cuts are satisfied. The preselection efficiency is calculated dividing the number of reconstructed B candidates by the number of generated B meson with all decay particles matched with reconstructed tracks. In table (9), the acceptance factor for the subleading muon and the kaon, and the reconstruction \times preselection efficiency factor are listed.

Table 9: Acceptance and reconstruction efficiency for the B candidates given the trigger cuts for the two decays.

Channel	α (%)	$\varepsilon_{reco} \times \varepsilon_{presel}$ (%)	$(\alpha \times \varepsilon)_B$
$B^+ \rightarrow J/\psi(\mu^- \mu^+) K^+$	56.17 ± 0.16	67.12 ± 0.24	37.70 ± 0.12
$B^+ \rightarrow \mu^- \mu^+ K^+$	60.49 ± 0.15	65.90 ± 0.21	39.86 ± 0.11
ratio			0.0964 ± 0.004

Finally, as mentioned in (4.3), each candidate reconstructed in data with $m(\mu\mu) < 2.5$ will be considered as a candidate from the rare mode and each candidate reconstructed in

$2.9 < m(\mu\mu) < 3.2$ GeV mass region will be considered as a candidate from the resonant mode. Therefore the efficiency factors for the mass windows are calculated in the above mentioned limits. Thus, having reconstructed completely the B candidate, we cut on the dimuon mass spectrum to separate the two decay modes and to calculate the efficiency for this cut, which is listed in table (10).

Table 10: Dimuon mass cut efficiency for the two decays.

Channel	$\varepsilon_{m_{\mu\mu}}$
$B^+ \rightarrow J/\psi(\mu^-\mu^+)K^+$	98.35 ± 0.38
$B^+ \rightarrow \mu^-\mu^+K^+$	21.26 ± 0.12
ratio	4.62 ± 0.03

4.6 BDT training and cut

However, if we just plot the mass candidates for $m(\mu\mu K)$ candidates for the two $m(\mu\mu)$ regions (rare and J/ψ resonance), the peak for the rare decay is not optimal, figure (50).

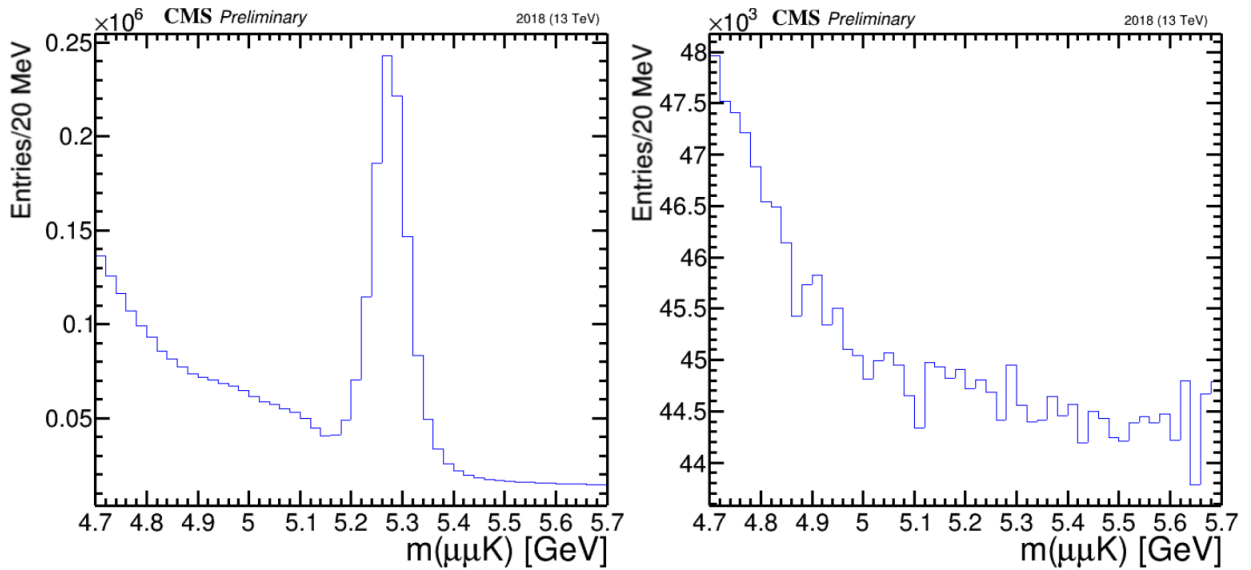


Figure 50: Mass distribution for the two dimuon mass regions, resonant (left) and rare (right), for tag candidates passing only the preselection cuts. As we can see the peak for the rare mode is not optimal.

Hence, we need to require extra cuts associated with the kinematics, and we need to maximize the signal "significance", for example something like $S/\sqrt{S+B}$. As for the B, we do not really care where does it come from, whether it's random combinatorics or partially reconstructed background. It's just background that must be limited.

In general, if someone wants to maximize the signal significance, defined as $S/\sqrt{S+B}$, for each channel, then different different optimizations are required. For example, in general

we need four different optimization one for the resonant mode in the tag side, one for the resonant mode in the probe side, one for the non-resonant in tag side and one for the non-resonant in tag probe side. The reason is that we want the maximum number of events for numerator and denominator, in forming the $R_K(\mu)$ fraction. On the other hand, the use of different cuts for non-resonant and resonant modes increases the systematics. If on the other hand we use a cut that maximizes the non-resonant events, where we have fewer candidates, we will be suboptimal for the resonant ones.

In the case of the muons the statistics is so high, that we have a huge number of resonant decays anyway, so even with a bit of inefficiency with respect to the "optimal", everything will be fine. In the muons the systematics are a bigger enemy than the statistics. So we should keep the same cuts for resonant and non-resonant modes, but still we need two optimizations, one for tag and one for probe side since the kinematics are different for the two sides. Hence, the optimization is made to maximize the significance $S/\sqrt{(S+B)}$ for the rare mode.

One possible method to maximize the significance is to apply global cuts for all candidates, for example to keep all candidates with $|L_{xy}|/\sigma(L_{xy})$ greater than a specific value, where the values can be calculated by comparing signal and background distributions. Instead of optimizing the cuts using this method we will use Boosted Decision Trees.

A decision tree takes a set of input features and splits input data recursively based on those features. Each split at a node is chosen to maximize information gain. The splits are created recursively. This process is repeated until some stop condition is met, for example the depth of tree or no more information gain. By the end of a decision tree, the initial volume of data has been separated in subareas, and each subarea is characterized as signal or background according to the majority of candidates. Boosting expands this process by combining many weak learners (trees) into a strong classifier. Each tree is trained every time by the same amount of data, but each time with different weights. To identify a candidate as signal or as background, the results from all trees are considered. Boosting can increase the learning efficiency. However, the unlimited usage of trees can not lead to an unlimited improvement of the process. The more used trees, the less they contribute to the process. Hence, the first trees are usually those that are dominant and the latter have less and less impact on the learning process. Furthermore, more trees demand more CPU.

The eXtreme Gradient Boosting is a machine learning technique for regression and classification problems, which produces a prediction model in the form of an ensemble of weak prediction models, typically decision trees. When a decision tree is the weak learner, the resulting algorithm is called gradient boosted trees, which usually outperforms random forest. It builds the model in a stage-wise fashion like other boosting methods do, and it generalizes them by allowing optimization of an arbitrary differentiable loss function. It is easiest to explain in the least-squares regression setting, where the goal is to "teach" a model F to predict values of the form $\hat{y} = F(x)$ by minimizing the mean squared error $\frac{1}{n} \sum_i (\hat{y}_i - y_i)^2$, where i indexes over some training set of size n of actual values of the output variable y , where \hat{y}_i is the predicted value $F(x)$, y_i is the observed value and n is the number of samples in y .

In our case, the complete set of algorithms for BDT studies have been written and tested by Georgios Karathanasis. The idea is to train the XGB framework using background events from data and signal events from MC samples and especially $B \rightarrow \mu\mu K$ events.

As discussed previously, we need to maximize the significance for the rare mode. Therefore we need to specify the background and the signal regions. Signal region, is defined by MC events, and to be more accurate, signal region is reconstructed candidates with $m(\mu\mu)$ in the low q^2 region. Background events are defined, using data, are defined as candidates in the same dimuon mass spectrum region but with $(\mu\mu K)$ mass in the two sideband regions, [4.9,5.1] and [5.4,5.65] GeV.

To train the BDT, we use the following parameters: $Prob(SV)$, L_{xy}/σ , $\cos\alpha(2D_{xy}) > 0$, $P_T(\mu_1, \mu_2, K) > 3$ GeV, $Iso(\mu_1)$, $\Delta z(\mu, K)$, $\Delta R(\mu, K)$. According to these parameters, BDT will connect each B candidate with a value, which is called BDT output or xgb value. The plot for this value is shown in figure (51). According to this plot the BDT cut is applied.

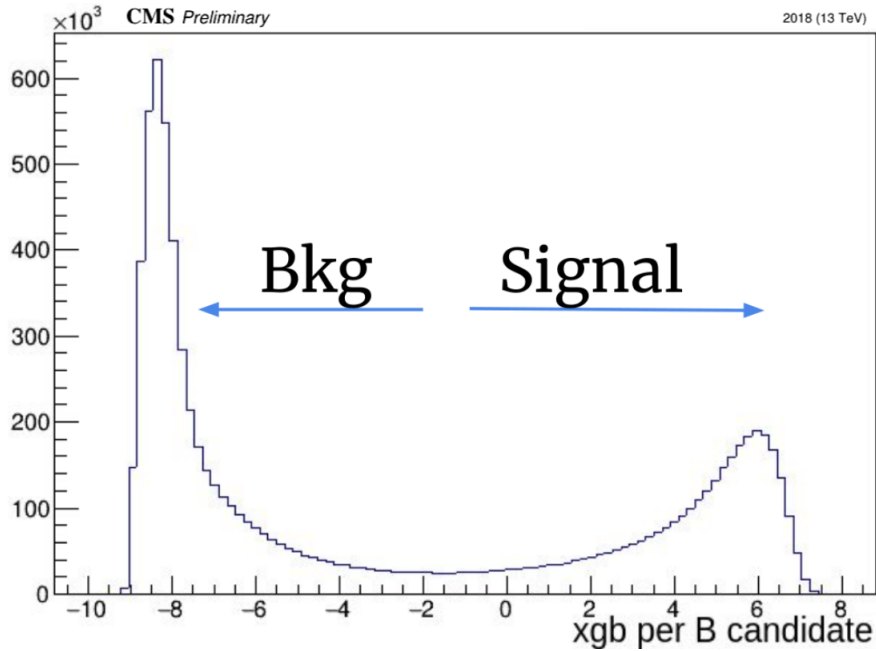


Figure 51: xgb value per B candidate.

But how do we choose the BDT cut? Let's focus for a while in figure (51). As we can see, BDT classifies candidates in two region according two their xgb value. The higher a candidate is rated, the higher the possibility the candidate to be a real candidate. However, a real candidate may be rated with a lower xgb value and, hence, may be rejected by the BDT cut. Therefore we need to calculated the BDT-cut efficiency. As we mentioned, we need to cut to a BDT value to maximiza the significance. So, to begin with we keep a specific q^2 region and then we keep all candidates above a xgb value. For example, let's work with the resonant mode ($2.9 < m(\mu\mu) < 3.2$) GeV) and keep all candidates with xgb value > -4 and plot their mass. The plot looks like those in (4.7). Then we fit the distribution

as discussed in the same section. If we integrate the sum of the two gaussian in the peak region, we measure the signal candidates. Then, if we integrate the exponential function for the background we measure the background candidates. For the integrals, we use the σ of the narrow gaussian. Therefore we can calculate the significance for this xgb cut. Having measured the significance we change the BDT cut and we repeat again the same process. This process is repeated until we found the maximum significance as shown in figure (52)

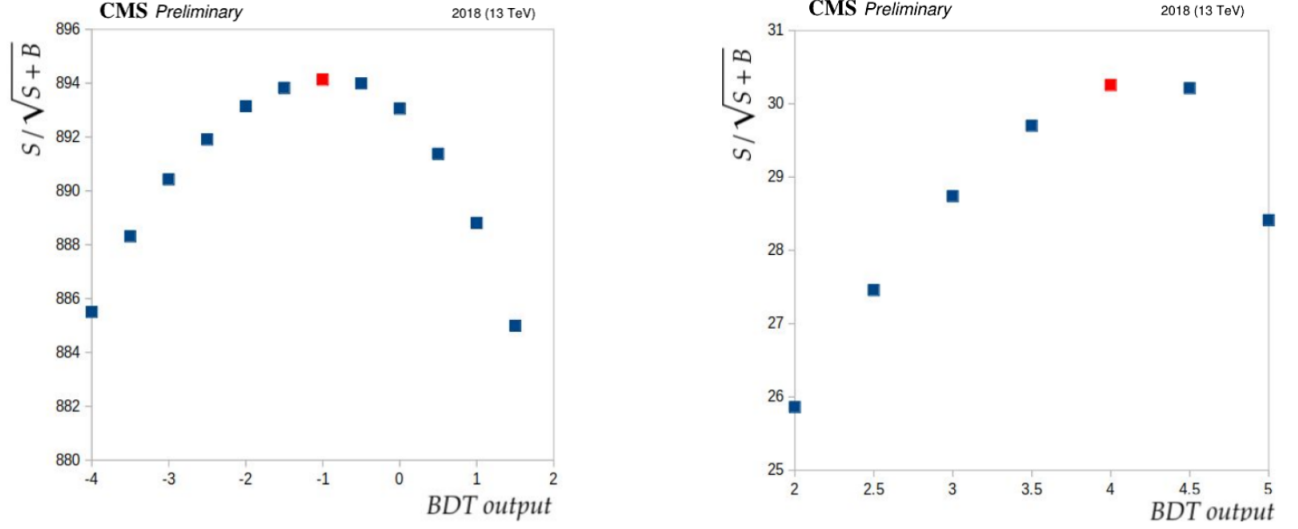


Figure 52: Scan BDT output for maximum significance in $2.9 < m(\mu\mu) < 3.2$ GeV (left) and in $m(\mu\mu) < 2.5$ GeV region.

Therefore, the working points are at BDT output=-1 for the resonant channel and at BDT output=4 for the rare channel. Now, using MC samples we can calculate the efficiency of the BDT cut. In table (11) the BDT cut efficiencies are listed for the two working points. In figure (53) the xgb values for the two MC samples.

Table 11: BDT efficiency for the The total $(\alpha \times \varepsilon)_{trg}$ factor for the two decays.

Channel	ε_{BDT}
$B^+ \rightarrow J/\psi(\mu^- \mu^+) K^+$	97.56 ± 0.25
$B^+ \rightarrow \mu^- \mu^+ K^+$	79.39 ± 0.75
ratio	4.62 ± 0.03

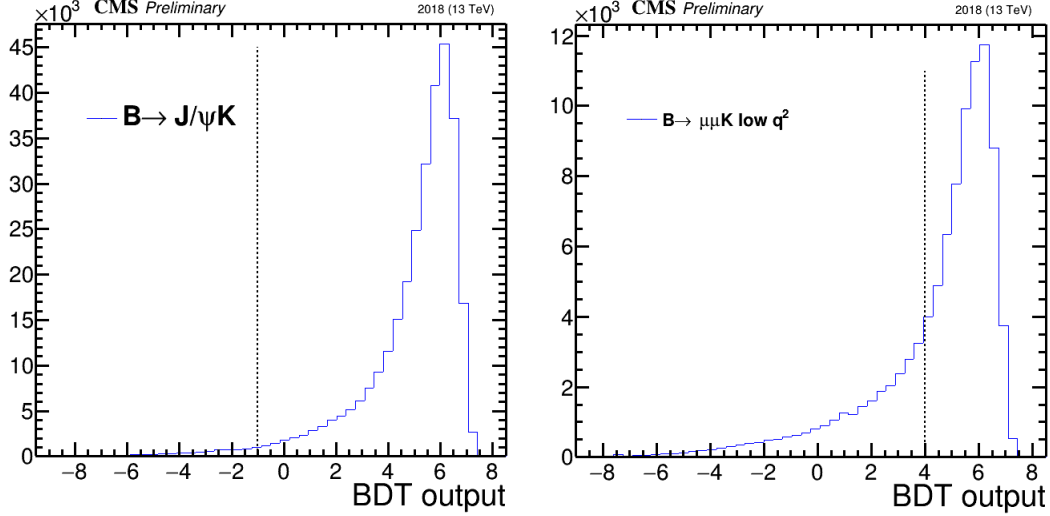


Figure 53: BDT output per B candidate for the two decay modes using MC samples.

4.7 Fitting Processes

Therefore, we can now apply the BDT cut. The distributions having applied the two BDT cuts for the two different dimuon mass regions are shown in figures (54) (resonant mode) and (55) (rare mode).

Let's focus for a while in the resonant mode, figure (54). As we see, the peak from this decay mode is sharp and clear, as expected since the muons are efficiently reconstructed and the branching ratio for this decay, according to PDG 2020, is

$$Br(B \rightarrow J/\psi K, J/\psi \rightarrow \mu\mu) = (1.006 \pm 0.027) \cdot 10^{-3} \times (0.0593 \pm 0.0006) = (5.97 \pm 0.17) \cdot 10^{-5}.$$

However, we see that there is a significant amount of background events. The most interesting part, is the small doubly bumpy area, extended in $[4.8, 5.15]$ GeV. Furthermore, if we look more carefully we will see that this area is not a simple bump, but actually two bumps with a bit different means. Indeed, these bumps are created by $B^0 \rightarrow K^* J/\psi, J/\psi \rightarrow \mu\mu, K^+ \rightarrow K\pi$ decays¹³. In these decays, the K^* decays to a charge kaon and an opposite charged pion. In our analysis, we reconstruct a vertex from two muons and a single track. Thus, half times we reconstruct the pion, and half times we reconstruct the kaon from these decays, but always we reconstruct these tracks as kaons, since we make the hypothesis that all tracks are kaons with $m=493.677$ MeV. When the pion is missing, we are losing ~ 140 MeV, and hence the bump with mean ~ 5.1 is created and when the pion is missing we are losing 500 MeV. However, in this case we give extra mass to the real pions, shifting their bump to higher values and close to 4.95 GeV. These cases, where we are missing at least one decay product, belong to the so-called partially reconstructed background. For these two bumps, two different gaussians, whose parameters have been calculated by MC samples, are used.

¹³B, K^* and J/ψ are neutral particles, while muons are opposite charged as the kaon-pion pair

For the peak region, two gaussians, a narrow and a wide gaussian are used. We are using two different gaussians, since muons are reconstructed by different muon chambers and hence, their resolution is a bit different creating two tangled gaussians.

As for the background, the upper side band is dominated by random combinatorics¹⁴. On the other hand, the lower side band has both random combinatorics and partially reconstructed B decays. The two contributions are separated by extending the exponential that describes the combinatorics of the upper sideband.

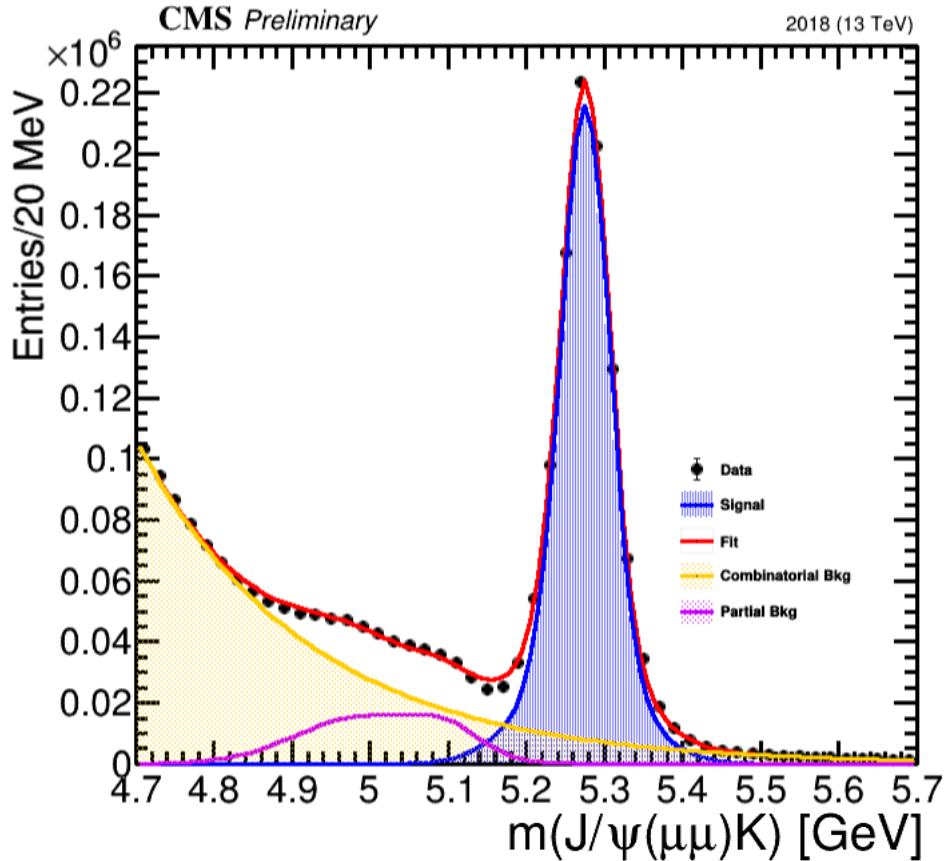


Figure 54: Invariant mass distribution of $J/\psi K^\pm$.

As for the integration, the sum of the two gaussians is integrated in the whole spectrum. Therefore

¹⁴However, this assumption is not correct, since according to the Kaon mass hypothesis and the lack of particle identification, pions from $B \rightarrow J/\psi\pi, J/\psi \rightarrow \mu\mu$ decays are creating signal events contaminating both the combinatorics fit component and the signal fit component. But, due to Cabibbo suppression the branching ratio for pion modes are 4% of the kaon modes.

Table 12: Reconstructed candidates for the resonant mode using the whole b-Parking dataset.

Channel	N_{data}
$B^+ \rightarrow J/\psi(\mu^- \mu^+)K^+$	983010 ± 1113

In table (13) the fit parameters are listed.

Table 13: Fit Parameters for the resonant mode. The First three parameters (0,1,2) are the amplitude, the mean and the σ of the narrow gaussian. The next three (3,4,5) are the same parameters for the wide gaussias. The following two parameteres (6,7) are the two parameters for the exponential component in the upper sideband. The following six parameters (8,9,10,11,12,13) are the amplitude, the mean and the σ for the two gaussians that describe the partially reconstructed background.

Parameter	Value
p ₀	$1.82020e+05 \pm 3.60882e+02$
p ₁	$5.27574e+00 \pm 6.20468e-05$
p ₂	$3.05363e-02 \pm 1.36928e-04$
p ₃	$3.41341e+04 \pm 1.82641e+02$
p ₄	$5.26782e+00 \pm 2.82478e-04$
p ₅	$6.69438e-02 \pm 6.15505e-04$
p ₆	$3.27158e+01 \pm 3.51719e-02$
p ₇	$-4.49881e+00 \pm 7.31703e-03$
p ₈	$7.27418e+03 \pm 1.13079e+02$
p ₉	$5.09931e+00 \pm 1.66001e-03$
p ₁₀	$4.11327e-02 \pm 2.20843e-03$
p ₁₁	$1.55525e+04 \pm 1.09271e+02$
p ₁₂	$4.99257e+00 \pm 4.80028e-03$
p ₁₃	$8.63803e-02 \pm 2.28013e-03$

For the rare mode, we are using again two gaussians for the peak region and again we are using again an exponential for the upper side band. However, this time, the partially reconstructed background is not visible as the one shown in figure (54). This time the partially reconstructed background is created again by $B \rightarrow K^* \mu \mu$ and by a "leakage" from the J/ψ mode. In figure (55), the mass spectrum for the $(\mu \mu K)$ candidates using low q^2 region. In table (15), the fit parameters are listed with their error values.

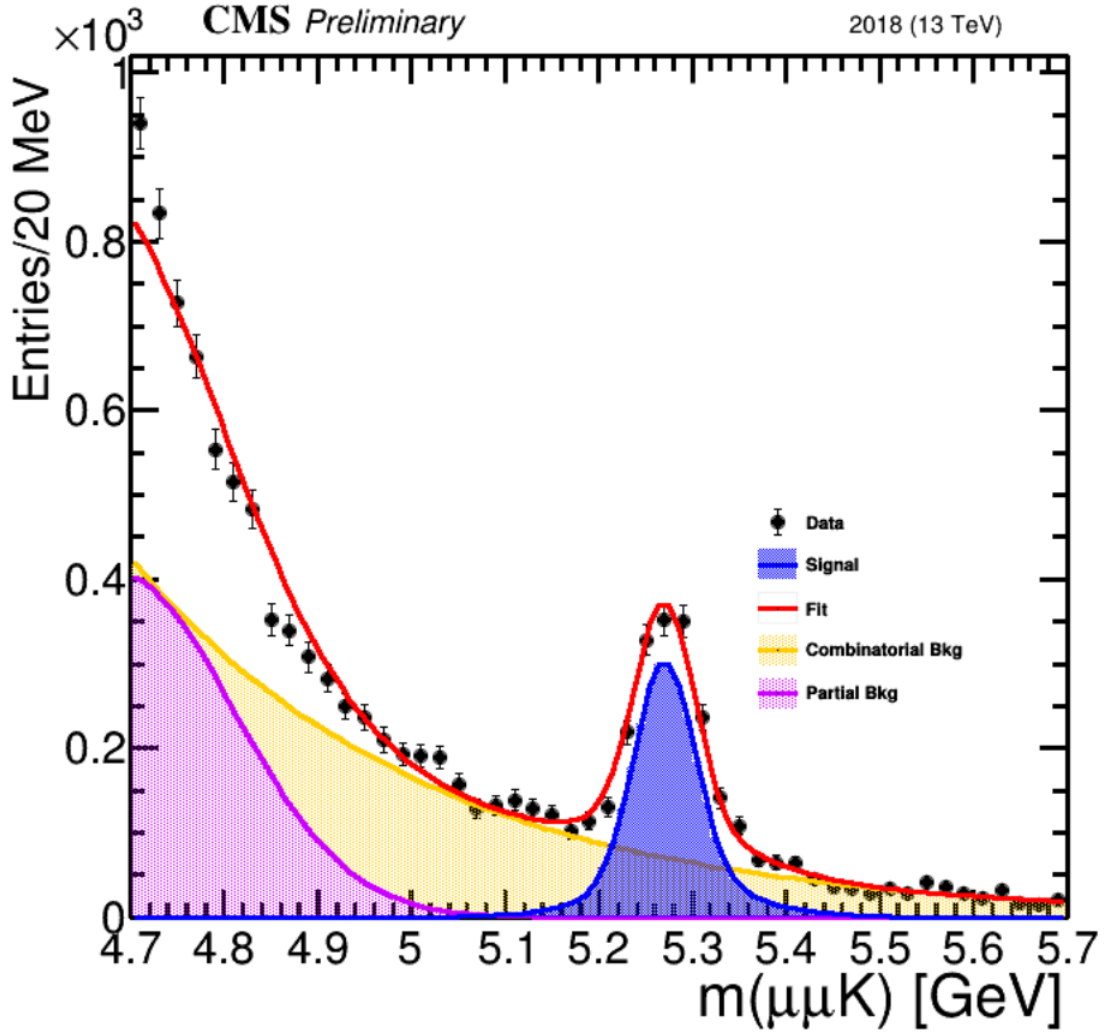


Figure 55

As for the integration, the sum of the two gaussians is integrated in the whole spectrum. Therefore

Table 14: Reconstructed candidates for the rare mode using the whole b-Parking dataset.

Channel	N_{data}
$B^+ \rightarrow \mu^- \mu^+ K^+$	1449 ± 50

Table 15: Fit Parameters for the rare mode. The First three parameters (0,1,2) are the amplitude, the mean and the σ of the narrow gaussian. The next three (3,4,5) are the same parameters for the wide gaussians. The following two parameters (6,7) are the two parameters for the exponential component in the upper sideband. The following six parameters (8,9,10,11,12,13) are the amplitude, the mean and the σ for the two gaussians that describe the partially reconstructed background.

Parameter	Value
p ₀	2.65445e+02 ± 1.54337e+01
p ₁	5.27022e+00 ± 2.87368e-03
p ₂	3.22489e-02 ± 5.20230e-04
p ₃	3.72529e+01 ± 9.82676e+00
p ₄	5.28136e+00 ± 1.16712e-02
p ₅	8.06440e-02 ± 2.51127e-03
p ₆	2.08502e+01 ± 1.56458e+00
p ₇	-3.14842e+00 ± 3.03586e-01
p ₈	2.22045e-10 ± 1.49984e+00
p ₉	4.85717e+00 ± 5.18369e-03
p ₁₀	1.19204e-01 ± 4.19758e-03
p ₁₁	4.07495e+02 ± 5.85781e+01
p ₁₂	4.68524e+00 ± 3.95438e-03
p ₁₃	1.23963e-01 ± 1.62441e-03

4.8 Scale Factor

As mentioned in the previous sections, the two decays we are working on, are separated in data according to the mass of the two muons, and hence each candidate with mass in the low q^2 is considered to be a candidate for the rare mode and all candidates with dimuon mass in the region [2.9,3.2] GeV are considered to be candidates for the resonant mode. However, as mention in (4.3), the mass spectrum from the rare non-resonant channel is extended from 0.2 up to 4.8 GeV, and thus, the this mode contaminates the resonant mode.

To subtract this contamination we are using the MC. We reconstruct the B candidate up to step where we cut on the dimuon mass region. The reconstructed spectrum for the rare mode is shown in figure (56).

We suppose that the shape of this spectrum (at reconstructed level of the MC sample) is the same with the reconstructed spectrum in data, which means that if we somehow could reconstruct only these decays in data, the reconstructed spectrum for the dimuon system would look like this. Now, we suppose that the ratio of the candidates belonging to the J/ψ resonance over the number of candidates belonging to the low q^2 and come from the MC, is equal to the same ratio using candidates that are reconstructed in data, namely

$$\frac{N_{data;rare \rightarrow J/\psi}}{N_{data;rare \rightarrow lowq^2}} = \frac{N_{MC;rare \rightarrow J/\psi}}{N_{MC;rare \rightarrow lowq^2}} \quad (4.1)$$

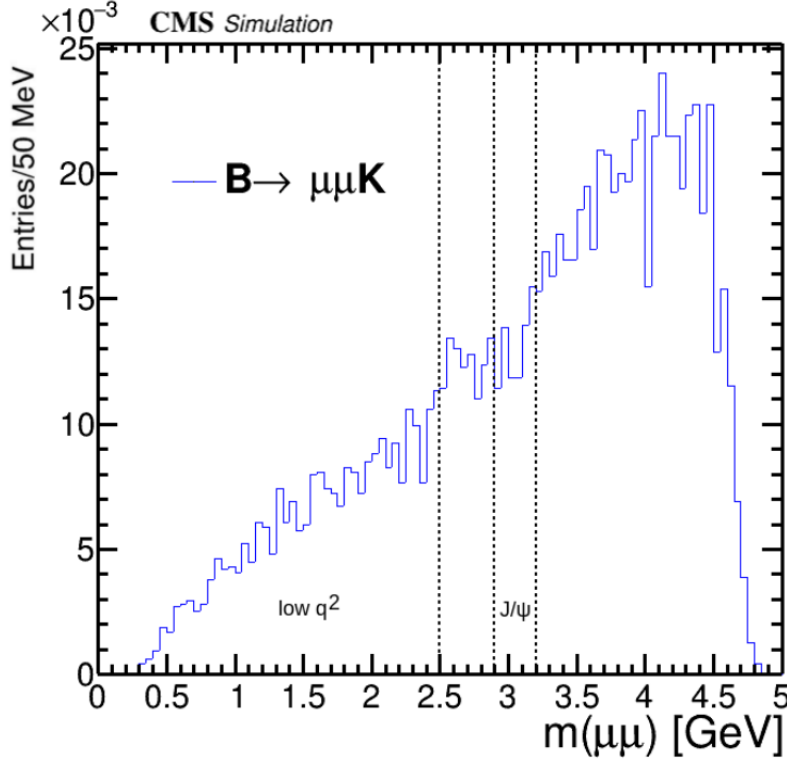


Figure 56: Reconstructed dimuon mass spectrum using MC samples for the rare $B \rightarrow \mu\mu K$ decay.

According to this MC sample, in the low q^2 region there are 24394 candidate, while in the J/ψ region there are 7327 candidates.

Now, the only unknown value is number of candidates from the rare mode that have dimuon mass in the J/ψ region, $N_{data;rare \rightarrow J/\psi}$,

$$N_{data;rare \rightarrow J/\psi} = N_{data;rare \rightarrow lowq^2} \times \frac{N_{MC;rare \rightarrow J/\psi}}{N_{MC;rare \rightarrow lowq^2}} = 1449 \times \frac{11946}{2294} \Rightarrow N_{data;rare \rightarrow J/\psi} = 433 \quad (4.2)$$

Therefore, we need to subtract 433 candidates from the total 983010 candidates that have been reconstructed for the resonant mode.

4.9 $R_K(\mu)$ measurement

Everything has been measured, and thus we can return to the (3.66) formula, to replace the ratios and to measure the $R_K(\mu)$ fraction.

$$R_K(\mu) = \left(\frac{N(B \rightarrow K\mu\mu)_{data}}{N(B \rightarrow KJ/\psi(\mu\mu))_{data}} \right) \times \left(\frac{(\alpha \times \varepsilon)_{B \rightarrow KJ/\psi(\mu\mu)}}{(\alpha \times \varepsilon)_{B \rightarrow K\mu\mu}} \right) =$$

$$\begin{aligned}
&= \frac{N(B \rightarrow K\mu\mu)_{data}}{N(B \rightarrow KJ/\psi(\mu\mu))_{data}} \times \frac{(\alpha \times \varepsilon)_{trg, B \rightarrow KJ/\psi(\mu\mu)}}{(\alpha \times \varepsilon)_{trg, B \rightarrow K\mu\mu}} \times \frac{(\alpha \times \varepsilon)_{B, B \rightarrow KJ/\psi(\mu\mu)}}{(\alpha \times \varepsilon)_{B, B \rightarrow K\mu\mu}} \times \\
&\quad \times \frac{\varepsilon(m_{\mu\mu})_{B \rightarrow KJ/\psi(\mu\mu)}}{(\varepsilon(m_{\mu\mu}))_{B \rightarrow K\mu\mu}} \times \frac{\varepsilon(BDT)_{B \rightarrow KJ/\psi(\mu\mu)}}{(\varepsilon(BDT))_{B \rightarrow K\mu\mu}} = \\
&= (1.475 \pm 0.051) \times 10^{-3} \times (0.9533 \pm 0.0031) \times (0.9457 \pm 0.0041) \times (4.626 \pm 0.032) \times (1.229 \pm 0.012) \Rightarrow \\
&\quad \Rightarrow R_K(\mu) = (7.560_{\pm 0.099(MC)}^{\pm 0.26(Data)}) 10^{-3} \tag{4.3}
\end{aligned}$$

where the upper error bar is estimated using only the Data statistics and the lower error bar is estimated using the MC statistics. According to PDG 2020 this ratio is measured as

$$R_K(\mu)(PDG) = (7.280 \pm 0.45) \times 10^{-3} \tag{4.4}$$

4.10 $R_{\psi(2S)}(\mu)$ measurement

To validate our method, we will measure one more branching fraction. In addition to $B \rightarrow J/\psi K$ decays, clear signals are observed from $B \rightarrow J\psi(2S)K$ decays. The double ratio of branching fractions, $R_{\psi(2S)}$, defined by (3.67) provides a cross check and an independent validation of the double-ratio analysis. This cross check is necessary since the systematics are not measured for the purposes of this thesis. Thus, we need to redo the whole process for the $B \rightarrow K\psi(2S)(\mu\mu)$

However, for the $B \rightarrow \psi(2S)K$ mode there are not official-filtered samples. Therefore, to measure the $\alpha \times \varepsilon$ ratios for the new fraction we will use only the unbiased samples¹⁵. We will focus for a while only in the $\alpha(P_T)$ factors, which are those with the most interest.

As mentioned in (44), the acceptance increases with the dimuon mass, which is expected since, higher invariant masses can produce more energetic decay products, and thus, more muons are now passing the P_T thresholds, and thus, these acceptance factors are higher than those of the J/ψ mode.

In figure (57), the distributions at generation level for the $B \rightarrow \psi(2S)(\mu\mu)K$ mode are shown, superimposed with those of the $B \rightarrow J/\psi(2S)(\mu\mu)K$. As we can see the distribution are in agreement (since these distributions are associated with the production kinematics of the B meson) and therefore there is no need for the ratio plots.

¹⁵Those with $P_T(b(\text{Hat})) > 9$ GeV

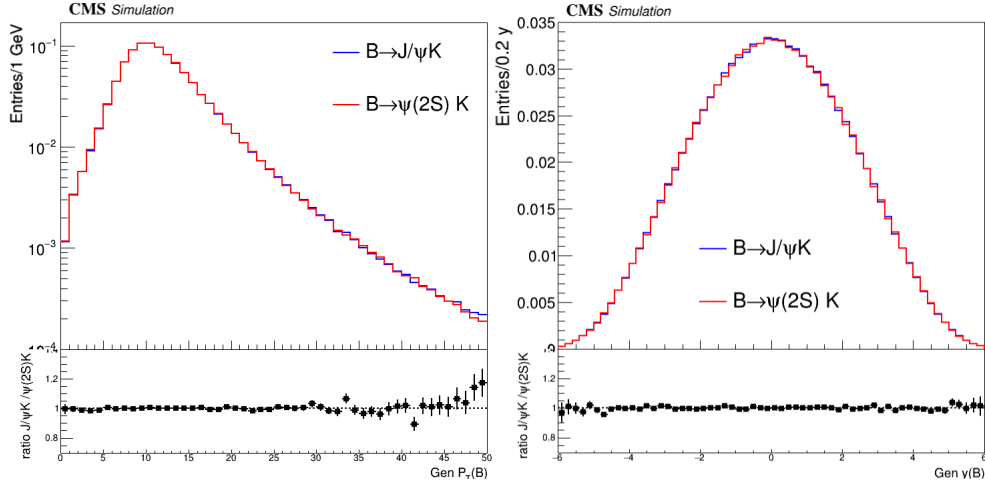


Figure 57: The $P_T(B^+)$ and $y(B^+)$ spectra at generation level for the two resonant modes. As we can see the spectra for the two decay modes are almost identical, which reflects again the fact that this spectra are associated with the production mechanism of the B^+ meson and not with the decay mechanism.

However, in figures (58) and (59), we see that this time the ratio behavior is a bit more "suppressive" since the plateau is at lower value comparing it with the ratio plots in figures (4),(45). The reason is the fact that acceptance is increasing with the dimuon mass and since the dimuon mass is higher for the $\psi(2S)$ mode, muons are now expected to be more energetic.

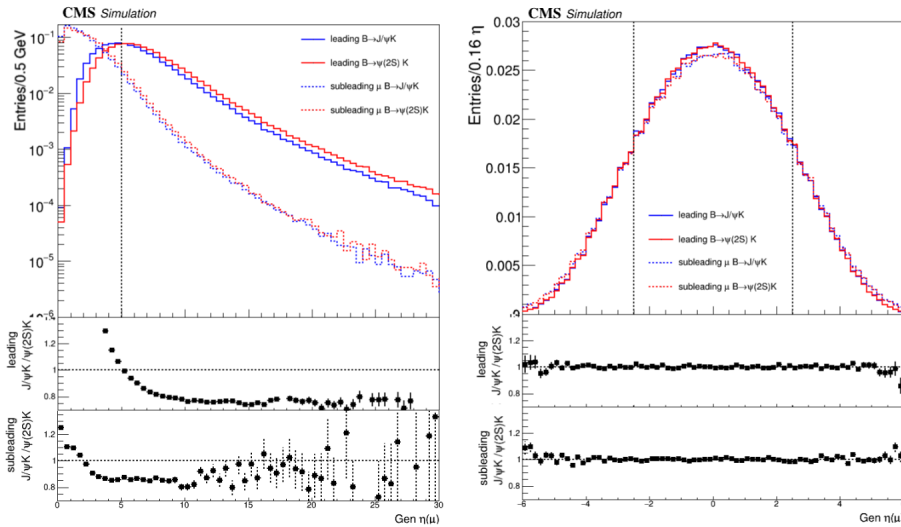


Figure 58: The leading and subleading $P_T(\mu)$ (left) and $\eta(\mu)$ (right) spectra at generation level for the $B \rightarrow J\psi(2S)(\mu\mu)K$ and $B \rightarrow J\psi(\mu\mu)K$ modes. As we can see, the P_T spectrum for the J/ψ mode is suppressed with respect to the $\psi(2S)$ mode. As mentioned, this effect is due to the fact that the acceptance increases with the dimuon mass.

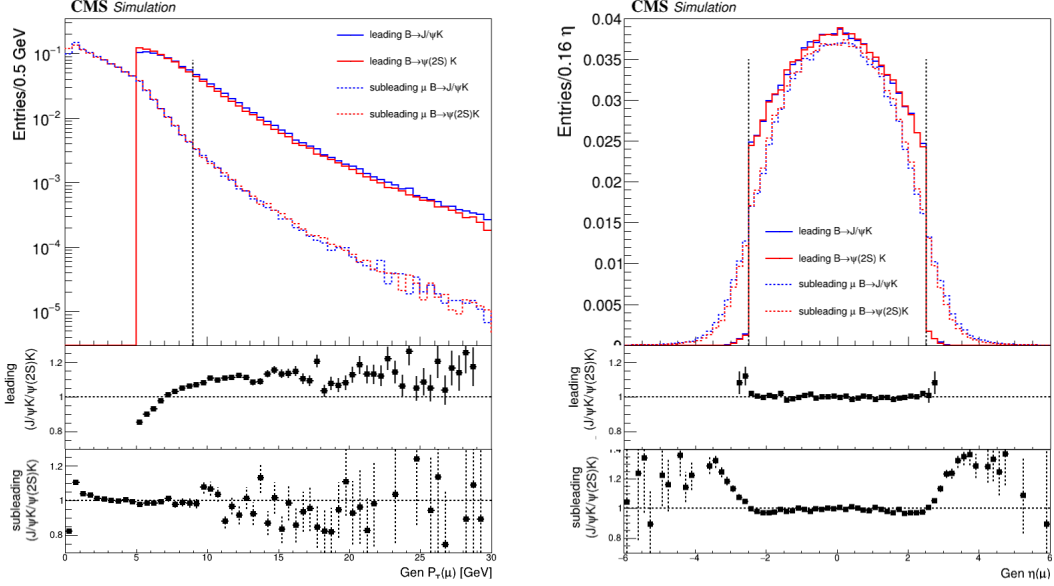


Figure 59: Spectra at generation level for muons passing the filter requirements for leading and subleading μ for the two decays. This spectra have been plotted using MC samples with $P_T(\text{hat}) > 9 \text{ GeV}$ only. As we can see, the P_T spectrum for the J/ψ mode is again suppressed with respect to the $\psi(2S)$ mode.

In table (16), the $\alpha \times \varepsilon$ ratios for the J/ψ mode and the $\psi(2S)$ modes are listed.

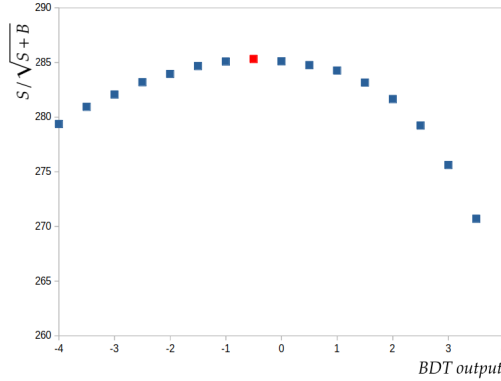


Figure 60: Scan BDT output for maximum significance in $3.4 < m(\mu\mu) < 4 \text{ GeV}$ mass region.

Therefore, after all these, the reconstructed mass spectrum for the $\psi(2S)$ mode is shown in figure (61). For the fit, a double gaussian is used again for the signal region (one narrow and one wide). For the combinatorial background, an exponential is used in the upside band. As for the partially reconstructed background, a single gaussian is used, since this time the double bump shape is not so much visible as previous, however this does not mean that the K^* source of background does not exist now. Furthermore each attempt to use a double gaussian for this case failed. The fit parameters are listed in table (17)

Table 16: Ratios of acceptance and efficiency factors for the two decays.

Channel	ratio ($B^+ \rightarrow J/\psi K^+$)/ $B^+ \rightarrow \psi(2S)K^+$
α_{filter}	0.8482 ± 0.0017
$\alpha(\eta < 1.5)$	1.0011 ± 0.0027
$\alpha(P_T > 9GeV)$	0.9075 ± 0.0039
α_{trg}	0.7705 ± 0.0036
ε_{reco}	0.9988 ± 0.0054
ε_{cuts}	1.0124 ± 0.0081
ε_{HLT}	1.002 ± 0.010
ε_{total}	1.014 ± 0.0082
$(\alpha \times \varepsilon)_{trg}$	0.7811 ± 0.0057
$\alpha(\mu_2, K)$	0.965 ± 0.012
$\varepsilon_{reco} \times \varepsilon_{presel}$	1.015 ± 0.015
$(\alpha \times \varepsilon)_B$	0.979 ± 0.014
$\varepsilon(m_{\mu\mu})$	1.005 ± 0.016
ε_{BDT}	0.992 ± 0.017

Table 17: Fit Parameters for the rare mode. The First three parameters (0,1,2) are the amplitude, the mean and the σ of the narrow gaussian. The next three (3,4,5) are the same parameters for the wide gaussians. The following two parameteres (6,7) are the two parameters for the exponential component in the upper sideband. The following six parameters (8,9,10,11,12,13) are the amplitude, the mean and the σ for the two gaussians that describe the partially reconstructed background.

Parameter	Value
p ₀	$1.64962e+03 \pm 4.15400e+01$
p ₁	$5.05785e+00 \pm 1.50569e-03$
p ₂	$5.32764e-02 \pm 1.64387e-03$
p ₃	$6.82850e+03 \pm 6.56522e+02$
p ₄	$5.27663e+00 \pm 5.57579e-04$
p ₅	$5.18432e-02 \pm 1.35996e-03$
p ₆	$1.59928e+04 \pm 6.16005e+02$
p ₇	$5.27487e+00 \pm 2.57754e-04$
p ₈	$2.76857e-02 \pm 6.06367e-04$
p ₉	$2.99567e+01 \pm 9.40297e-02$
p ₁₀	$-4.33365e+00 \pm 1.94894e-02$

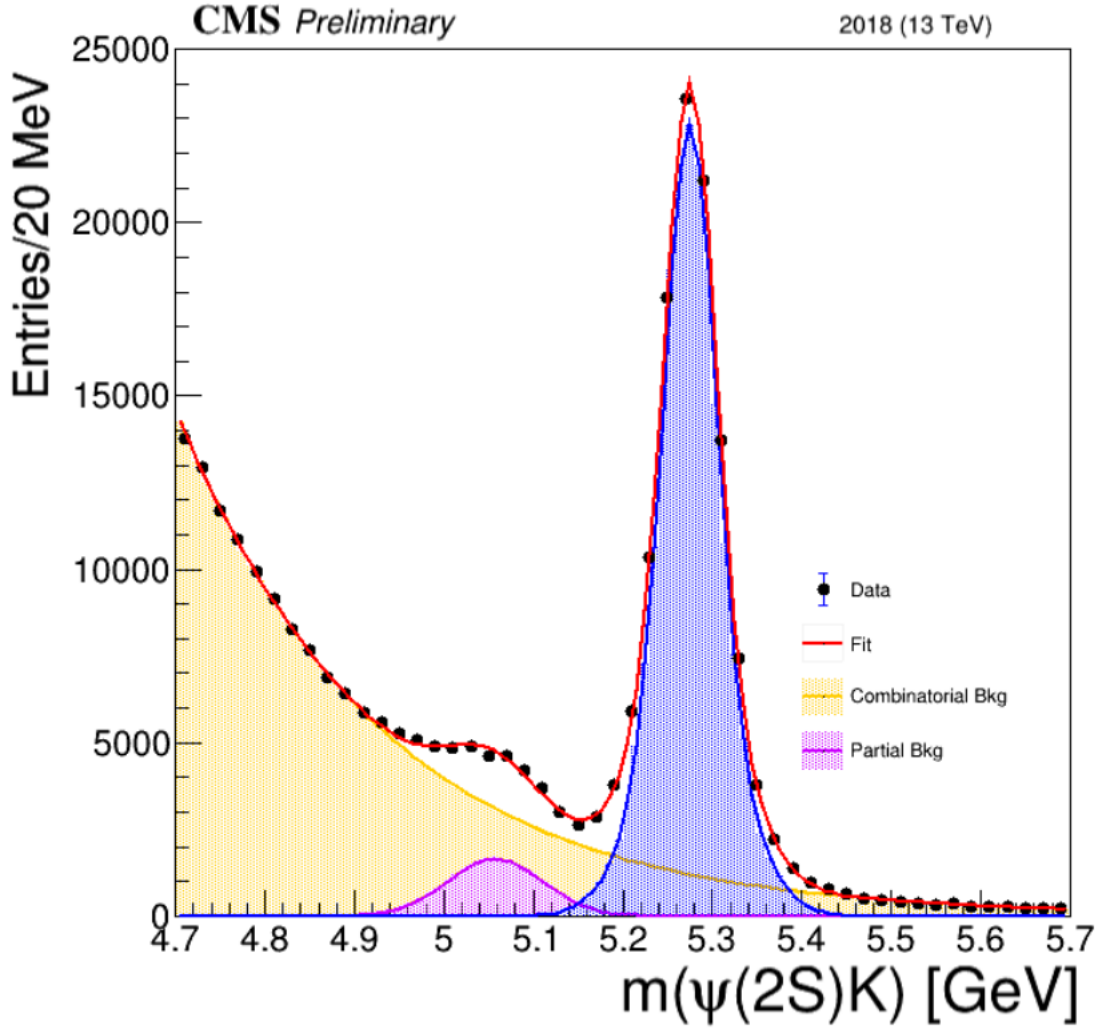


Figure 61

Table 18: Reconstructed candidates for the $\psi(2S)$ mode using the whole b-Parking dataset.

Channel	N_{data}
$B \rightarrow \psi(2S)(\mu\mu)K$	99862 ± 349

Again, as mentioned in the previous sections, there is not only overlap in the dimuon mass spectrum between the rare mode and the J/ψ mode, but also between the rare mode and the $\psi(2S)$ mode. Thus, again, we can not keep all candidates reconstructed with dimuon mass in $[3.4, 4]$ GeV region. To subtract this contamination we will calculate again a scale factor as in (4.1).

$$\frac{N_{data;rare\rightarrow\psi(2S)}}{N_{data;rare\rightarrow lowq^2}} = \frac{N_{MC;rare\rightarrow\psi(2S)}}{N_{MC;rare\rightarrow lowq^2}} \quad (4.5)$$

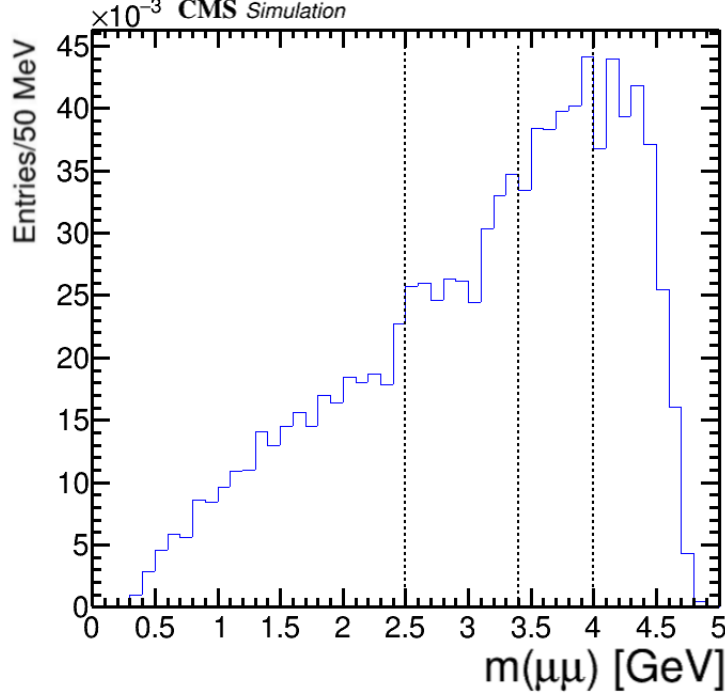


Figure 62: Reconstructed dimuon mass spectrum using MC samples for the rare $B \rightarrow \mu\mu K$ decay.

$$N_{data;rare\rightarrow\psi(2S)} = N_{data;rare\rightarrow lowq^2} \times \frac{N_{MC;rare\rightarrow\psi(2S)}}{N_{MC;rare\rightarrow lowq^2}} = 1449 \times \frac{21103}{24271} \Rightarrow N_{data;rare\rightarrow\psi(2S)} = 1250 \quad (4.6)$$

Therefore, we need to subtract 1250 candidates from the total 99862 candidates that have been reconstructed for the $\psi(2S)$ mode.

Now, lets go back in (3.67) and replace all the MC ratios according to table (16).

$$\begin{aligned} R_{\psi(2S)}(\mu) &= \left(\frac{N(B \rightarrow K\psi(2S)(\mu\mu))_{data}}{N(B \rightarrow KJ/\psi(\mu\mu))_{data}} \right) \times \left(\frac{(\alpha \times \varepsilon)_{B \rightarrow KJ/\psi(\mu\mu)}}{(\alpha \times \varepsilon)_{B \rightarrow K\psi(2S)(\mu\mu)}} \right) = \\ &= \frac{N(B \rightarrow K\psi(2S)(\mu\mu))_{data}}{N(B \rightarrow KJ/\psi(\mu\mu))_{data}} \times \frac{(\alpha \times \varepsilon)_{trg,B \rightarrow KJ/\psi(\mu\mu)}}{(\alpha \times \varepsilon)_{trg,B \rightarrow K\psi(2S)(\mu\mu)}} \times \frac{(\alpha \times \varepsilon)_{B,B \rightarrow KJ/\psi(\mu\mu)}}{(\alpha \times \varepsilon)_{B,B \rightarrow K\psi(2S)(\mu\mu)}} \times \\ &\quad \times \frac{\varepsilon(m_{\mu\mu})_{B \rightarrow KJ/\psi(\mu\mu)}}{(\varepsilon(m_{\mu\mu})_{B \rightarrow K\psi(2S)(\mu\mu)}} \times \frac{\varepsilon(BDT)_{B \rightarrow KJ/\psi(\mu\mu)}}{(\varepsilon(BDT)_{B \rightarrow \psi(2S)(\mu\mu)}} = \\ &\Rightarrow R_{\psi(2S)}(\mu) = (75.46_{\pm 2.14(MC)}^{\pm 0.28(Data)}) 10^{-3} \quad (4.7) \end{aligned}$$

where the upper error bar is estimated using only the Data statistics and the lower error bar is estimated using the MC statistics. According to PDG 2020 this ratio is measured as

$$R_{\psi(2S)}(\mu)(PDG) = (82.9 \pm 7.2) \times 10^{-3} \quad (4.8)$$

5 Summary and Outlook

In this Master's Thesis, the basic characteristic of the CMS detector was presented in Chapter 1, while in the second chapter the "Event Reconstruction" was discussed. For further details, someone could use the references along the text. In the third chapter, the basic theory for the electroweak unification was discussed. In this chapter the theory describing the rare and the resonant mode was outlined. However, the detailed calculations for these decays and the analytical proof for the branching fraction are far beyond the purposes of this thesis.

In the fourth chapter, all the parts that are associated with the muon reconstruction and the $R_K(\mu)$ fraction were discussed. Furthermore, we managed to measure the $R_K(\mu)$ fraction, without measuring the systematic error bars. To validate the method, which seems to work, we also measured the $R_{\psi(2S)}$ fraction. Both fraction are in agreement with PDG values in the uncertainty of $\sim 1\sigma$. But, we should keep in mind that all these results are preliminary.

During the last weeks, we have found a few problems with the MC samples. All private MC samples that have been used to measure the filter acceptances and the $\psi(2S)$ mode have been produced with Hard QCD settings for the Pythia generator and further studies showed that hard QCD spectra are inefficient with respect to the Official Soft QCD samples. We also know, that the official samples, were not initially produced to be used in the tag side. The existence of a third muon may contaminate the samples with bias.

As for the systematics, they are expected to cancel out to first order, due to the ratios. The main source of systematics are expected due to the different BDT cuts and the different acceptance factors. Since a muon is accepted, it is not expected to behave with a different way depending on its mother and the decay mode. Therefore, reconstruction efficiencies for the two decays are not expected, and indeed they are not different, and the systematic uncertainties for this factors are now expected to play a significant role.

Finally, I would like to thank Georgios Karathanasis for his help, all my friends and my family for their unlimited support and Pr. Sphicas Paraskevas for his trust, his advices, his guidance and the opportunities he offered me.

References

- [1] Roel Aaij, LHCb Collaboration, et al. Test of lepton universality using $b^+ \rightarrow k^+l^+l^-$ decays. *Phys. Rev. Lett*, 113(151601):6, 2014.
- [2] T Affolder, H Akimoto, A Akopian, MG Albrow, P Amaral, SR Amendolia, D Amidei, J Antos, G Apollinari, T Arisawa, et al. Measurement of b-quark fragmentation fractions in $p p^-$ collisions at $s = 1.8$ tev. *Physical review letters*, 84(8):1663, 2000.
- [3] Ahmed Ali. Flavor changing neutral current processes in b decays. In *AIP Conference Proceedings*, volume 300, pages 437–466. American Institute of Physics, 1994.
- [4] Christoph Bobeth, Benjamin Grinstein, and Mikhail Savrov. Decay $b \rightarrow (c c^-) s$ in the leading logarithm approximation. *Physical Review D*, 77(7):074007, 2008.
- [5] Christoph Bobeth, Gudrun Hiller, and Giorgi Piranishvili. Angular distributions of $B \rightarrow Kll$ decays. *Journal of High Energy Physics*, 2007(12):040–040, dec 2007.
- [6] A. Buonauro. Tests of lepton flavour universality at LHCb. *Journal of Physics: Conference Series*, 1586:012031, aug 2020.
- [7] CERN. Accelerators. <https://home.cern/science/accelerators>. [Online; accessed 22-February-2021].
- [8] CERN. High-Luminosity LHC. <https://home.cern/resources/faqs/high-luminosity-lhc>. [Online; accessed 22-February-2021].
- [9] CERN. Linear accelerator 2. <https://home.cern/science/accelerators/linear-accelerator-2>. [Online; accessed 22-February-2021].
- [10] CERN. Precise Mapping of the Magnetic Field in the CMS Barrel Yoke using Cosmic Rays. <http://cds.cern.ch/record/1215500/plots>. [Online; accessed 22-February-2021].
- [11] CERN. SILICON PIXELS. <https://cms.cern/detector/identifying-tracks/silicon-pixels>. [Online; accessed 22-February-2021].
- [12] CERN. SILICON STRIPS. <https://cms.cern/detector/identifying-tracks/silicon-strips>. [Online; accessed 22-February-2021].
- [13] CERN. The Proton Synchrotron. <https://home.cern/science/accelerators/proton-synchrotron>. [Online; accessed 22-February-2021].
- [14] CERN. The Proton Synchrotron Booster. <https://home.cern/science/accelerators/proton-synchrotron-booster>. [Online; accessed 22-February-2021].

- [15] CMS Collaboration. Identification and filtering of uncharacteristic noise in the CMS hadron calorimeter. *Journal of Instrumentation*, 5(03):T03014–T03014, mar 2010.
- [16] CMS Collaboration. Performance and operation of the CMS electromagnetic calorimeter. *Journal of Instrumentation*, 5(03):T03010–T03010, mar 2010.
- [17] CMS Collaboration. Performance of the CMS cathode strip chambers with cosmic rays. *Journal of Instrumentation*, 5(03):T03018–T03018, mar 2010.
- [18] CMS collaboration et al. Performance of the CMS drift tube chambers with cosmic rays. *Journal of Instrumentation*, 5(03):T03015, 2010.
- [19] The CMS Collaboration. Aligning the CMS Muon Chambers with the MuonAlignment System during an Extended Cosmic Ray Run. <https://arxiv.org/pdf/0911.4770.pdf>. [Online; accessed 22-February-2021].
- [20] Emlyn Corrin. Development of digital readout electronics for the CMS tracker. *Researchgate*, 04 2003.
- [21] Diptimoy Ghosh. explaining the r_k and r_{K^*} . *The European Physical Journal C*, 77(10):1–13, 2017.
- [22] Paolo Gunnellini. The CASTOR calorimeter at the CMS experiment. *arXiv preprint arXiv:1304.2943*, 2013.
- [23] F. Halzen and Alan D. Martin. *QUARKS AND LEPTONS: AN INTRODUCTORY COURSE IN MODERN PARTICLE PHYSICS*. 1984.
- [24] Q Ingram. Energy resolution of the barrel of the CMS electromagnetic calorimeter. *Journal of Instrumentation*, 2(04):P04004–P04004, apr 2007.
- [25] Manfred Jeitler. Upgrade of the trigger system of CMS. *Nuclear Instruments and Methods in Physics Research Section A: Accelerators, Spectrometers, Detectors and Associated Equipment*, 718:11–15, 2013. Proceedings of the 12th Pisa Meeting on Advanced Detectors.
- [26] Manfred Jeitler. Upgrade of the trigger system of CMS. *Nuclear Instruments and Methods in Physics Research Section A: Accelerators, Spectrometers, Detectors and Associated Equipment*, 718:11–15, 08 2013.
- [27] F. Kircher, Bruno Levesy, Y. Pabot, D. Campi, Benoit R. Cure, Alain Herve, I.L. Horvath, P. Fabbriatore, and Riccardo Musenich. Status report on the cms superconducting solenoid for lhc. *Applied Superconductivity, IEEE Transactions on*, 9:837 – 840, 07 1999.
- [28] Karen Lingel, Tomasz Skwarnicki, and James G Smith. Penguin decays of b mesons. *Annual Review of Nuclear and Particle Science*, 48(1):253–306, 1998.

- [29] Alessio Mangoni. Hadronic decays of the J/ψ meson. *arXiv e-prints*, page arXiv:2002.09675, February 2020.
- [30] Esma Mobs. The CERN accelerator complex - August 2018. Complexe des accélérateurs du CERN - Août 2018. *CDS*, Aug 2018. General Photo.
- [31] E. A. Paschos. *Electroweak Theory*. Cambridge University Press, 2007.
- [32] Benoit Roland. Forward Physics Capabilities of CMS with the CASTOR and ZDC detectors. *arXiv preprint arXiv:1008.0592*, 2010.
- [33] A M Sirunyan et al. Electron and photon reconstruction and identification with the CMS experiment at the CERN LHC. *submitted to JINST*, 2020.
- [34] Albert M Sirunyan, Malte Backhaus, Pirmin Berger, Nadezda Chernyavskaya, Günther Dissertori, Michael Dittmar, Mauro Donegà, Christian Dorfer, Tirso Alejandro Gomez Espinosa, Dmitry Hits, et al. Performance of the reconstruction and identification of high-momentum muons in proton-proton collisions at $\sqrt{s} = 13$ TeV. *Journal of Instrumentation*, 15(2):P02027, 2020.
- [35] Albert M Sirunyan, Armen Tumasyan, Wolfgang Adam, Federico Ambrogi, Ece Asilar, Thomas Bergauer, Johannes Brandstetter, Erica Brondolin, Marko Dragicevic, Janos Erö, et al. Performance of the CMS muon detector and muon reconstruction with proton-proton collisions at $\sqrt{s} = 13$ TeV. *Journal of Instrumentation*, 2018.
- [36] Albert M Sirunyan, Armen Tumasyan, Wolfgang Adam, Ece Asilar, Thomas Bergauer, Johannes Brandstetter, Erica Brondolin, Marko Dragicevic, Janos Erö, Martin Flechl, et al. Particle-flow reconstruction and global event description with the CMS detector. *Journal of Instrumentation*, page 86, 2017.
- [37] Mark Thomson. *Modern particle physics*. Cambridge University Press, New York, 2013.
- [38] Piet Verwilligen, CMS Collaboration, et al. Muons in the cms high level trigger system. *Nuclear and particle physics proceedings*, 273:2509–2511, 2016.